STUDIES OF ZINC OXIDE AND ZINC PHOSPHATE NANOSTRUCTURES

Inaugural-Dissertation

to obtain the academic degree

DOCTOR RERUM NATURALIUM (DR. RER. NAT.)

submitted to the Department of Biology, Chemistry, Pharmacy

of Freie Universität Berlin

by

PATRICK E. J. SALOGA

from Berlin

2020

The research presented in this thesis was carried out under supervision of Andreas F. Thünemann between March 2017 and October 2020 at the Department of Materials Chemistry of Bundesanstalt für Materialforschung und -prüfung (BAM).

1st Reviewer:	Dr. habil. Andreas F. Thünemann Bundesanstalt für Materialforschung und -prüfung (BAM)
2nd Reviewer:	Prof. Dr. Thomas Risse Freie Universität Berlin
Date of Defense:	11 December 2020

ACKNOWLEDGEMENTS

This dissertation would not have been realised without the support of several people, whom I would like to thank in the following. First and foremost, I would like to express my gratitude to my supervisor and first reviewer, Andreas F. Thünemann. While providing me with the freedom to explore science and the scientific community, he has guided me through the different phases of conducting doctoral research throughout the years.

Furthermore, I am grateful to Thomas Risse for taking over the second review of this dissertation, and for the stimulating discussions we had.

I am also thankful to Christina Roth for assuming university supervision at the beginning of my doctoral project.

I would like to thank all my collaboration partners for the insights we would not have gained otherwise. In particular, this is with regard to Adam H. Clark from the Paul Scherrer Institut, and to Linn Voss, Valerie Stock, Linda Böhmert, Holger Sieg, Albert Braeuning, and Alfonso Lampen from the Bundesinstitut für Risikobewertung.

I am very grateful to the current and former members of the *Synthesis and Scattering of Nanostructured Materials* division for this time I wouldn't have enjoyed nearly as much without them. Breakfast, lunch and coffee breaks and the odd team day complemented the friendly and productive working atmosphere excellently. In particular, I would like to thank Glen J. Smales for guiding me through the delicate steps needed to obtain adequate data on our newest and largest X-ray scattering machine. I also thank Ingo Breßler, on whose introduction into Python I much relied on for data analysis, and I thank Brian R. Pauw for setting an example of how best to present this data afterwards. I would like to thank Tina Rybak for conducting all kinds of experiments in the laboratory, and Maximilian Ebisch for his efforts to keep it flawlessly organised, which I certainly torpedoed one time or another. For their support concerning dynamic light scattering and slit-collimated X-ray scattering, I am grateful to Petra Fengler and Kerstin Brademann-Jock. I am thankful to the group's organisational talent, Dana Ziegel, for helping me through all the administrative challenges I encountered from time to time. My current and former fellow doctoral candidates Jana Hildebrandt, Claudia Kästner, and Qais Saadeh are thanked for all their support. Furthermore, I would like to thank my student interns Anja Schröder, Frederik Firschke, and Jakob Heidrich for their experimental work.

I would like to acknowledge the Bundesanstalt für Materialforschung und -prüfung for financial support as a doctoral researcher, and the Gesellschaft Deutscher Chemiker for a travel stipend.

Finally, I gratefully thank my friends and family for their unconditional and constant support over the years. Without them, this dissertation would not have come into being.

ABSTRACT

In the framework of this dissertation, a microwave-assisted synthesis strategy for the production of zinc oxide nanoparticles, at the lower end of the nanoscale, is presented. The radius of these spherical particles can be adjusted by choosing a reaction temperature between 125 °C and 200 °C in the range of 2.6 nm to 3.8 nm. In this range, semiconductor particles such as those made of zinc oxide, exhibit size-dependent optical and structural properties, and tailor-made particles can aid their detailed investigation. This is demonstrated by the changes in optical band gap, photoluminescence and crystal lattice stress.

Due to their functionalisation with oleate, these zinc oxide nanoparticles are hydrophobic and only dispersible in organic solvents such as cyclohexane or tetrahydrofuran. However, some applications – for example as luminescent probes in biological systems – may require hydrophilic particles in aqueous dispersion. For this, a phase transfer procedure is presented in which the particles are transferred into an aqueous medium employing the surfactant polysorbate 80. This process is associated with further particle growth, and the final particle size can be adjusted to up to 5.7 nm *via* the duration of heating this dispersion to 90 °C.

In this context, the particle size distributions are determined *via* small-angle X-ray scattering, which, in contrast to other methods such as electron microscopy, can also be reliably applied in complex media. This is demonstrated with studies on the artificial digestion of zinc oxide nanoparticles. Zinc oxide, as well as other ionic zinc compounds, are added to food and cosmetic products due to their antibacterial effect or as food supplements and are ingested by humans. For this reason, it is essential to examine in detail any changes in the chemical and structural composition of these additives that end up being digested.

When zinc oxide and zinc chloride come into contact with artificial saliva, new, small nanoparticles with radii around 3 nm are formed, whereby the size, concentration or functionalisation of the ingested substances has no significant influence on particle formation. After the dissolution of these nanostructures in gastric juice, particles form again in the intestinal juice, but their size distribution could not be determined unambiguously. It is assumed that the newly formed particles consist of zinc phosphate, regardless of which zinc compound is initially ingested. Ion release measurements confirm the findings on the formation and dissolution behaviour of the particles obtained from small-angle X-ray scattering.

In order to investigate the particle formation from a zinc chloride solution in artificial saliva more precisely, X-ray scattering and X-ray absorption spectroscopy were employed. Within five minutes of the addition of zinc chloride to artificial saliva, nanoparticles with a radius of 1 nm are formed, and this radius remains constant for at least two weeks. The particles are found as aggregates with a radius of ca. 15 nm, in which a protein layer presumably

binds the particles together. It is assumed that the particles initially consist of amorphous zinc phosphate, which begins to crystallise within seven hours. At the same time, the aggregates densify, i.e. the distance between the particles becomes smaller. In the subsequent two weeks, the radius of the aggregate increases to ca. 22 nm as the number of bound particles also increases.

In summary, the first part of this dissertation focuses on the synthesis of reference candidate nanoparticles from zinc oxide at the lower end of the nanoscale. These particles, with adjustable size and in turn inherent optical and structural properties, are provided in both polar and apolar solvents. The second half of this dissertation, focuses on the application of small-angle X-ray scattering, and the suitability of the method for the characterisation of nanoparticles in complex media is demonstrated at an artificial digestion process. Thus, a contribution is made to the understanding of biological processes induced by the application of particulate and dissolved zinc compounds in food and cosmetic products.

KURZZUSAMMENFASSUNG

Im Rahmen dieser Dissertation wird eine mikrowellengestützte Synthesestrategie zur Herstellung von Zinkoxidnanopartikeln am unteren Ende der Nanoskala vorgestellt. Der Radius dieser sphärischen Partikel ist hierbei durch Wahl einer Reaktionstemperatur zwischen 125 °C und 200 °C im Bereich von 2.6 nm bis 3.8 nm einstellbar. Halbleiterpartikel wie aus Zinkoxid weisen in diesem Bereich größenabhängige optische und strukturelle Eigenschaften auf, zu deren eingehender Untersuchung maßgeschneiderte Partikel beitragen können. Dies wird anhand der Änderungen von optischer Bandlücke, Photolumineszenz sowie Kristallgitterspannung demonstriert.

Aufgrund ihrer Funktionalisierung mit Oleat sind diese Zinkoxidnanopartikel hydrophob und nur in organischen Lösungsmitteln wie Cyclohexan oder Tetrahydrofuran dispergierbar. Einige Anwendungen – beispielsweise als lumineszente Sonden in biologischen Systemen – können jedoch hydrophile Partikel in wässriger Dispersion erfordern. Hierzu wird eine Phasentransferprozedur vorgestellt, in der die Partikel unter Verwendung des Tensids Polysorbat 80 in wässriges Medium überführt werden. Dieser Prozess ist mit einem weiteren Partikelwachstum verbunden, wobei sich die finale Partikelgröße über die Dauer des Erhitzens der Dispersion auf 90 °C auf bis zu 5.7 nm einstellen lässt.

Die Ermittlung der Partikelgrößenverteilungen erfolgte hierbei stets mittels Röntgenkleinwinkelstreuung, welche im Gegensatz zu anderen Verfahren wie der Elektronenmikroskopie auch in komplexen Medien zuverlässig anwendbar ist. Dies wird anhand des künstlichen Verdaus von Zinkoxidnanopartikeln sowie einer Zinkchloridlösung als ionische Kontrolle demonstriert. Sowohl Zinkoxid als auch andere ionische Zinkverbindungen werden aufgrund ihrer antibakteriellen Wirkung oder zur Nahrungsergänzung Speisen und Kosmetikprodukten zugesetzt und vom Menschen aufgenommen. Aus diesem Grund ist eine genaue Untersuchung der während des Verdauvorgangs möglicherweise auftretenden Änderungen der chemischen oder strukturellen Zusammensetzung dieser Zusätze von Bedeutung.

Bei Kontakt von Zinkoxid und Zinkchlorid zu künstlichem Speichel kommt es zur Bildung neuer, kleiner Nanopartikel mit Radien um 3 nm, wobei die Größe, Konzentration oder Funktionalisierung der aufgenommenen Substanzen keinen signifikanten Einfluss auf die Partikelbildung hat. Nach der Auflösung dieser Nanostrukturen im Magensaft bilden sich abermals Partikel im Darmsaft, deren Größenverteilung jedoch nicht eindeutig bestimmbar war. Es wird angenommen, dass die neu gebildeten Partikel im Gegensatz und unabhängig von den eingesetzten Verbindungen aus Zinkphosphat bestehen. Ionenfreisetzungsmessungen bestätigen die mittels Röntgenkleinwinkelstreuung gewonnenen Erkenntnisse über das Bildungs- und Auflösungsverhalten der Partikel.

Um die Partikelbildung aus einer Zinkchloridlösung im künstlichen Speichel genauer zu untersuchen, werden Röntgenstreuung und Röntgenabsorp-

tionsspektroskopie eingesetzt. Innerhalb von fünf Minuten nach Zugabe von Zinkchlorid bilden sich Nanopartikel, deren Radius bei 1 nm liegt und in den folgenden zwei Wochen konstant bleibt. Die Partikel liegen als Aggregate mit einem Radius von etwa 15 nm vor, in denen vermutlich eine Proteinschicht die Partikel miteinander verbindet. Es wird angenommen, dass die Partikel zunächst aus amorphem Zinkphosphat bestehen, welches innerhalb von sieben Stunden zu kristallisieren beginnt. Gleichzeitig kommt es zu einer Verdichtung der Aggregate, d.h. die Abstände der Partikel zueinander werden geringer. In den darauf folgenden zwei Wochen vergrößert sich der Aggregatradius unter Zunahme der Anzahl der gebundenen Partikel auf etwa 22 nm.

Zusammengefasst liegt der Fokus des ersten Teils dieser Dissertation auf der Synthese von Referenzkandidatenmaterialien aus Zinkoxidnanopartikeln am unteren Ende der Nanoskala. Diese Partikel, mit einstellbarer Größe und den damit verbundenen optischen und strukturellen Eigenschaften, werden in polaren sowie apolaren Lösungsmitteln zur Verfügung gestellt. Im zweiten, auf die Anwendung der Röntgenkleinwinkelstreuung fokussierten Teil, wird die Geeignetheit der Methode zur Charakterisierung von Nanopartikeln in komplexen Medien anhand des künstlichen Verdauvorgangs demonstriert. Somit wird zur Aufklärung der durch die Anwendung partikulärer und gelöster Zinkverbindungen in Lebensmitteln und Kosmetikprodukten induzierten, biologischen Vorgänge beigetragen.

NOMENCLATURE

BAM	*Bundesanstalt für Materialforschung und -prüfung* (German Federal Institute for Materials Research and Testing), Berlin, Germany
BfR	*Bundesinstitut für Risikobewertung* (German Federal Institute for Risk Assessment), Berlin, Germany
BSA	Bovine Serum Albumin
DLS	Dynamic Light Scattering
EXAFS	Extended X-ray Absorption Fine Structure
ICSD	Inorganic Crystal Structure Database
JRC	Joint Research Centre, European Commission's science and knowledge service
PSI	Paul Scherrer Institute, Villigen, Switzerland
SAXS	Small-angle X-ray Scattering
SLS	Static Light Scattering
UDEDM	Uniform Deformation Energy Density Model
UDM	Uniform Deformation Model
USDM	Uniform Stress Deformation Model
WAXS	Wide-angle X-ray Scattering
XAFS	X-ray Absorption Fine Structure
XANES	X-ray Absorption Near-Edge Structure
XRD	X-ray Diffraction

LIST OF FIGURES

CONTENTS

1 INTRODUCTION

Early humans were presumably aware of eight orders of magniatude in size, from the thickness of a human hair of just under 100 µm[1] to the size of landscape formations of a few kilometres. However, processes in our world proceed on a scale of more than 60 orders of magnitude, assuming the Planck length (10^{-35} m) as lower, and the diameter of the observable universe (10^{27} m) as upper limit.[2] Of practical relevance to material development is undoubtedly the size range of $10^{-10} - 10^{0}$ m, from atoms to macroscopic objects.

While the existence of atoms as indivisible particles has been postulated since ancient times,[3,4] their size has been estimable at the order of 10^{-10} m since the early 20th century.[5] The nanoscale ($10^{-9} - 10^{-7}$ m), however, was excluded from systematic research until the end of 1959, when Richard Feynman pointed out that "There's Plenty of Room at the Bottom" in a famous lecture of the same title.[6] Since then, he has been considered the founder of "nanotechnology", a term coined by Norio Taniguchi in 1974.[7] It appears reasonable to assume that the targeted manipulation of interdependent objects, from atoms to macroscopic entities, with exhaustively optimised structures on each length scale, could open up undreamt possibilities in material development.

This dissertation primarily focuses on the lower nanoscale, on structures smaller than 10 nm. In this size range, quantum size effects can occur, for instance, in semiconductor particles, the optical band gap becomes dependent on particle size.[8] It is within this context that this dissertation provides strategies for the synthesis of small zinc oxide nanoparticles with adjustable size, and thus optical and structural properties. Microwave-assisted synthesis techniques are applied, enabling reaction control at elevated temperatures and pressures. Thus, an enormous increase in reaction rates is achieved, in comparison to conventional synthesis methods, whilst also providing control over the final particle size. In combination with a polysorbate-mediated phase transfer, zinc oxide particles at the lower end of the nanoscale with adjustable size are thereby provided both in organic and aqueous dispersions.

One particular challenge in identifying correlations between particle sizes and optical properties lies within precise size determination. In this context, small-angle X-ray scattering (SAXS) is excellently suited to investigate nanoparticles and determine size distributions. This technique can be applied in complex media, such as digestive juices, which opens up another thematic constellation of this dissertation: zinc compounds in artificial digestion. The behaviour of zinc oxide and zinc chloride in three digestive stages of saliva, gastric juice and intestinal juice is investigated with respect to particle size distribution changes and particle dissolution, with an emphasis upon the formation of novel particles from ionic precursors.

2 THEORETICAL BACKGROUND

2.1 NANOMATERIALS

An international standard defines the nanoscale as the size range between approximately 1 nm and 100 nm, along with the indication that novel, size-specific effects occur in this range.[9] A narrower definition proposed by the European Commission sets the size range to strictly 1 nm to 100 nm with exceptions for certain carbon-based materials such as graphene.[10] Following this proposal, materials shall be classed as nanomaterials when for at least 50% of the particles in the number-weighted size distribution, at least one of their external dimensions falls in the said size range.[10] Accordingly, nanomaterials can be divided into nanosheets, nanowires or nanoparticles based on the number of their nanoscale dimensions (see Figure 2.1 for examples). Frequently, these are also referred to as 2D, 1D, or 0D nanoobjects, respectively, relating to the number of their non-nanoscale dimensions.

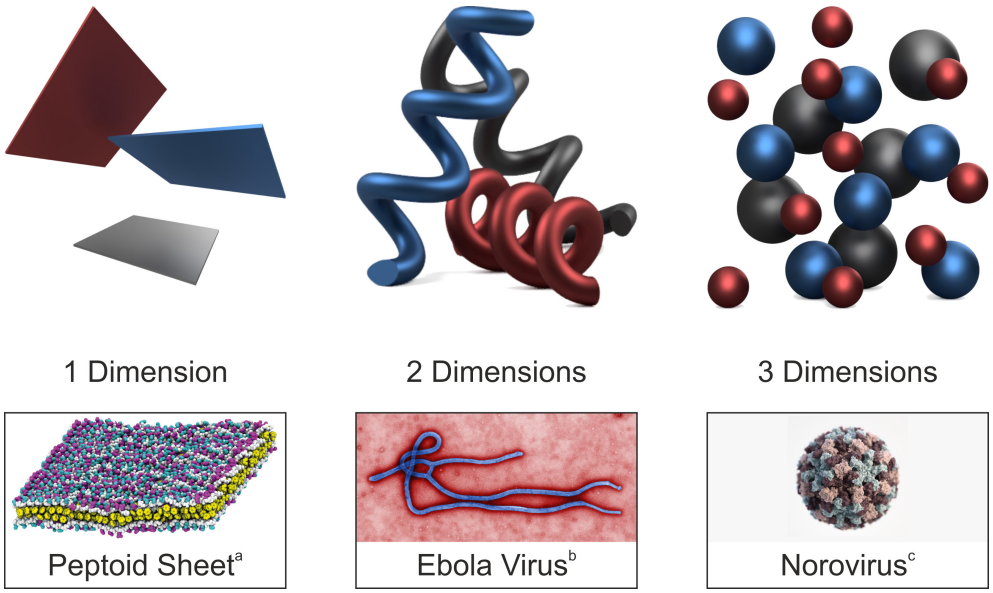

Figure 2.1: Examples for nanomaterials with one, two, or three nanoscale dimensions, from left to right.

[a] Mannige et al. *Nature* **2015**, *526*, 415-420.
[b] Public Health Image Library (PHIL) ID 10816, by Cynthia Goldsmith (Centers for Disease Control and Prevention, CDC).
[c] PHIL ID 21350, by Alissa Eckert, MS (CDC).

It is mainly at the lower nanoscale, where materials of those dimensions show properties different to those of the corresponding bulk material. This is mainly due to the tremendously increasing surface-to-volume ratio and the occurrence of quantum size effects. The former, for example, provides access to enhanced catalytic activities through the greater surface area pro-

vided in a given volume of material. As an illustration, 1 g of the zinc oxide nanoparticles with a radius of 2.6 nm produced in project **1** of this dissertation provide a surface area increased by a factor of 10^6 compared to a 1 g sphere of the bulk material. The exploited properties of such an enhanced surface area, however, could also be observed in the bulk phase. Occasionally, the mere applicability at specific locations, such as in biological systems, is the reason for using nanoparticles, as in the case of upconverting nanoparticles whose luminescence yield is lower for nanoparticles as compared to the bulk.[11] In contrast, quantum size effects only occur when particle sizes drop below a threshold of roughly 10 nm,[12,13] as is the case with the optical properties of zinc oxide studied in this dissertation. In semiconductor materials such as zinc oxide in this size range, the particle dimensions drop below the De Broglie wavelength of the charge carriers (electrons and holes), which leads to confinement of their movement and quantisation of their energy states. Provided that the thermal energy does not exceed the Coulomb attraction of electron and hole, these form pairs, excitons. When they decay, these excitons can emit light with a narrow wavelength distribution, just like atoms, which leads to them occasionally being referred to as "artificial atoms".[14]

2.2 ZINC OXIDE NANOPARTICLES

2.2.1 Properties

The semiconductor zinc oxide (ZnO) is predominantly available as a powder, which, since ancient times, has been used as a pigment and eventually replaced more toxic, lead-containing ones in the 18th century.[15–17] The mineral zincite represents the natural source of zinc oxide; however, for practical applications, it is industrially synthesised on a scale of 10^5 tonnes.[18,19] At ambient conditions, zinc oxide will commonly be obtained in its thermodynamically most stable hexagonal wurtzite structure, while its cubic zincblende and rock-salt structures can be synthesised by epitaxial growth or under high pressure, respectively.[15]

Pharmaceutical applications of zinc oxide date back to medieval times, since when it has been referred to as *nihilum album* and used as a remedy.[17] Antibacterial properties led to its use in deodorant as early as 1888, and still today, it is applied in skin and dental care.[16,20,21] Zinc oxide is used as an activator in the sulfur vulcanisation of rubber to increase efficiency and reduce reaction time. At the same time, this enables a significant release of ZnO into the environment through rubber abrasion.[22]

Systematic research into the optical and structural properties of zinc oxide began around 1930.[23,24] With a direct band gap of 3.37 eV at room temperature, light absorption sets in below a wavelength of 368 nm, facilitating applications as UV absorbers in food packaging and sunscreens.[16,25,26] As laid out in the previous chapter, the optical properties of zinc oxide become size-dependent for particles at the lower nanoscale. For radii in the range of 1.5 nm to 3.5 nm, Jacobsson and Edvinsson determined the band gap energy of zinc oxide nanoparticles, E_g (in eV), to be dependent on the particle radius, R_0 (in nm), as:[27]

$$E_g = C_1 + \frac{C_2}{R_0} + \frac{C_3}{R_0^2} \tag{2.1}$$

They ascertained the coefficients as $C_1 = 3.30$, $C_2 = 0.1465$, and $C_3 = 0.985$ and compared them to theoretical values of 3.37, -0.675, and 2.18, respectively. It is reasonable that C_1 should correspond to the band gap energy of bulk zinc oxide since the latter two terms become negligibly small with increasing particle size. Therefore, within the scope of this dissertation, C_1 was set to the widely accepted value of $E_{g,bulk} = 3.37$ eV at room temperature for curve fitting according to Equation 2.1.[25,28,29]

Zinc oxide shows luminescence, which is often described as green with a wavelength around 550 nm, but the colour is also dependent on the particle size.[27,30] The exact cause of this is still disputed and is commonly attributed to point defects.[25,28]

2.2.2 Synthesis

Nanoparticle synthesis methods can be divided into top-down and bottom-up processes, wherein either macroscopic materials are broken down to

the nanoscale or are built up from sub-nanoscale molecules through chemical reactions, respectively. An example of a top-down approach is the mechanochemical production using a ball mill, whereby zinc oxide is produced from calcined zinc carbonate, obtained as follows with subsequent calcination:[31]

$$\mathrm{ZnCl_2 + Na_2CO_3 \longrightarrow ZnCO_3 + 2\,NaCl}$$

$$\mathrm{ZnCO_3 \xrightarrow{\Delta} ZnO + CO_2}$$

Contrary, in the context of this dissertation, liquid phase, bottom-up approaches were used exclusively. These are based on reducing the solubility of a substance, which then precipitates out of solution and, depending on reaction conditions and additives, can be stabilised in nanoscale dimensions. In principle, this can be achieved by modifying the solvent or synthesising a less soluble species (monomers with respect to the grown particles), the latter having been carried out in this dissertation. Victor LaMer developed a kinetic model which describes this formation of nanoparticles and in particular reflects the conditions for the formation of monodisperse ones.[32] Its graphical representation, depicting the change in monomer concentration over time, is given in Figure 2.2.

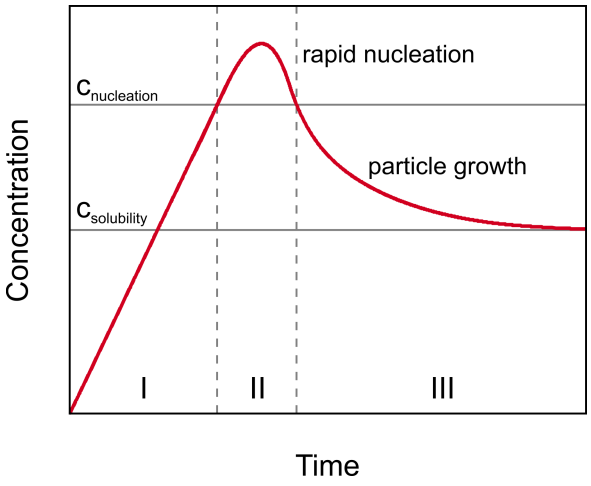

Figure 2.2: Concentration of monomers during production, nucleation and growth phases, I, II, and III, respectively, based on LaMer et al.[32]

The process can be divided into three phases: monomer production phase (I), nucleation phase (II), and particle growth phase (III). In the first phase, a readily soluble precursor is converted into monomers with a solubility of $c_{\mathrm{solubility}}$, thereby creating a supersaturated solution. Conversely, $c_{\mathrm{solubility}}$ of existing monomers can be exceeded by adding a poor solvent, although their total concentration decreases. Once a critical concentration $c_{\mathrm{nucleation}}$ is reached, the monomer concentration is decreasing rapidly in phase II, and nuclei are formed, which then grow to the final particles in a diffusion-controlled way in phase III. From this model it can be derived that a strict separation of phases II and III is indispensable for the production of monodis-

perse particles, meaning that at first, uniform nuclei are generated, which subsequently grow as uniformly into nanoparticles.[32]

For the production of zinc oxide nanoparticles in this dissertation, the hydrolysis synthesis of spherical, oleate-coated particles previously published by Ehlert et al., was adapted for a one-pot, microwave-assisted synthesis.[30] Therein, the zinc soap is dissolved in tetrahydrofuran, to which a base, tetrabutylammonium hydroxide, dissolved in methanol, is added. Nanoparticle syntheses frequently rely on metal oleates as they can be thermally decomposed and then function as stabilisers for the particles formed.[33] The reaction mixture is subjected to autoclave-like, microwave-assisted heating, facilitating reactions at elevated temperatures and pressures.[34] Based on previous experience, this type of reaction control was expected to give access to an enormous reduction in reaction time and to other particle sizes than conventional synthesis methods.[35]

The acceleration of the reaction in microwave-assisted syntheses is essentially based on autoclave-like reaction control, which allows for higher reaction temperatures above the boiling point of the solvent. The relationship between reaction temperature, T, and rate constant, k, is then the same as given in the Arrhenius equation with a prefactor, A, the energy of activation, E_A, and the gas constant, R:[36,37]

$$k = A \cdot e^{-\frac{E_A}{RT}} \tag{2.2}$$

This acceleration would also occur if other heat sources than microwave radiation were used, and resulting variations in the reaction course are referred to as thermal effects. Whether so-called microwave-specific or non-thermal effects occur in microwave-assisted syntheses, in which either the unique heating mechanism plays a role or a direct influence is exerted on the reaction path, remains disputed in the literature. However, there is a broad consensus that most observed effects are merely thermal effects for which no microwave radiation is required.[38]

While the LaMer model provides a plausible explanation of nanoparticle growth and is sufficient for some quantitative and qualitative considerations, actual syntheses can also take place *via* various intermediate stages that are not considered there. For the synthesis performed in this dissertation, Herbst et al. conducted an *in situ* investigation on nucleation and particle growth, considering the following reaction:[33]

$$Zn^{2+} + 2\,OH^- \longrightarrow ZnO + H_2O$$

At reaction temperatures of 40 °C and 50 °C, they observed that the particle synthesis could be divided into a 1000 second long nucleation and growth phase to which a second growth phase adjoins, taking up to 4.5 hours. Within 20 seconds, the critical concentration of monomers was reached, leading to the formation of first nuclei of 0.5 nm radius, which then grew to almost their final size during the first growth phase. Therein, the precursor reaction rate constant was primarily dependent on the reaction temperature, while the growth rate constant was dependent on precursor concentration as well. Higher reaction temperatures led to an increase in the ratio of growth and precursor reaction rate and thus to larger particles. Interestingly, the

yielded particles were amorphous at first and did not crystallise until the second growth phase, which lasted for hours but only resulted in an increase in particle size of less than 2 Å.[33]

2.3 METHODS AND TECHNIQUES

2.3.1 Dynamic Light Scattering

Dynamic Light Scattering (DLS) enables the determination of the diffusion coefficient of nanoparticles in dispersion by time-resolved analysis of their Rayleigh scattering. In contrast, static light scattering (SLS) involves a time-averaged measurement of the scattering intensity over various scattering angles, typically to determine the size or molecular weight of polymers.[39,40] During the measurement, the sample is irradiated with laser light of a wavelength, λ, and the scattered light is detected at an angle, 2θ, as shown schematically in Figure 2.3.

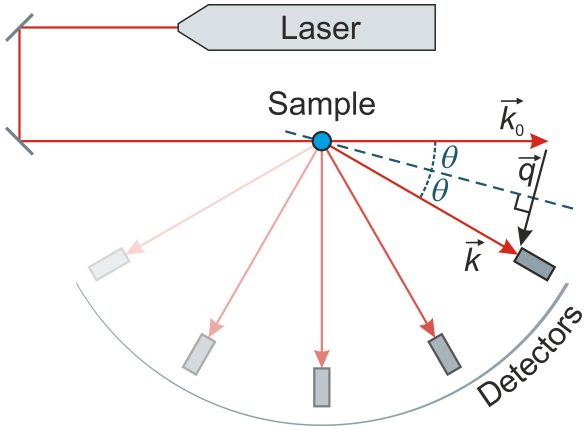

Figure 2.3: Scheme of a multi-angle DLS set-up as used in this dissertation.

In the process, incoming light with a wave vector, $\vec{k_0}$, is scattered elastically and assumes a new wave vector, $\vec{k}$, where $\vec{k} - \vec{k_0}$ is equal to the scattering vector, $\vec{q}$, whose modulus is given as follows with the refractive index, n:

$$q = \frac{4\pi n}{\lambda} \sin\theta \tag{2.3}$$

When using coherent laser light, a fluctuation of the scattered light intensity, $I(t)$, over time, t, can be measured, which is caused by the Brownian motion of the particles. $I(t)$ contains information on the diffusion behaviour of the particles, whose more detailed analysis begins with the calculation of the intensity autocorrelation function, $G_2(\tau)$. This is determined for many different pairs of points in time and is only dependent on the time-lag, τ, between them:[41]

$$G_2(\tau) = \langle I(t) \cdot I(t+\tau) \rangle \tag{2.4}$$

If the particle sample to be examined is monodisperse, $G_2(\tau)$ can be approximated with an exponential function according to equation 2.5, using the parameters A, B and the decay rate, Γ, which in turn is related to the diffusion coefficient, D, as in equation 2.6.[41]

$$G_2(\tau) = A\left[1 + B\ \mathrm{e}^{-2\Gamma\tau}\right] \tag{2.5}$$

$$\Gamma = Dq^2 \tag{2.6}$$

The hydrodynamic radius, R_h, can be determined from the diffusion coefficient using the Stokes-Einstein equation (equation 2.7) with the Boltzmann constant, k_B, for a known temperature, T, and viscosity, η, of the dispersion medium. This is an equivalent sphere radius, i.e. that of a hypothetical sphere which would diffuse in the same way as the particles in the sample.[41]

$$D = \frac{k_B T}{6\pi\eta R_h} \tag{2.7}$$

So far these elaborations are only applicable to monodisperse particle systems, which are rarely found in practice. To enable the analysis of polydisperse samples, the previously constant decay rate, Γ, must be expanded to a distribution, $G(\Gamma)$. This is achieved by introducing the field autocorrelation function, $g_1(\tau)$, whose square corresponds to the exponential term in equation 2.5:[41]

$$g_1(\tau) = \int_0^\infty G(\Gamma)\mathrm{e}^{-\Gamma\tau}d\Gamma \quad \text{where} \quad \int_0^\infty G(\Gamma)d\Gamma = 1 \tag{2.8}$$

The method of cumulants was used for evaluation of DLS results in this dissertation. This involves expanding the term $\mathrm{e}^{(-\Gamma\tau)}$ in equation 2.8 around a mean value, $\langle\Gamma\rangle$, in a Taylor series expansion, which for narrow $G(\Gamma)$ can be terminated after the term with order 2:[42]

$$\mathrm{e}^{-\Gamma\tau} = \mathrm{e}^{-\langle\Gamma\rangle\tau}\left[1 - (\Gamma - \langle\Gamma\rangle)\tau + (\Gamma - \langle\Gamma\rangle)^2\frac{\tau^2}{2}\right] \tag{2.9}$$

Eventually, the mean value, $\langle\Gamma\rangle$, and variance, μ_2, of the decay rate distribution, $G(\Gamma)$, are obtained from equations 2.10 and the polydispersity index, PI, as a measure of the particle size distribution width according to equation 2.11.[42]

$$\langle\Gamma\rangle = \int_0^\infty G(\Gamma)\Gamma d\Gamma \quad \text{and} \quad \mu_2 = \int_0^\infty G(\Gamma)(\Gamma - \langle\Gamma\rangle)^2 d\Gamma \tag{2.10}$$

$$PI = \frac{\mu_2}{\langle\Gamma\rangle^2} \tag{2.11}$$

2.3.2 X-ray Scattering

The history of X-ray scattering essentially dates back to Wilhelm Conrad Röntgen's discovery of X-rays in 1885,[43] while Peter Debye reported on their scattering for the first time in 1915, in a work entitled "*Zerstreuung von Röntgenstrahlen*."[44] X-ray scattering can be considered the equivalent of light scattering – only at smaller wavelengths –, and as there, it is possible to distinguish between dynamic and static scattering. While the former method, X-ray photon correlation spectroscopy, is comparably new and relies on coherent radiation sources such as free-electron lasers,[45–47] the static variant has been used in the context of this dissertation. Based on the investigated regime of scattering angles, it can be divided in, e.g. small-angle and wide-angle X-ray scattering (SAXS and WAXS, respectively).

Generally, small-angle scattering of X-rays occurs when they interact with nanoscale inhomogeneities in the electron density of matter, such as at phase boundaries between nanoparticles and their surroundings, but equally within the particles themselves. Thus SAXS is suitable, provided appropriate samples in each case, for the determination of internal and external dimensions, shapes, but also the investigation of surface structure, particle-particle interactions, or molar mass.[48,49] Wide-angle X-ray scattering, on the other hand, probes properties on the atomic length scale such as crystal structure and is essentially the same as widely applied X-ray diffraction (XRD).

In this work, SAXS was used regularly for the non-destructive analysis of nanostructures, concerning size and structural organisation. While electron microscopy is an extensively applied technique for the characterisation of nanoparticles, in most examples in the literature, only up to several hundred nanoparticles of any one sample are examined as opposed to the analysis of billions of particles when employing SAXS. Thus, a result determined by SAXS is based on a significantly larger sample, whereas the analysis of a few particles by electron microscopy allows the selection of hypothesis-fitting results contrary to scientific standards. However, SAXS results are ambiguous and must, therefore, be combined with those obtained with other methods. For instance, a derived particle size distribution is generally only meaningful if the shape of the particles is known from another means of investigation.

For this dissertation, two different SAXS instruments were used: mainly the SAXSess (from Anton Paar, Austria), and a customised Xeuss 2.0 (from Xenocs, France). The SAXSess is a Kratky-type camera with a slit-collimated X-ray beam, which, due to the greater irradiated sample volume in comparison to point-collimated instruments, is particularly suitable for weakly scattering isotropic samples and offers shorter measurement times.[50] On the other hand, the obtained scattering curve is convoluted with the beam profile, so that for analysis it must either be deconvoluted, whereby the uncertainties may increase, or a model convoluted with the beam profile must be fitted.[51] This effect is less pronounced for point-collimated instruments such as the customised Xeuss 2.0, which allows for investigations of anisotropic samples over a larger size range than the SAXSess, and also into the WAXS region, but may require longer measurement times. This instru-

ment was mainly used when the measurable size range of the SAXSess was not sufficient.

The scattering process of incoming X-rays with a wave vector, $\overrightarrow{k_0}$, at two scattering points, P and S, of a sample with an electron density, $\rho(\overrightarrow{r})$, is depicted in Figure 2.4.

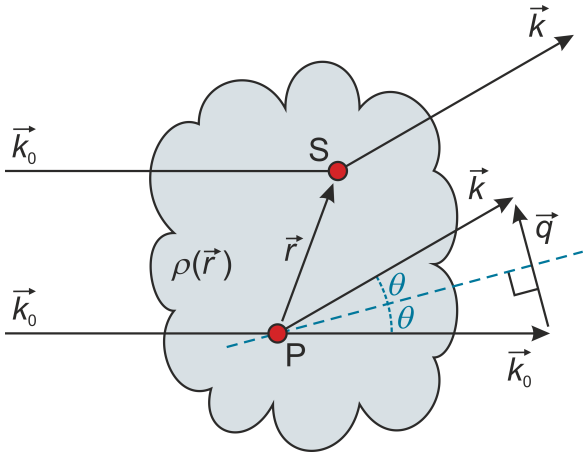

Figure 2.4: Scheme of the X-ray scattering process at matter, based on Moscosco Londoño et al.[52]

X-rays are elastically scattered at an angle, 2θ, creating elementary waves at P and S with a wave vector, k. The scattering vector, $\overrightarrow{q}$, is defined as $\overrightarrow{k} - \overrightarrow{k_0}$ and its modulus is given as follows:

$$q = 4\pi \frac{\sin\theta}{\lambda} \tag{2.12}$$

Constructive interference of the outgoing waves is strongest when Bragg's law is fulfilled:[53]

$$n\lambda = 2d\sin\theta \tag{2.13}$$

with an integer, n, radiation wavelength, λ, interplanar spacing, d, and the diffraction angle, θ. From combination of equations 2.13 and 2.12 results that a scattering maximum at a certain q-value corresponds to an interplanar spacing of $d = 2\pi/q$. This implies that a scattering curve recorded between the scattering vectors $q_{\min}$ and $q_{\max}$ limits the size resolution to the radial range of $R_{\min}$ and $R_{\max}$ according to equations 2.14.

$$R_{\min} = \frac{\pi}{q_{\max}}, \quad R_{\max} = \frac{\pi}{q_{\min}} \tag{2.14}$$

Within this thesis, particle sizes were usually stated as radii, R, and scattering curves recorded in q-ranges of $0.1\,\mathrm{nm}^{-1}$ to $4\,\mathrm{nm}^{-1}$ on the slit-focus and $0.013\,\mathrm{nm}^{-1}$ to $25\,\mathrm{nm}^{-1}$ on the point-focus instrument, roughly corresponding to size resolutions in the R-range of 1 nm to 30 nm and 0.13 nm to 250 nm, respectively.

The electron density, $\rho(\overrightarrow{r})$, of the sample is the property investigated by SAXS. Its relation to the measured intensity, $I(\overrightarrow{q})$, is depicted in the "magic square of scattering" (equation 2.15). Therein, the electron density, $\rho(\overrightarrow{r})$, the

amplitude, $A(\overrightarrow{q})$, the correlation function, $P(\overrightarrow{r})$, and the intensity, $I(\overrightarrow{q})$, are depicted on the square's corners and are connected *via* operations leading from one sample property to the next. The left side of the square depicts real space as a function of $\overrightarrow{r}$, and the right side depicts reciprocal space as a function of $\overrightarrow{q}$. Both sides are connected *via* reversible Fourier transforms, $\mathscr{F}$, while the upper side is connected to the lower side by irreversible autocorrelation, ^{*2}, and absolute square, $||^2$.[54–56]

$$\begin{array}{ccc} \rho(\overrightarrow{r}) & \overset{\mathscr{F}}{\longleftrightarrow} & A(\overrightarrow{q}) \\ {\scriptstyle *2}\downarrow & & \downarrow{\scriptstyle ||^2} \\ P(\overrightarrow{r}) & \overset{\mathscr{F}}{\longleftrightarrow} & I(\overrightarrow{q}) \end{array} \tag{2.15}$$

This makes it obvious that the determination of $\rho(\overrightarrow{r})$ of the sample, and thus for example particle sizes, from the intensity measured by the detector is not straightforward. Nevertheless, conversely, it is possible to calculate the resulting scattering curve from an assumed electron density distribution and compare it with the measured $I(q)$. Within the scope of this dissertation, two software packages were used for this purpose: McSAS[57] and SASfit.[58] While the shape of the nanostructures is predefined in both methods, the size distributions are determined randomly in McSAS, and a preselected distribution function is fitted in SASfit, each until a defined goodness of fit is achieved. Furthermore, SASfit provides the possibility to simulate scattering curves based on preselected particle shapes and sizes, which was used in the following illustration of the fundamental characteristics of scattering curves as in this dissertation (Figure 2.5).

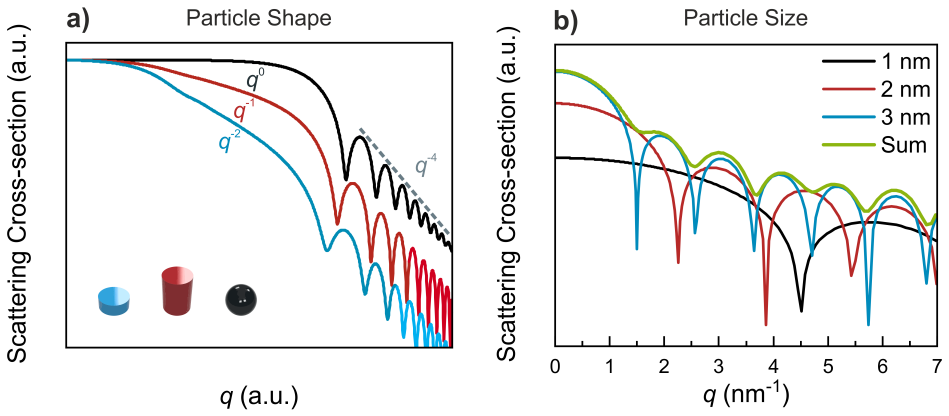

Figure 2.5: (a) Simulated scattering curves of spheres (black), cylinders (red), and platelets (blue) with indication of characteristic curve slopes. (b) Simulated scattering curves of spheres with radii of 1 nm, 2 nm, and 3 nm, and the sum of their scattering contributions.

Panel **a** depicts the general form of a scattering curve for different particle shapes: spheres, cylinders, and platelets. At low q-values, the scattering curves reach a plateau, the Guinier region, which is indicative of the overall particle size. As this plateau is reached, it can be concluded that the scattering curve represents the "whole" nanoparticle, while the absence of such plateau may indicate the presence of structures larger than what can be re-

solved from a certain q-range. In the subsequent Fourier region in direction of higher q, the curve is seen to decay with shape-dependent slopes; q^0 for spheres, q^{-1} for cylinders, and q^{-2} for platelets. The presence of these characteristic slopes in the scattering curve is indicative of the probed particles having the respective shapes; however, this is no proof. In the following Porod region, the scattering curves decay with a slope of q^{-4}, showing that these simulated particles all have a classical surface. In panel **b** of Figure 2.5, scattering curves of spherical particles of different radii, R, are shown. These curves display sharp minima whose positions are defined by the roots of the form factor for a sphere, the mathematical model describing its scattering (Equation 2.21). This is zero when $\tan qR = qR$, implying that the positions of the minima are shifted to smaller q values for larger particles. In principle, this relation could be used to determine particle sizes from the position of the minima; however, this would presuppose a sample of monodisperse, homogeneous spheres. Furthermore, panel **b** depicts the curve of the sum of the three scattering contributions, indicating that the presence of less pronounced minima is a simple indicator for polydisperse samples.

In the following, a short outline of the equations used for curve fitting within this dissertation shall be given as to enable later reference. In general, the scattering intensity, $I(q)$, is modeled as the sum of the product of the form and the structure factor, $P(q)$ and $S(q)$, and a background function, $I_{\mathrm{bkg}}(q)$:

$$I(q) = P(q)S(q) + I_{\mathrm{bkg}}(q) \tag{2.16}$$

$I_{\mathrm{bkg}}(q)$ (Equation 2.17) with parameters a, b, and p, is introduced to account for both a linear, horizontal background when $p = 0$, as well as structures larger than what can be resolved from the investigated q-range, when $p = 4$.

$$I_{\mathrm{bkg}}(q) = a + bq^{-p} \tag{2.17}$$

$P(q)$ is composed of the scattering contrast, $\Delta\rho$,– the scattering length density difference between particle and surrounding medium –, a particle size distribution, $f(R)$, and the scattering contribution of a single particle of a certain shape, $I_s(q, R)$, as follows:

$$P(q) = \int_0^\infty (\Delta\rho)^2 f(R) I_s(q, R) dR \tag{2.18}$$

This means that for a meaningful measurement, there must be a sufficiently large difference between the electron densities of the sample and the matrix. It is also noteworthy that the phase information is lost by squaring this difference, which is why nanoparticles in dispersion cannot be distinguished from foam with corresponding nanopores simply by the shape of their scattering curves. This is a general theorem in optics and known as Babinet's principle.[59] While $f(R)$ is form-free in McSAS, when using SASfit, a specific distribution has to be chosen, which in the context of this dissertation is the log-normal distribution, $f(N, R, R_{\mathrm{median}}, \sigma_{\log})$. With the particle number density, N, median radius, R_{median}, and the width parameter of the size distribution, $\sigma_{\log}$, this can be written as:

$$f(N, R, R_{\text{median}}, \sigma_{\log}) = \frac{N}{R\sigma_{\log}\sqrt{2\pi}} \exp\left[-\frac{(\ln R - \ln R_{\text{median}})^2}{2\sigma_{\log}^2}\right] \tag{2.19}$$

Mean particle radius, R_{mean}, and distribution width, σ, can then be calculated as follows:

$$R_{\text{mean}} = R_{\text{median}} e^{\sigma_{\log}^2/2} \text{ and } \sigma = R_{\text{mean}}(e^{2\sigma_{\log}^2} - e^{\sigma_{\log}^2})^{1/2} \tag{2.20}$$

The scattering intensity originating from a sphere for a scattering vector, q, depends on the radius, R, as follows:[51,60,61]

$$I_s(q, R) = \left[4\pi R^3 \frac{\sin qR - qR\cos qR}{(qR)^3}\right]^2 \tag{2.21}$$

$S(q)$ represents particle-particle-interactions and can be set to unity for dilute dispersions with no such interactions. Within this dissertation, two different structure factors are utilised, one each to describe repulsive and attractive interactions. The former is the hard-sphere structure factor, $S_{\text{hs}}(q, R, \varphi)$, and the latter, $S_{\text{agg}}(q, D, r_0, \xi)$, accounts for particle aggregation to mass fractals.[62–65] Here, φ is the volume fraction of the particles, D is the fractal dimension, r_0 is the distance between the scatterers and thus the mean radius of individual particles including any shell that otherwise may be invisible to SAXS, and ξ is the fractal aggregate size. For the longish mathematical representations, reference is made to their presentation in Publication **3** (Section 4.3) as well as to the literature references given.[66]

Moving from the SAXS region considered up to here in the direction of larger q, the WAXS region adjoins and was analysed concerning atomic lattice properties in the context of this dissertation. The simplest method was to compare the position of reflections in the scattering curve with reference values from crystallographic databases in order to obtain an indication of the material composition of the sample. On closer inspection of these reflection peaks, it becomes apparent that they are not infinitely narrow, but have a width that is determined by the properties of both the sample and the instrument.[67] Consequently, the measured peak width can be expressed as a convolution of an instrument- and a sample-induced broadening whereby the former was approximated as a Gaussian- and the latter as a Lorentzian-shaped contribution.[68,69] Using an analytical expression derived by Ruland, the instrumental broadening can then be removed from the experimentally determined one in order to obtain and evaluate the sample-dependent broadening.[70] Based thereon, structural properties such as crystallite size according to Scherrer or lattice strain, stress, and deformation energy density can be determined *via* different approaches based on Williamson-Hall analysis.[71–73] These have been applied in project **1** (Appendix 4.1) and are laid out there and in the stated literature references.[34]

2.3.3 X-ray Absorption Fine Structure Spectroscopy

X-ray absorption fine structure (XAFS) spectroscopy probes local variations in the absorption behaviour of a material around distinct absorption edges, first observed by Hugo Fricke in 1920.[74] In practice, X-rays of variable energy are obtained from a synchrotron, and the change in their intensity during their passage through the sample is measured. In the context of this dissertation, this was performed at the SuperXAS beamline of the Swiss Light Source at the Paul Scherrer Institute, Switzerland. There, a bending magnet is used to deflect the electron beam, thereby generating a polychromatic X-ray beam. This is then directed towards the sample *via* a monochromator to allow scanning over a certain photon energy range, and ionisation chambers are positioned before and after the sample in the beam direction, for measurement of its intensity. XAFS measurements with a time resolution of 10 ms are enabled with this arrangement, which is therefore ideally suited for *in situ* investigations.[75]

Following the Beer-Lambert law, from the measured X-ray beam intensities before (I_0) and after (I) passage through a sample of thickness d, the attenuation coefficient, μ, can be calculated:[76]

$$I = I_0 \mathrm{e}^{-\mu d} \tag{2.22}$$

For μ, roughly, the following dependence on the atomic number, Z, and photon energy, E, applies:[77]

$$\mu \propto \frac{Z^x}{E^3} \quad \text{where} \quad 3 \leq x \leq 4 \tag{2.23}$$

Normalisation of μ to the sample density, ρ, yields the total mass attenuation coefficient, μ/ρ, which for zinc is depicted in panel **a** of Figure 2.6 as a function of the photon energy, E. In the depicted energy range, μ/ρ is mainly dependent on photoabsorption processes, in which electrons are removed from their atoms. A decrease with E^3 is clearly visible; however, two discontinuities at energies E_0 can be seen in the spectrum, where the absorption suddenly increases. Consequently, these are referred to as absorption edges, where the photons reach the binding energy of core electrons, which is decreasing with increasing principal quantum number, n, of the excited electrons. According to that number, the edges are referred to as K-edge for $n = 1$, L-edges for $n = 2$, M-edges for $n = 3$ and so forth. The edges seen in the spectrum are the Zn K-edge just below 10 keV and the Zn L-edges located slightly above 1 keV.[78–80] In the context of this dissertation, experiments were carried out at the Zn K-edge. For K-edge excitations, transitions from *s*- to *p*-states are electric-dipole allowed and will be observed.[78] Experimental data of this edge obtained in the course of this dissertation is depicted in panel **b** of Figure 2.6. Evidently, the (experimentally measured) Zn K-edge does not only consist of a mere discontinuity in the otherwise monotonic decreasing μ/ρ, but does show distinct features: the X-ray Absorption Near-Edge Structure (XANES) and the Extended X-ray Absorption Fine Structure (EXAFS). While there is no strict, defined boundary between the two, the former commonly extends up to 30 eV to 50 eV above the edge itself, and the latter adjoins.[81]

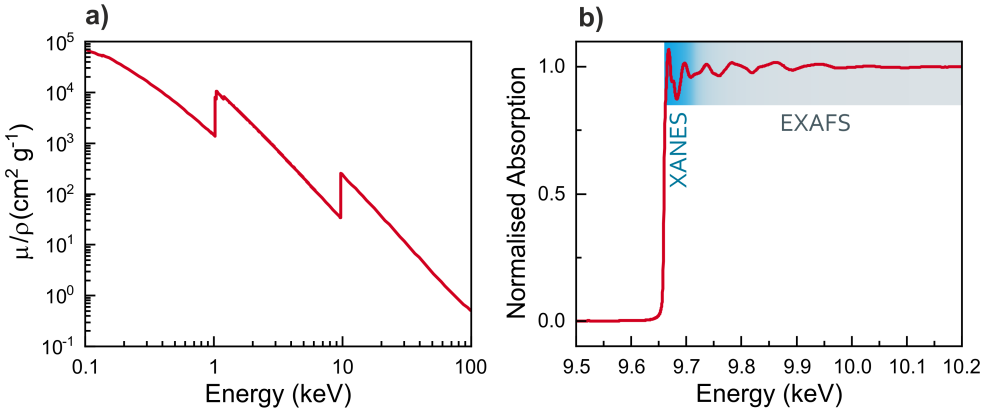

Figure 2.6: (a) Total mass attenuation coefficient of zinc as a function of photon energy.[79,80] (b) K-edge of zinc as experimentally determined within the scope of this dissertation.

Within this thesis, the XANES region was evaluated qualitatively concerning the position and intensity of features at the edge in order to follow the progress of a chemical reaction in Publication **4**.[82] In the EXAFS region, oscillations are visible, which are primarily due to interference of generated photoelectrons with themselves. After a photoelectron has been emitted from the central atom, it propagates as a spherical wave that can be scattered back when it hits neighbouring atoms. This leads to constructive or destructive interference at the point of origin, which according to Fermi's golden rule changes the probability of absorption of the photon in the first place.[83]

The EXAFS spectrum, χ, is defined as the normalised, oscillatory part of μ, and can be modeled as a function of a "photoelectron momentum index", $k = \sqrt{E - E_0}$, as follows:[84]

$$\chi(k) = \sum_R S_0^2 N_R \frac{|f(k)|}{kR^2} \sin(2kR + 2\delta_c + \Phi) e^{-2R/\lambda(k)} e^{-2\sigma^2 k^2} \qquad (2.24)$$

This and related relationships are known as "the EXAFS equation", with the following parameters describing the atomic structure under investigation: the interatomic distances, R, coordination numbers (concerning equivalent scatterers), N_R, and the root mean square, σ, of bond length variations. Further, S_0^2 is an amplitude factor, accounting for the altered orbital geometry after ionisation of the central atom and thus lower similarity of the initial and final state. $f(k)$ is the backscattering amplitude, incorporating the possibility of elastic scattering at nearby atoms, which is energy-dependent but also element-specific, potentially facilitating the identification of nearby atoms. During the excitation and scattering process, the photoelectron moves out of the potential well of the central atom, then into that of the scattering atom, and back again. Thus, the frequency of the electron's wave function changes throughout, and it may exhibit a phase shift, δ_c, when it returns to the central atom. To account for phenomena other than elastic scattering at neighbouring atoms, the XAFS mean free path, $\lambda(k)$, is introduced, essentially mod-

elling how far the photoelectron can freely move. Lastly, Φ is the argument of $f(k)$ and accounts for the wavelike nature of the backscattering.[81,84]

For this dissertation, the software ProQEXAFS was used to extract, normalise and interpolate XAS data which were then fitted using the Demeter software package to obtain N_R, R, and σ.[85,86]

3 COMPREHENSIVE SUMMARY AND DISCUSSION

Within the framework of this dissertation, four research projects were undertaken, resulting in three peer-reviewed publications,[34,66,82] a correction,[87] and a manuscript to be published. The publications and aforementioned manuscript can be found in chapter 4.

This work includes collaborations with the German Federal Institute for Risk Assessment (BfR) in Berlin, concerning the artificial digestion of commercially available zinc oxide nanomaterials,[66] and the Paul Scherrer Institute (PSI) in Villigen, Switzerland, for *in situ* X-ray absorption fine structure (XAFS) measurements.[82]

The two focal points of this work are the synthesis of nanomaterials and their characterisation, with an emphasis of employing small-angle X-ray scattering (SAXS). To which topic the four projects in this dissertation correspond to is laid out in Table 3.1.

Table 3.1: Overview over the four projects of this dissertation

Synthesis-focused		**SAXS-focused**	
1	Microwave-Assisted Synthesis of Ultrasmall Zinc Oxide Nanoparticles[34]	**3**	Environmental Impact of ZnO Nanoparticles Evaluated by in Vitro Simulated Digestion[66,87]
2	Phase Transfer of Ultra-small ZnO Nanoparticles to Aqueous Medium	**4**	Zinc Phosphate Nanoparticles Produced in Saliva[82]

Project **1** is based on the adaptation of the synthesis of oleate-functionalised zinc oxide nanoparticles, previously published by Ehlert et al.,[30] to create a microwave-assisted, one-pot synthesis method.[34]

Therein, a solution of zinc oleate in tetrahydrofuran was reacted with a solution of tetrabutylammonium hydroxide in methanol to obtain a dispersion of luminescent zinc oxide nanoparticles with adjustable radii and interrelated optical and lattice properties. Project **2** was aimed at the phase-transfer of these particles into an aqueous dispersion to enable application in water or biological media, e.g. as catalyst or fluorescent probes. This was facilitated by coating them with polysorbate 80, which induced a particle growth that was monitored with *in situ* SAXS measurements.

While SAXS has already been used as characterisation method in each of the projects mentioned above, each one focused primarily on the production of nanostructures with favourable properties. In contrast, projects **3** and **4** focused on the investigation of non-tailored samples using SAXS. The artificial digestion of commercially available zinc oxide nanoparticles was carried out in project **3**, and structural changes during the digestive process were monitored.[66] In the course of these investigations, the formation of nanostructures in reference samples containing solubilised zinc chloride became

evident and was further investigated by SAXS, WAXS, and XAFS measurements in project **4**. Project **3** was carried out in collaboration with BfR and project **4** with PSI.

Project **1** (Publication in Section 4.1) was motivated by previous experience with microwave-assisted synthesis, based on which an enormous acceleration of the synthesis by this kind of reaction in an autoclave-like system at temperatures above that of the solvent boiling point was expected.[35] In fact, the reaction time could be reduced by more than 99 % when compared to the synthesis at ambient pressure, and by varying the reaction temperature and time, the particle radii became tunable.

For instance, five minute long syntheses at temperatures increasing from 125 °C to 200 °C yielded particles with increasing average zinc oxide core radii in the range of (2.6 ± 0.1) nm to (3.8 ± 0.1) nm, determined from SAXS. These particle systems P_{125}, P_{150}, P_{175}, and P_{200} were narrowly disperse in size, displaying similar relative distribution widths of around 10 %. The oleate is expected to determine the stability of the particles in the dispersion medium and to have an impact on the final particle shape and size. In contrast to SAXS, where this shell is practically invisible due to the comparably high scattering contrast of zinc oxide, complementary DLS measurements allowed for the determination of the shell thickness. For P_{125} - P_{175}, comparable shell thicknesses of (3.3 ± 0.2) nm to (4.1 ± 0.2) nm indicated that the particles are stabilised by at least two molecular layers, while degradation of the stabiliser is assumed to set in for P_{200}, leading to a slightly increased shell thickness of 4.9 ± 0.2 nm.

These particle systems are particularly suitable for the investigation of correlations between particle size and optical and structural properties. Therefore, using UV/Vis and fluorescence spectroscopy, the band gap and fluorescence energies were determined and linked to the zinc oxide core radii (Figure 3.1). Therein, the dependence of the band gap energy (E_g, red symbols) on the core radius is shown according to equation 3.1 (solid red line) with the 95 % confidence interval (light red shaded area). This result is between theoretical (lower dashed line) and empirical (upper dashed line) literature data.[27]

$$E_g = 3.37 - \frac{0.51 \pm 0.10}{R_0} + \frac{1.72 \pm 0.27}{R_0^2} \tag{3.1}$$

In contrast to the band gap energy, the fluorescence energy (E_{fl}, blue symbols) decreases linearly with increasing core radius according to equation 3.2 (solid blue line), with 95 % confidence intervals shown as the light blue shaded area.

$$E_{fl} = (2.51 \pm 0.02) - (0.12 \pm 0.01) R_0 \tag{3.2}$$

While Jacobsson and Edvinsson found E_{rel}, the ratio of E_{fl} and E_g, to be constant at a value of 62.5 ± 0.4 %[27] (green line with light green shaded area, right in figure 3.1), in this project, E_{rel} (green symbols) decreased significantly alongside increasing core radius.

Similar to quantum dots, changes in optical properties of ZnO nanoparticles are attributed to particle size changes, though the underlying mecha-

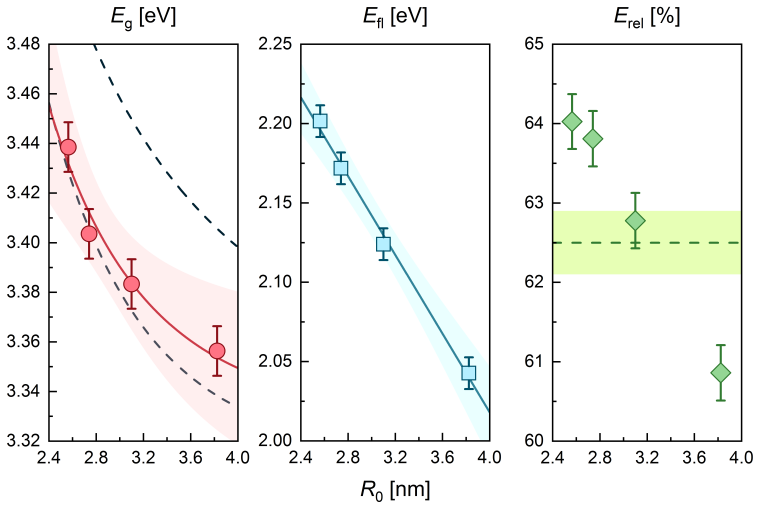

Figure 3.1: Band gap energies E_g, fluorescence energies E_{fl} and the ratio E_{rel} of E_{fl} and E_g – symbols, respectively – plotted against the mean particle core radii R_0. Dashed lines correspond to theoretical (lower line) and empirical (upper line) literature data for $E_g(R_0)$,[27] and E_g was fitted as a function of R_0 according to equation 2.1 (red line). $E_{fl}(R_0)$ was approximated as a linear function (blue line). Light red and blue shaded areas represent 95 % confidence intervals. Literature data for E_{rel} (green line) with uncertainties (light green shaded area) is given for comparison.[27,34]
Reprinted with permission from *Langmuir* **2019**, 35, 38, 12469–12482.
Copyright 2019 American Chemical Society.

nisms for this are not yet fully understood.[25,28] To investigate the correlations of optical properties with crystal structure in detail, wide-angle X-ray scattering (WAXS) measurements were performed. These confirmed the formation of zinc oxide in the hexagonal wurtzite structure, which is its thermodynamically most stable form.[15]

In addition to the identification of the crystal structure, WAXS measurements enable the size determination of the crystallites by analysis of the peak widths.[71] A distinction has to be made between the broadening due to particle size, as according to Scherrer, and the instrument broadening, the former being representable by a Lorentz profile and the latter by a Gaussian profile.[67–69] Therefore, the experimental values are to be regarded as the result of the convolution of a Lorentz and a Gauss profile and need appropriate correction to determine the sample-induced peak broadening. To the best of our knowledge, this type of correction has not been applied previously, and we assume that the presence of this convolution is the pertinent case for WAXS/XRD profile analysis of small nanoparticles. From the peak broadening values, the ZnO nanoparticles were identified as single crystals with crystallite sizes, corresponding to particle diameters, between 4.55 ± 0.13 nm (P_{125}) and 8.00 ± 0.37 nm (P_{200}).

Furthermore, the impact of the choice of correction type, i.e. correction for two same profiles or no correction at all, on the resulting crystallite size was discussed in detail. When both the sample-induced and the instrumental peak broadening are of a similar magnitude, the choice of correction

strongly influences the determined crystallite size. However, it is only of minor importance when the instrumental broadening is comparatively small.

Three variants of the Williamson-Hall model were employed to determine further structural parameters: the uniform deformation model (UDM) for determination of the lattice strain, ϵ, the uniform stress deformation model (USDM) for determination of the lattice stress, σ, and the uniform deformation energy density model (UDEDM) for determination of the deformation energy density, u.[72,73] These values increase with decreasing crystallite size (see Figure 3.2), and were compared to data from other studies.[69,73,88–97]

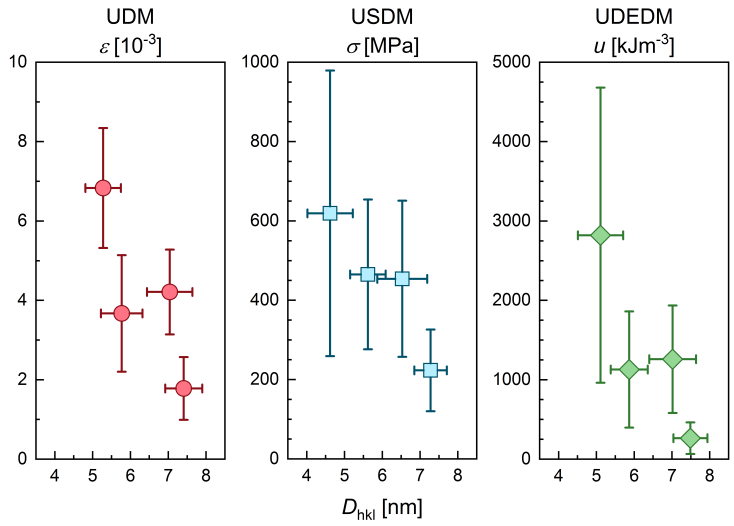

Figure 3.2: Lattice strain, ϵ, lattice stress, σ, and the deformation energy density, u, in dependence of the crystallite size, D_{hkl}, as obtained from the following variants of the Williamson-Hall model: uniform deformation model (UDM), uniform stress deformation model (USDM), and uniform deformation energy density model (UDEDM).

We found that their size-dependencies could be approximated with power law scaling functions for crystallite sizes below 20 nm as follows:

$$\epsilon = k_\epsilon D_{\mathrm{hkl}}^{-p_\epsilon} \tag{3.3}$$

$$\sigma = k_\sigma D_{\mathrm{hkl}}^{-p_\sigma} \tag{3.4}$$

$$u = k_u D_{\mathrm{hkl}}^{-p_u}, \tag{3.5}$$

where k is the scaling constant and p is the power law exponent. Application of equations 3.3, 3.4, and 3.5 resulted in the constants $k_\epsilon = (37 \pm 18) \times 10^{-3}$, $k_\sigma = (4.2 \pm 1.6) \times 10^3$ MPa, and $k_u \approx 1.6 \times 10^5$ kJ m^{-1}, respectively, which correspond to the hypothetical values for strain, stress, and deformation energy density of crystallites with a size of one nanometer. The power law exponents were determined as $p_\epsilon = 1.2 \pm 0.3$, $p_\sigma = 1.2 \pm 0.2$, and $p_u = 2.8 \pm 0.8$. We speculate that such a power law scaling generally applies to zinc oxide nanoparticles smaller than a certain threshold size, and perhaps to other materials as well, each with their respective scaling constant, k, and exponent, p.

After this detailed investigation on how reaction conditions affect the resulting system of oleate-coated zinc oxide nanoparticles, the project **2** (Publication in Section 4.2) aims to expand the potential areas of application, which are limited by the hydrophobic particle functionalisation. With regard to the adjustable optical properties, for instance, biological *in vitro* or *in vivo* applications are possibilities, for which a phase transfer into an aqueous environment is required. Thus, the particles from project **1** were transferred into an aqueous dispersion in project **2**, employing polysorbate 80 (polyoxyethylene (20) sorbitan monooleate, trade name Tween 80) to assist the phase-transfer. This surfactant comprises both hydrophilic polyoxyethylene and hydrophobic oleate groups, and may thus be able to mediate between the hydrophobic particle surface and the aqueous dispersion medium, as implied by Ren et al. for the corresponding phase transfer of upconversion nanoparticles ($NaYF_4$:Yb,Er).[98]

For the phase transfer, polysorbate 80 and water were successively added under stirring to a particle dispersion in cyclohexane, synthesised at a reaction temperature of 125 °C, as described in project **1**. In this context, the initial particle system is referred to as P_0 before, and as P_{0+TW} after, the addition of polysorbate 80. Subsequently, heating the sample to a temperature of 90 °C in an open flask facilitated evaporation of the organic phase and supported the phase transfer into the aqueous medium. This process was completed after four hours, and, alternatively, particle systems were also produced with shorter heating times with the removal of excess cyclohexane performed through rotary evaporation. Depending on the heating time, i, in minutes, the obtained samples are designated as H_i from here on.

The particle systems were characterised before and after phase transfer using SAXS to determine the sizes of the ZnO cores and the stabiliser shells. As in project 1, SAXS curves were analysed assuming log-normal particle size distributions to determine the distribution parameters. For the presentation of the SAXS data as well as the curve fits and size distribution plots, reference is made to the manuscript (Section 4.2). The SAXS data was complemented by DLS analysis, from which a layer thickness of the stabiliser of 2 nm to 4 nm was estimated in all cases. Thus, no significant influence of the phase transfer procedure on the stabiliser shell thickness of the nanoparticles was found.

The initial particle system P_0 exhibited a mean radius, R_{mean}, of 2.3 ± 0.1 nm with a distribution width, σ, of 0.3 ± 0.1 nm. With regard to the particle system P_{0+TW} it was established that the addition of the surfactant to the organic particle dispersion had no significant influence on the size of the ZnO cores or inter-particle interactions.

After addition of water and the removal of cyclohexane in vacuum, without intermediate heating of the dispersion, the particle system H_0 was obtained in aqueous medium. Before particle characterisation, the dispersion was centrifuged to remove aggregates that may have formed during phase transfer. Here the SAXS curve was indicative of particle sizes as in the initial organic dispersion, besides a contribution of larger particles with $R_{mean} = 7.2 \pm 0.1$ nm and a numerical contribution of less than 1% to the overall size distribution. This particle population is interpreted as aggregates of 33 ± 2 primary particles, whereas this aggregation number would

appear not to be large enough to remove all aggregates by centrifugation alone.

Regarding the optical properties, the initial and final particle systems P_0 and H_{240} were analysed using UV/Vis and fluorescence spectroscopy. A redshift of the optical band gap and luminescence energy was found, as could be expected from project **1** for growing ZnO nanoparticles at the lower end of the nanoscale. However, the optical properties may also depend on the dispersion medium or the particle stabiliser, and a determination of the relative influence of these parameters on the optical properties was outside the scope of this project.

In order to investigate the necessity of removing the cyclohexane for a successful phase transfer, it was also carried out in a microwave-assisted fashion in a closed system. Thereby, all solvents remained in the system and after the 240 min long heating process, a turbid, mainly organic, and an opalescent, mainly aqueous phase were obtained. The latter may have been a microemulsion of cyclohexane in water, mediated by the stabilisers, with the ZnO nanoparticles still locally dispersed within the cyclohexane. The ZnO core radii determined by SAXS matched those of the H_{240} particle system before and after removal of the cyclohexane on the rotary evaporator. The removal of cyclohexane either through heating or by additional pressure reduction did not change the particle size, but was necessary to obtain a purely aqueous dispersion after phase transfer.

Besides possible biological applications, photocatalysis is another potential field of application for these phase-transferred nanoparticles. This was investigated *via* the decolourisation of an aqueous methylene blue solution under irradiation with UV light (wavelength $\lambda = 365\,\text{nm}$). Methylene blue exhibits absorbance bands around energies of 1.8 eV to 2.1 eV; thus, its degradation could be followed *in situ* by UV/Vis spectroscopy (see panel **a** of Figure 3.3). Spectra were recorded at intervals of 10 s, and the absorbance pattern in the range of 1.6 eV to 2.2 eV was modelled using two Gaussian functions f_1 and f_2, and a Rayleigh scattering background, $f_3 = a + b \cdot E^4$, where E is the photon energy and a and b are arbitrary constants (see panel **b** of Figure 3.3).

To determine the reduction of the concentration of methylene blue, $c(t)$, over time, t, the summed area of the two Gaussian functions $\Sigma A(t)$ at $t = 0$ was assigned to the initial concentration $c_0 \simeq 0.95 \times 10^{-5}$ M. Then, a linear decrease of $\ln[c(t)/c_0] = -k_{\text{app}} \cdot t$ was observed for the different samples: water as blank sample, a solution of the stabilizers sodium oleate and polysorbate 80, H_{240}, as well as commercial ZnO and TiO_2 nanoparticles, indicating pseudo-first order kinetics (see panel **a** of Figure 3.4). Thus, an apparent rate constant k_{app} could be obtained by linear regression (see panel **b** of Figure 3.4).

A comparison of k_{app} with the literature is not readily possible, as a large number of parameters influencing k_{app} are not necessarily known to the experimenter. An example is the unknown ratio of the absorption by the particles to the absorbance of the whole system, and thus the impossible determination of the quantum yield.[99] It seems plausible that this may depend, for example, on the geometry of the experimental setup or the type and concentration of the particles. A comparison of the phase-transferred particles was

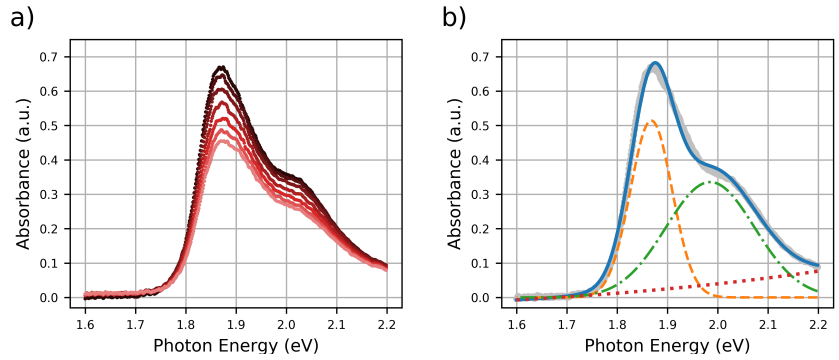

Figure 3.3: UV-Vis analysis of the photocatalytic degradation of methylene blue employing H_{240} particles as catalyst. (a) UV-Vis spectra taken in 300 s intervals, depicting the decrease of absorbance of the dye over time. (b) UV-Vis spectrum at a reaction time of 0 s (silver circles) and curve fit (blue, solid line) with the sum of of two Gaussian functions f_1 and f_2 and a Rayleigh scattering contribution f_3 (orange dashed line, green dash-dotted line and red dotted line, respectively).

therefore carried out within this project with commercially available ZnO and TiO_2 nanoparticles with a size of 25 nm under otherwise identical conditions. This was done under the assumption that the inherent flaws in this experiment did not differ fundamentally between the different particles and was only intended to determine the photocatalytic activity of the particles but not to quantify it precisely. As a result, it was found that the phase-transferred particles catalyse the decolourisation of methylene blue, about half as effectively as commercial ZnO and TiO_2 nanoparticles with respect to the applied particle masses. Accounting for the higher specific surface area of the H_{240} particles as compared to the commercial particles, the catalytic activity is about a quarter as high. Besides, the stabilisers on their own were found to be catalytically active. In conclusion, the phase-transferred particles of this project can be used in catalytic reactions where specific demands are made for particle size or stability in dispersion.

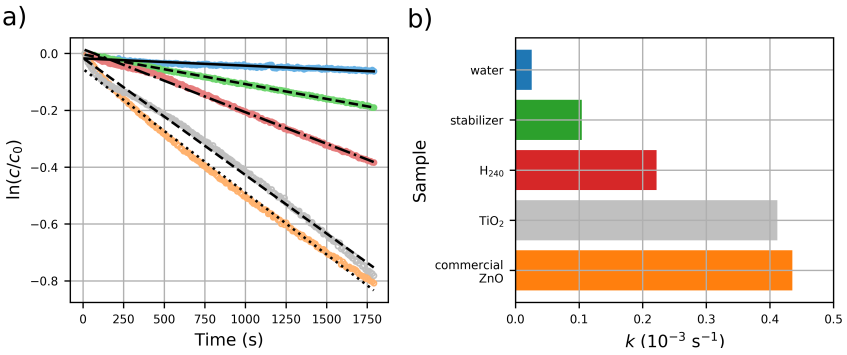

Figure 3.4: (a) Plot of $\ln[c(t)/c_0]$ of methylene blue dye as a function of irradiation time with UV-light for pure water (blue), stabilizer (green), H_{240} (red), TiO_2 (silver) and commercial ZnO (orange), given in the order of increasing steepness of the decrease. Straight lines are linear fits for evaluation of the rate constants. (b) Rate constants derived from the slopes of the curve fits in a).

Moving towards the SAXS-focused part of this dissertation, in project 3, several commercially available zinc oxide nanoparticulate systems, in dispersion or solid powder form, were examined in an artificial digestion process, which was carried out in collaboration with the BfR.[66] This project's main objective was to find out how different zinc species, partly in the presence of food simulants, behave at the different stages of the artificial digestion.

While the BfR collaboration partners selected the zinc species and concentrations to be investigated, the digestion process itself, as well as the SAXS measurements and their evaluation, were carried out at BAM. Complementary atomic absorption spectroscopy measurements were carried out by the BfR collaboration partners. The *in vitro* artificial digestion procedure is laid out in Figure 3.5.

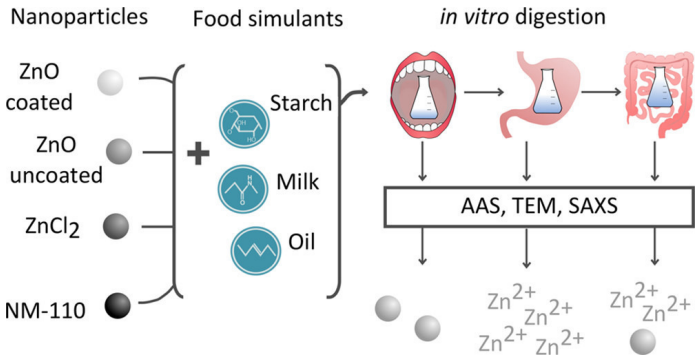

Figure 3.5: Graphical abstract of "Environmental Impact of ZnO Nanoparticles Evaluated by in Vitro Simulated Digestion."[66]
Reprinted with permission from *ACS Appl. Nano Mater.* **2020**, 3, 1, 724-733.
Copyright 2020 American Chemical Society.

The materials selected were silane-coated and uncoated ZnO nanoparticles, $ZnCl_2$ as an ionic zinc reference, as well as the reference material NM-110 from the Joint Research Centre (JRC). These were each dispersed in artificial saliva before enzyme addition, with bovine serum albumin (BSA) as a stabiliser. The first three zinc compounds were probed at initial concentrations of 6.67, 3.33, 0.67, 0.33, and 0.167 mg/mL, and underwent a dilution series during the digestion process from saliva *via* gastric juice to intestinal juice. Digestions of the reference material NM-110 as well as all those in the presence of food simulants (starch, milk, oil, or a mixture thereof) were conducted using initial concentrations of 0.33 mg/mL.

The detection of small nanoparticles in complex media, such as digestive juices, is not trivial but suitable for the application of SAXS. A key point regarding the unique suitability of SAXS is the possibility of examining liquid samples, meaning that only nanostructures that are present during the digestion process are detected, and their formation during sample preparation (e.g. drying prior to electron microscopy) is not a reason for concern. Dissolved salts contained in the artificial saliva would not produce a scattering signal in the q-range under investigation here. For the analysis of the digestion samples, the slit-focus SAXS instrument was used, which is uniquely suited for the examination of weakly scattering samples such as diluted particle dispersions. However, based on the q-range of the instru-

ment of 0.1 nm^{-1} to 4 nm^{-1}, when applying equation 2.14, it becomes clear that this instrument is only suitable for the determination of particle size distributions in the radial range of roughly 1 nm to 30 nm. With regard to this project, the available q range was, therefore, in principle, sufficient for the analysis of structures at the lower nanoscale.

The analysis of spherical, oleate-coated ZnO nanoparticles, as laid out in project **1**, was comparatively simple: small nanoparticles with narrowly-distributed radii around 3 nm were dispersed in an organic solvent and did not aggregate or sediment. In contrast, the particle systems investigated within the scope of this project were more complex and created higher analytical demands. The ZnO samples exhibited primary particle sizes up to several hundred nanometers as well as polydispersity concerning both shape and size. Hence, these samples were considered unsuitable for SAXS analysis and were instead evaluated using transmission electron microscopy and dynamic light scattering. However, SAXS could be used to analyse a *de novo* particle formation at the lower nanoscale. Within the scope of the SAXS data evaluation for this project, a significant particle formation was observed only for particle radii below 10 nm, to which the following explanations will, therefore, be limited.

As an example for the SAXS analysis of digestive samples, with regard to the presence of nanostructures, the uncoated ZnO particles in saliva will be used (670 µg/mL, Figure 3.6).

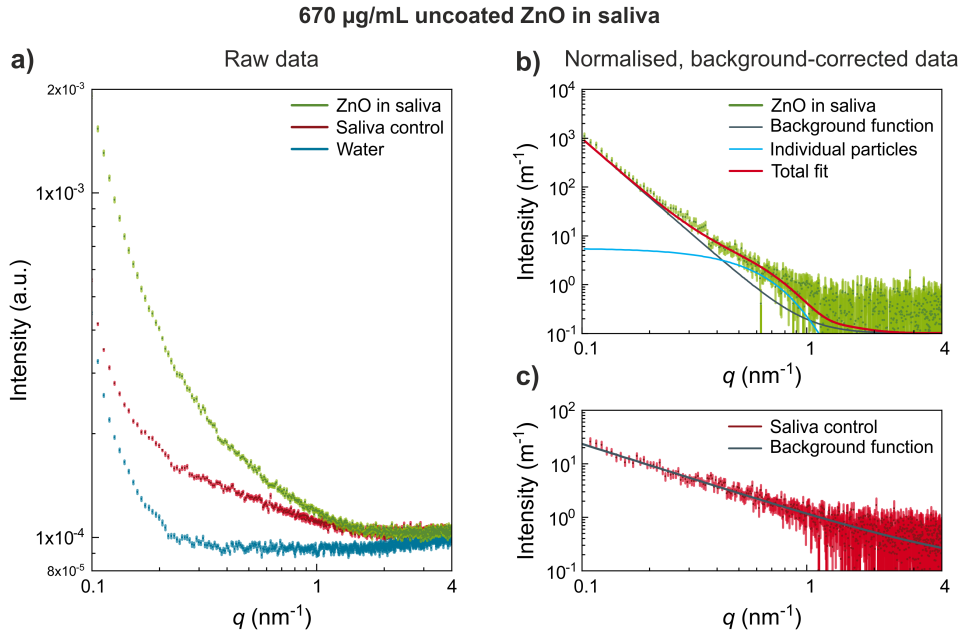

Figure 3.6: SAXS data from 670 µg/mL uncoated ZnO particles in saliva with a) raw data of the ZnO sample, the saliva control sample as background, and water; b) data of the ZnO sample after correction for the saliva background with fitted background function (Equation 2.17) and scattering contribution of spherical particles; and c) data of the saliva control with the fitted background function.

Panel **a** contains SAXS data from water, the saliva control sample (digestive matrix) as well as the denoted ZnO sample. When moving from water

to saliva to ZnO in saliva, a tendency of the scattering curve towards higher intensity is observed. This additional scattering intensity, from the ZnO sample, when compared to the saliva control and water, may indicate the presence of nanostructures, in the radial range of 1 nm to 30 nm as laid out above. To allow for a definitive conclusion concerning this aspect, several data corrections are necessary.[100] In simple terms, the scattering curve of the matrix is subtracted from that of the sample in order to solely obtain the scattering signal of the sample and feed it into the data analysis. These operations were performed on both sample (panel **b**) and control data (panel **c**), subtracting the scattering curve of the saliva control data from that of the ZnO sample, and that of water from the saliva control. Thereby, normalised and background-corrected data was obtained, ready for analysis concerning the presence of nanostructures. Detectable nanostructures here can be of three main origins: they are already contained in the sample to be digested, they are contained in the digestive matrix, or they are formed during the digestion process. With regard to the first case, the scattering curves taken from the undigested, particulate samples were not evident of any such structures. The digestive matrix contains enzymes, and as such, its scattering curve could be expected to be evident of nanostructures. However, this is not expected to cause any issue in the analysis of the ZnO sample scattering curve, as that of the digestive matrix was subtracted.

Structures with a smooth surface that are larger than the upper limit of 30 nm would produce a scattering signal that decays with q^{-4} in the q-range under investigation. Correspondingly, their scattering contribution was modeled as a background function, I_{bkg}, according to equation 2.17 with $p = 4$. This means that the actual size of such structures cannot be derived from the SAXS measurements undertaken here. Similarly, if the scattering curve can be modelled according to equation 2.17, but with $p \neq 4$, the particle size cannot be determined either, and could also be smaller than R_{max}.

However, any scattering contribution on top of this background function could indicate the presence of nanostructures. This is depicted in panel **b** of Figure 3.6, where the scattering curve (green) is modelled as the sum (red) of a background function according to equation 2.17 (grey), representing structures too large to be resolved, and a contribution from spherical nanoparticles (blue). Thus, the presence of nanostructures in the sample, besides structures too large to be resolved, has been proven. Although the determination of their chemical composition did not fall within the scope of this project, it is assumed that nanoscale zinc phosphate is formed, as will be discussed in more detail later. A model of log-normally distributed, spherical particles was employed for fitting this population, yielding volume-weighted values of $R_{\mathrm{mean}} = 3.5 \pm 0.1$ nm and $\sigma = 0.7 \pm 0.1$ nm as well as number-weighted values of $R_{\mathrm{mean}} = 3.1 \pm 0.1$ nm and $\sigma = 0.6 \pm 0.1$ nm. Details on the functions used for curve fitting are given in section 2.3.2.

At this point, it should be emphasised that any scattering contribution of nanostructures present in the digestive matrix has been removed from the sample scattering curve by background subtraction, and the saliva control curve is depicted in panel **c** of Figure 3.6 (red). Alongside the data, a background function according to Equation 2.17 is depicted (grey), showing that the data can be fitted sufficiently well using only said background. This

means that no nanostructures in the size range of 1 nm to 30 nm could be detected in the digestive matrix, but a population with dimensions around 3 nm is present in the investigated sample of digested ZnO particles. This does not prove the absence of nanostructures in the digestive matrix; on the contrary, the size of the added proteins is on the nanoscale. However, the data available here, on its own, is not sufficient to prove the presence of nanostructures. The reason for this is possibly the comparatively low scattering contrast of biopolymers, which could lead to an overshadowing of their scattering signal by that of inorganic components of the saliva. For example, precipitation of $CaSO_4 \cdot 2\,H_2O$ can be expected due to its low solubility, and at sizes >30 nm the scattering signal could easily mask that of biopolymers. Zinc oxide or zinc phosphate nanostructures, on the other hand, could still contribute significantly to the measured scattering curve, as in the example in panel **b**, since those would have a higher scattering contrast than $CaSO_4 \cdot 2\,H_2O$.

All samples of the aforementioned, different zinc compounds and concentrations were subjected to the artificial digestion process. After passing through the salivary, gastric and intestinal stages, SAXS measurements were taken and processed to obtain the sample scattering curves ready for analysis. Raw and processed data are depicted in the supporting information of the publication (Chapter 4.3). To begin with, it can be stated that detectable structures, i.e. those causing a scattering contribution exceeding the background, were present in all saliva and intestinal juice samples, while in the gastric juice all zinc species were dissolved, as is to be expected in acidic environments. This does imply a *de novo* particle formation in the intestine and thus that after intermittent particle dissolution in gastric juice, zinc species may reach the intestine in particulate form. However, exact particle sizes in terms of mean radius, R_{mean}, and distribution width, σ, could only be determined in some saliva samples, as discussed in the following. In the remaining saliva samples and all intestinal samples, the scattering curves did not exhibit any distinct characteristics and could be fitted with the background function alone (equation 2.17), i.e. it was not possible to determine particle sizes. Thus in the following, results will be presented where a systematic comparison between samples can be made.

For samples without food components added, R_{mean} and σ could be determined for uncoated ZnO and solubilised $ZnCl_2$ at initial concentrations of 167 µg/mL to 670 µg/mL (Figure 3.7), and were found in ranges of roughly 3 nm to 6 nm and 0.6 nm to 1.2 nm, respectively. For the analysis of the $ZnCl_2$ samples, the hard-sphere structure factor, $S_{\mathrm{hs}}(q, R, \varphi)$, with an average volume fraction of $\varphi = 0.27 \pm 0.07$ was employed to model particle-particle repulsion. While both R_{mean} and σ were decreasing with increasing concentration of uncoated ZnO, for $ZnCl_2$ they were essentially constant, at the lower limit, over the concentration range.

It is striking that these particle populations were not present in the samples before digestion: the ZnO sample consisted of much larger particles, and the $ZnCl_2$ sample of a completely dissolved solution. However, the formation of phosphate-compounds from ionic zinc in phosphate-containing solutions such as phosphate-buffered saline, or potentially the artificial saliva used here, is a known issue in literature.[101] Therefore, a similar mech-

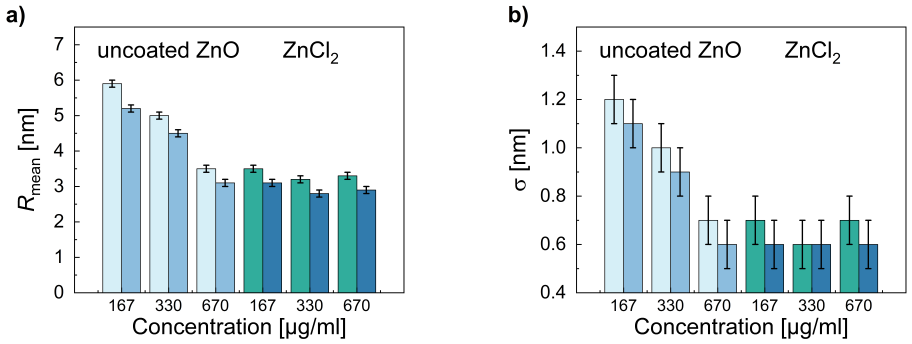

Figure 3.7: SAXS-derived mean radius (a) and size distribution width (b) of particles found in saliva upon addition of uncoated ZnO nanoparticles and $ZnCl_2$, with each pair of bars representing one concentration. Left and right bars denote characteristics of volume- and number-weighted data, respectively.[66]
Reprinted with permission from *ACS Appl. Nano Mater.* **2020**, 3, 1, 724-733.
Copyright 2020 American Chemical Society.

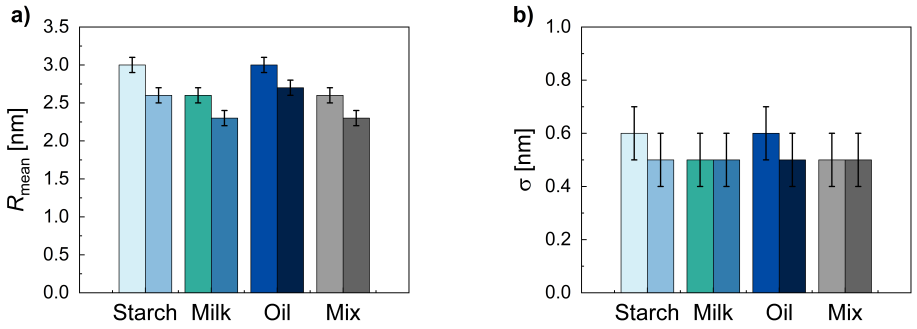

Figure 3.8: SAXS-derived mean radius (a) and size distribution width (b) of particles found in saliva upon addition of 330 µg/mL $ZnCl_2$ in the presence of the denoted food component. Left and right bars denote characteristics of volume- and number-weighted data, respectively.[87]
Reprinted with permission from *ACS Appl. Nano Mater.* **2020**, 3, 5, 4914.
Copyright 2020 American Chemical Society.

anism was suggested, which leads to a *de novo* particle formation in the $ZnCl_2$ sample. And indeed, within the scope of project **4**, the formation of $Zn_3(PO_4)_2 \cdot 4\,H_2O$ could be proven. With regard to zinc oxide, which is insoluble in water, a mechanism is proposed in which etching of the surface occurs, as has already been observed in physiological environments.[102]

During oral ingestion of nanoparticles, their mixing with food components seems likely; hence the digestive process was also performed in the presence of starch, skimmed milk powder, olive oil, and a mixture thereof as food simulants. The obtained SAXS curves were evaluable for samples with 330 µg/mL of $ZnCl_2$, and were evident of particles with mean radii of 2.3 nm to 3.0 nm and distribution widths of 0.5 nm to 0.6 nm (Figure 3.8).

For analysis, $S_{\mathrm{hs}}(q, R, \varphi)$ with a volume fraction of $\phi = 0.06 \pm 0.02$ was employed in the case of starch being added to the sample, and $S_{\mathrm{agg}}(q, D, r_0, \xi)$ to model particle aggregation into mass fractals in the remaining cases. For the latter, the aggregate size was set to the upper resolution limit of the measurement, $\xi = 30$ nm, and curve fitting yielded individual particle radii, r_0, that

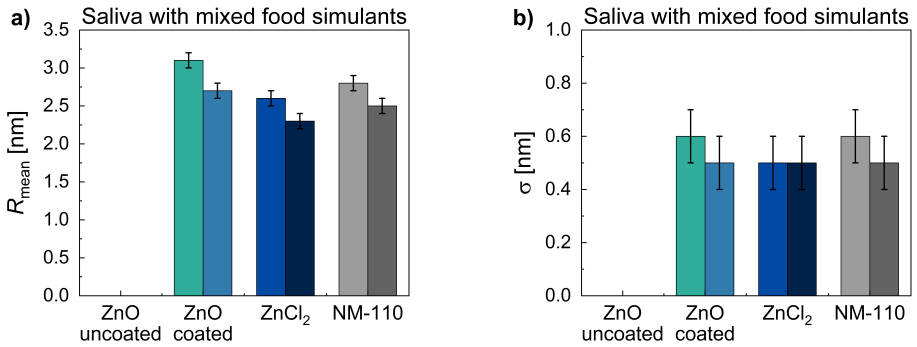

Figure 3.9: SAXS-derived mean radius (a) and size distribution width (b) of particles found in saliva upon addition of 330 µg/mL ZnO coated, $ZnCl_2$ and NM-110 in the presence of the mixed food components. Left and right bars denote characteristics of volume- and number-weighted data, respectively.[66]
Reprinted with permission from *ACS Appl. Nano Mater.* **2020**, 3, 1, 724-733.
Copyright 2020 American Chemical Society.

corresponded to R_{mean} in each case, and a fractal dimension of $D = 2.8 \pm 0.1$ that indicates a relatively dense particle packing in the aggregate. With $r_0 = R_{mean}$ it can be said that no significant layer around the particles could be detected. As will be demonstrated later in the context of project **4**, the case of $r_0 > R_{mean}$ is possible if a shell of negligible scattering contrast surrounds the particles. Therefore, r_0 depicts a particle core/shell radius.

Furthermore, R_{mean} and σ could be determined for the samples with coated ZnO and the reference material NM-110 in the presence of a mixture of the food simulants, and were compared with the corresponding dataset of $ZnCl_2$ (Figure 3.9). For the sample with uncoated ZnO particles, the scattering curve was fitted sufficiently well with only the background function; hence no particle sizes were obtainable.

For the three evaluable samples, mean radii were found in the range of 2.3 nm to 3.1 nm with distribution widths of roughly 0.5 nm, implying that the structure of the zinc source has no major influence on the observed *de novo* particle formation. The presented SAXS results with the observed particle dissolution and formation behaviour were confirmed by ion release measurements, which were performed by the BfR collaboration partners using atomic absorption spectroscopy.

Summarising, project **3** showed that a *de novo* formation of small nanostructures is possible upon contact of ZnO or $ZnCl_2$ with saliva, which is largely independent of the size, concentration or functionalization of the ingested substances, or the presence of food simulants. After intermittent dissolution in the gastric juice, the intestinal juice causes a renewed particle formation, which is thought to lead to zinc phosphate compounds in all cases. However, the assessment of the potential implications of these findings concerning the toxicity or applicability of zinc-containing compounds or products was outside the scope of this project.

The comprehensive characterisation of the structures formed by ionic zinc species during the artificial digestion of project **3** is of great interest due to their possible specific effects to humans. Dissolved zinc salts are ubiquitously applied in various cosmetic products, which are permitted to contain

ionic zinc at concentrations up to 1% in the European Single Market.[103] Toxicological assessments and resultant clearances of the originally ingested substances do not exclude the possibility that during the digestion process, both chemically and structurally different substances may form, which in turn could exhibit different toxicological properties. Therefore, as a comparable model experiment, $ZnCl_2$ was used at a mass fraction of $\approx 0.13\%$ in project **4**.[82] The structures formed upon contact of $ZnCl_2$ with saliva were examined employing SAXS and WAXS measurements on the point-focus instrument as well as XAFS investigations at the Swiss Light Source's SuperXAS beamline (PSI, Villigen, Switzerland). As in project **3**, no toxicological assessment is intended nor is it the objective of this project, however, it could stimulate further investigations.

Throughout this project, five samples were prepared and characterised: 6.8% $ZnCl_2$ in H_2O (sample A), artificial saliva (sample B), and their combination product of 0.13% $ZnCl_2$ in saliva, which was examined after five minutes (sample C), seven hours (sample D), and after a storage period of two weeks (sample E). SAXS curves were obtained from samples B, C, D, and E, with sample B acting as a background for the subsequent three samples. XAFS measurements were performed on the zinc-containing samples A, C, D, and E, while WAXS measurements were performed on all samples. The identification of the products formed was complemented by infrared spectroscopy measurements of sample C. Exact values obtained from data analysis can be found in the corresponding publication (section 4.4).

Sample B functioned as background for the SAXS data analysis, which was conducted as in project **3**, assuming log-normal distributions of spherical particles and modelling particle aggregation with the mass fractal structure factor, $S_{\mathrm{agg}}(q, D, r_0, \xi)$. Furthermore, a background function decreasing with q^{-4} was employed to represent structures larger than roughly 250 nm in radius. From this analysis, particle number densities, N, mean radii, R_{mean}, distribution widths, σ, particle core/shell radii, r_0, and aggregate sizes, ξ, were obtained. The change of these parameters over time is depicted as a scheme in Figure 3.10.

Within five minutes after addition of $ZnCl_2$, aggregates of primary particles with a mean radius of $R_{\mathrm{mean}} = 1.1 \pm 0.2\,\mathrm{nm}$ and a distribution width of $\sigma = 0.7 \pm 0.2\,\mathrm{nm}$ were detected. These values did not change significantly throughout the following two weeks, indicating that primary particles are present from the beginning and only their number density, chemical composition or interaction within the aggregates are expected to change. While in the beginning, the particle number density, N, is around $5 \times 10^{15}\,\mathrm{mL}^{-1}$, it grows by a factor of around 20 over the course of two weeks, which is accompanied by a growth in aggregate size from $\xi \approx 16\,\mathrm{nm}$ to just over 22 nm. Likewise, the radius of gyration and aggregation number increase from $R_g \approx 37\,\mathrm{nm}$ and $N_{\mathrm{agg}} \approx 4000$ to values of approximately 49 nm and 9000, respectively. The mean core/shell radius displays a contrasting behaviour with an initial decrease from $2.2 \pm 0.2\,\mathrm{nm}$ to $1.7 \pm 0.1\,\mathrm{nm}$ over the course of seven hours, indicating the particles became more densely packed, and subsequent constancy within uncertainties.

In characterising the material composition of the produced particles, it initially seemed reasonable to assume that they consist of a water-insoluble

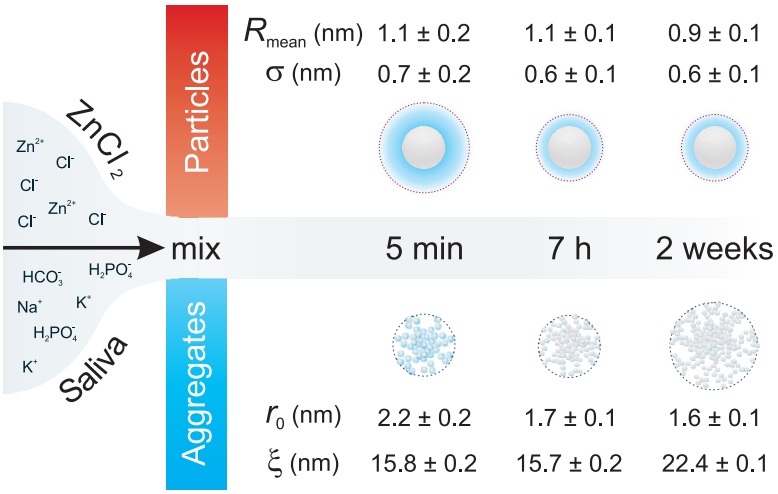

Figure 3.10: Scheme depicting the changes in particle size distribution parameters of primary particles and their aggregates over time, regarding mean particle core radius, R_{mean}, size distribution width, σ, mean particle core/shell radius, r_0, and aggregate radius, ξ.[82]

compound of zinc and one or more of the saliva components. A precipitate was observed only after combining aqueous solutions of $ZnCl_2$ with KH_2PO_4 and $NaHCO_3$, so that the dried products were compared with sample E through infrared spectroscopy. The results indicated the formation of a phosphate compound in sample E, and WAXS measurements of samples A to E were performed for precise identification and tracking of the reaction process (Figure 3.11). The absence of features from the scattering pattern of $ZnCl_2$ (sample A) in all subsequent samples indicates that the initial compound has undergone a chemical transformation. Crystalline material was found already in saliva (sample B), which was identified as calcium sulfate dihydrate ($CaSO_4 \cdot 2\,H_2O$), presumably formed from calcium chloride dihydrate ($CaCl_2 \cdot 2\,H_2O$) and sodium sulfate decahydrate ($Na_2SO_4 \cdot 10\,H_2O$) contained within the saliva. After five minutes of incubation in saliva (sample C), two small, broad diffraction peaks at $q = 9.56\,nm^{-1}$ and $11.16\,nm^{-1}$ become observable (asterisks), and remain present for at least seven hours (sample D). No significant amounts of other crystalline material were formed during the first five minutes of incubation, and no signals from a zinc phosphate compound could be detected. After seven hours the diffraction signals of $Zn_3(PO_4)_2 \cdot 4\,H_2O$ become visible (sample D), and persist over the following storage period of two weeks (sample E), after which no additional diffraction is detected.

These investigations suggest that the formation of $Zn_3(PO_4)_2 \cdot 4\,H_2O$ proceeds *via* an intermediate, possibly hydrozincite ($Zn_5(CO_3)_2(OH)_6$), which exhibits diffraction peaks at similar positions to those of the minor diffraction peaks observed in samples C and D (ICSD collection code 16583).[106] As reported in the literature, when in the presence of organic molecules, a delayed crystallisation of $Zn_3(PO_4)_2 \cdot 4\,H_2O$ can occur due to the formation of amorphous intermediate species.[107,108] Hence, it is assumed that the crystallisation of $Zn_3(PO_4)_2 \cdot 4\,H_2O$ is delayed due to the presence of organic

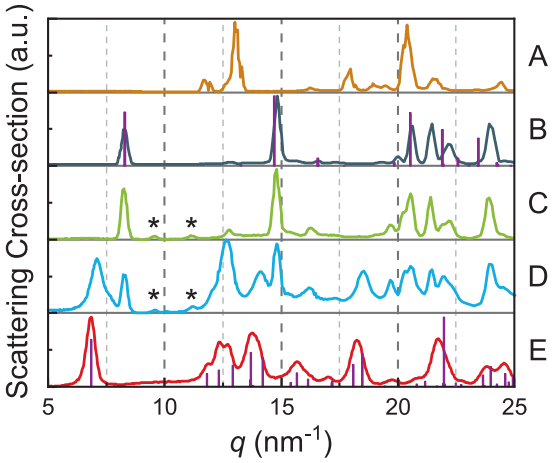

Figure 3.11: Wide-angle X-ray scattering data of samples A - E (solid lines) and reference data for $CaSO_4 \cdot 2\,H_2O$ (bars at sample B) and $Zn_3(PO_4)_2 \cdot 4\,H_2O$ (bars at sample E), taken from ICSD Collection Codes 161622[104] and 1945,[105] respectively.[82]

compounds in the artificial saliva and is therefore only observed in samples D and E.

To verify the assumptions made so far, XAFS measurements were carried out to follow the reaction progress in the X-ray absorption near-edge structure (XANES), and to determine coordination numbers of zinc with regard to chlorine and oxygen from the extended X-ray absorption fine structure (EXAFS) (Figure 3.12).

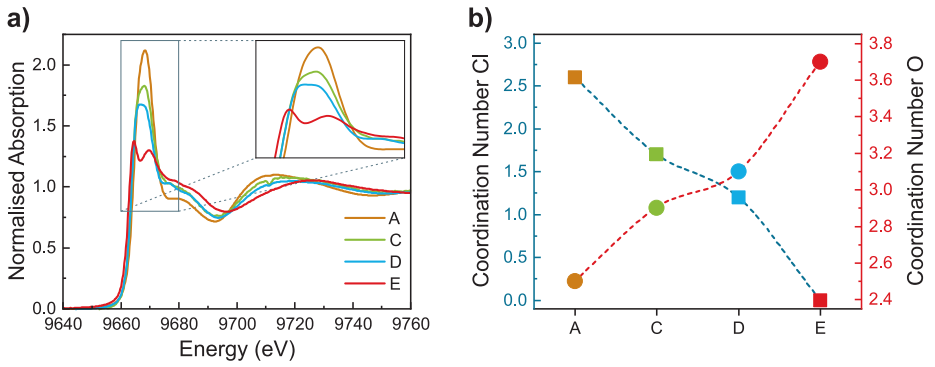

Figure 3.12: XAFS data with a) XANES spectra measured at the Zn K-edge of samples A, C, D, and E, and b) coordination numbers of zinc with regard to chlorine (squares, left axis of ordinate) and oxygen (circles, right axis of ordinate) as determined from fitting to the EXAFS region.[82]

From the XANES (panel **a**) of Figure 3.12), a significant change in the Zn K-edge, with decreasing white line intensity upon injection of $ZnCl_2$ into saliva (sample C), is observed when compared to the aqueous solution of $ZnCl_2$ (sample A). This trend progresses throughout the following seven hours to sample D, albeit slower and manifests itself in a doublet splitting of the absorption edge for sample E, after two weeks of storage. This transfor-

mation from a single initial edge at an energy of 9668 ± 1 eV (sample A) into the two distinct absorption peaks at 9664 ± 1 eV and 9670 ± 1 eV for sample E can be followed in more detail in the inset of Figure 3.12. The absence of isosbestic points, in the XANES data, indicates the possible involvement of an intermediate species, in line with the assumption from the WAXS data. Due to this, linear combination fitting of the precursor and product data was not possible, and the exact nature of the possible intermediate could not be elaborated upon from the data. However, as two different methods point to the involvement of an intermediate such as $Zn_5(CO_3)_2(OH)_6$, which exhibits a lower solubility than the eventually detected $Zn_3(PO_4)_2 \cdot 4\,H_2O$,[109,110] an intermediate involvement of hydrozincite in the formation process of the zinc phosphate seems reasonable. Concerning coordination numbers as depicted in panel **b** of Figure 3.12, a steady decrease of the coordination number of zinc to chlorine, and a likewise steady increase regarding oxygen was observed, in line with the transformation of $ZnCl_2$ into $Zn_3(PO_4)_2 \cdot 4\,H_2O$.

To provide a clear overview, the changes in the key parameters during the periods between the analyses of samples C, D, and E, i.e. in periods 5 min $\rightarrow$ 7 h and 7 h $\rightarrow$ 14 d, are presented in Table 3.2. In summary, immediately after addition of $ZnCl_2$ to artificial saliva, small nanoparticles are formed, which are contained in aggregates and are thought to be separated by a protein layer. Through the course of the reaction, the mean radii and distribution widths of these primary particles remain similar, while the particles are transformed to crystalline $Zn_3(PO_4)_2 \cdot 4\,H_2O$. Within the first seven hours, for which there is an indication of the presence of an intermediate, the aggregates become more densely packed. During the subsequent 14 days of storage the particle number density increases, accompanied by the disappearance of the intermediate and growth of aggregates in both size and the number of particles.

Table 3.2: SAXS-derived particle size distribution parameters for samples C, D and E, with observed increases ($\nearrow$), stagnations ($\rightarrow$), and decreases ($\searrow$)

Parameter	**Symbol**	**5 min $\rightarrow$ 7 h**	**7 h $\rightarrow$ 14 d**
Particle number density	N	$\rightarrow$	$\nearrow$
Mean radius (core)	R_{mean}	$\rightarrow$	$\rightarrow$
Distribution width	σ	$\rightarrow$	$\rightarrow$
Mean radius (core/shell)	r_0	$\searrow$	$\rightarrow$
Aggregate radius	ξ	$\rightarrow$	$\nearrow$
Radius of gyration	R_g	$\rightarrow$	$\nearrow$
Aggregation number	N_{agg}	$\rightarrow$	$\nearrow$
Crystalline intermediate		persists	disappears
$Zn_3(PO_4)_2 \cdot 4\,H_2O$		crystallises	persists

4 PUBLICATIONS

4.1 MICROWAVE-ASSISTED SYNTHESIS OF ULTRASMALL ZINC OXIDE NANOPARTICLES

Patrick E. J. Saloga and Andreas F. Thünemann
Langmuir **2019**, 35, 38, 12469-12482.

Figure 4.1: Graphical abstract.

Submitted on 26 June 2019, first published on 30 August 2019 in Langmuir.
An electronic version of the article is available.
DOI: 10.1021/acs.langmuir.9b01921

Reprinted with permission from *Langmuir* **2019**, 35, 38, 12469–12482.
Copyright 2019 American Chemical Society.

Author Contributions:
The general concept of this study was set up by me. I performed the nanoparticle syntheses and subsequent SAXS, DLS, UV-Vis and fluorescence spectroscopy data collection, procession as well as their evaluation. The evaluation of the WAXS data as well as discussion of the results and writing of the manuscript were carried out by Andreas F. Thünemann and me.

4.2 PHASE TRANSFER OF ULTRA-SMALL ZNO NANOPARTICLES TO AQUEOUS MEDIUM

Patrick E. J. Saloga, Tina Rybak, and Andreas F. Thünemann

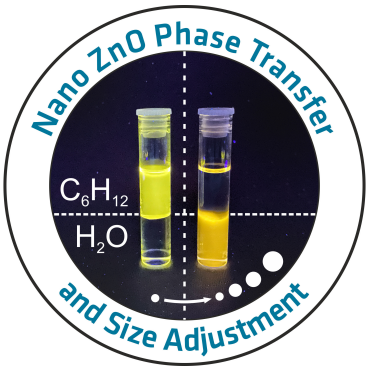

Figure 4.2: Graphical abstract.

Submitted on 28 October 2020 to ChemPhysChem.

Author Contributions:
The general concept of this study was set up by me. The syntheses and SAXS measurements were performed by Tina Rybak and me. The catalysis experiments, and the UV-Vis and fluorescence spectroscopy data collection were carried out by me. I performed the data analysis while the discussion of the results and writing of the manuscript were carried out by Andreas F. Thünemann and me with major contributions from my side.

Phase Transfer of Ultra-small ZnO Nanoparticles to Aqueous Medium

Patrick E. J. Saloga[1,2], Tina Rybak[1], and Andreas F. Thünemann[1,*]

[1]Bundesanstalt für Materialforschung und -prüfung (BAM), Unter den Eichen 87, 12205 Berlin, Germany

[2]Freie Universität Berlin, Fachbereich Biologie, Chemie, Pharmazie, Takustraße 3, 14195 Berlin, Germany

Abstract

This paper reports on a simple one-pot procedure to obtain aqueous ZnO nanoparticle dispersions from ZnO nanoparticles dispersed in cyclohexane. In the process, polyoxyethylene (20) sorbitan monooleate (polysorbate 80, Tween 80) functions as a phase transfer agent and colloidal stabilizer. Surprisingly, the particles grow in a defined manner during the transfer, presumably via coalescence. The final particle radii are tuneable in the range of $2.3 \pm 0.1\,\mathrm{nm}$ to $5.7 \pm 0.1\,\mathrm{nm}$ depending on the incubation time of the dispersions at $90\,^{\circ}\mathrm{C}$. Small-angle X-ray scattering is employed to determine the particle radius distributions before and after phase transfer. The larger ZnO particle radii are associated with a redshift of the optical bandgap and luminescence emission, as expected for semiconductor nanoparticles. The particles presented here exhibit a relative size distribution width of 20%, rendering them attractive for applications in, e.g., biology or catalysis. The latter application is demonstrated at the photocatalytic degradation of methylene blue dye.

1 Introduction

Zinc oxide (ZnO) nanoparticles with defined sizes are of scientific and industrial interest.[1] They are a robust alternative candidate to TiO_2 for cleaning of wastewater.[2, 3] Also, photocatalytically active pavings may alternatively be manufactured with ZnO instead of TiO_2, mainly for the degradation of NO_x compounds from combustion engines.[4] Nanoparticles are generally advantageous for catalytic applications, compared to microparticles, since the specific surface area scales reciprocally with particle size. We recently reported a microwave-assisted synthesis of ultra-small ZnO particles, which are stable long-term in cyclohexane.[5] However, depending on the photocatalysis requirements, these particles may need to be available as dispersions in water. Therefore, the present study aims to utilize the ZnO nanoparticles, from our previous study, as starting material and provide an easy method to transfer them from cyclohexane to water. The catalytic properties of the resulting aqueous ZnO dispersion has also been tested for the photocatalytic degradation of methylene blue as a typical model reaction for degradation of an organic pollutant.[6]

2 Results and Discussion

The preparation of water-dispersed zinc oxide nanoparticles, as presented here, utilizes spherical oleate-stabilized ZnO nanoparticles as starting material. These were prepared in a microwave-assisted synthesis, as previously reported.[5] Briefly, ZnO nanoparticles were synthesized within five minutes in a microwave at $125\,^{\circ}\mathrm{C}$ and obtained as a colloidally stable dispersion in cyclohexane. In the following, we refer to these particles as P_0. The phase transfer to aqueous solution started by the addition of polysorbate 80 (polyoxyethylene (20) sorbitan monooleate, trade name Tween 80) to P_0 yielding particles $\mathrm{P}_{0+\mathrm{TW}}$. Water was added next, followed by heating of the samples to $90\,^{\circ}\mathrm{C}$ for 240 minutes, whereby the cyclohexane was removed completely. This procedure yielded the aqueous ZnO particle dispersion H_{240}. Similarly, Ren et al. have shown that this method is applicable for the upconversion of oleate-stabilized $NaYF_4$:Yb,Er-nanoparticles.[7] Polysorbate 80 is a biocompatible nonionic surfactant, bearing an ethoxylated sorbitan and an oleate chain. The latter was expected to interact with the oleate-coating on the as-synthesized particles, with the hydrophilic groups enabling particle dispersion in water. Besides H_{240}, we were also interested in the intermediate stages of the phase transfer. Therefore, samples were additionally taken at heating times of 0, 15, 30, 60, and 90 minutes. The remaining cyclohexane in these samples was removed at reduced pressure at $40\,^{\circ}\mathrm{C}$, yielding samples H_0, H_{15}, H_{30}, H_{60} and H_{90}, respectively.

2.1 Particle Structure

All samples were analyzed with small-angle X-ray scattering (SAXS), and the resulting scattering curves are shown in Figure 1. It can be seen that the shape of the curves is characteristic of non-interacting nanoparticles. While SAXS is an accurate method for determining size distributions of particles smaller than 10 nm,[8] the particle shape needs to be known for a detailed SAXS data analysis. Scanning transmission electron microscopy was used for this purpose and confirmed the presence of spherical particles after phase transfer in sample H_{240}, with 90% of the particles in the size range of 5.5 and $8.5\,\mathrm{nm}$ (see Figure S1). As proven earlier, the particles P_0 are also spherical, but much smaller with radii in the range of 2 to $4\,\mathrm{nm}$.[5] Therefore we conclude that the particles grow during the phase transfer but keep their spherical shape. The simplest model for interpretation of the SAXS curves of P_0, $\mathrm{P}_{0+\mathrm{TW}}$, H_{15} H_{30}, H_{60}, H_{90} and H_{240} is a monomodal log-normal radial distribution of spherical ZnO particles. This simple model was not sufficient for the curve of H_0 for which a bimodal log-normal distribution was found suitable. The resulting curve fits are provided as solid lines in Figure 1.

As for nanoparticles with a ZnO core and a stabilizer shell, the question arises whether the determined radii distributions refer to the cores only or are inclusive of the particle shell. To answer this question, the scattering length densities of ZnO and polysorbate 80 need to be considered. More precisely, for copper K_α radiation with an energy of $8.04\,\mathrm{keV}$, the scattering length density difference between ZnO and water is $\Delta\mathrm{SLD} \simeq 3.31 \times 10^{11}\,\mathrm{cm}^{-2}$ and that of polysorbate 80 is $\Delta\mathrm{SLD} \simeq 4.39 \times 10^{9}\,\mathrm{cm}^{-2}$.[9] Therefore, ZnO scatters 75 times more than the stabilizer, and the scattering of the polysorbate can be neglected in SAXS analysis. In conclusion, it can be stated that SAXS detects the ZnO cores of the particles exclusively.

The mean radii of the zinc oxide particles before phase transfer in cyclohexane without (P_0) and with added polysorbate 80 ($\mathrm{P}_{0+\mathrm{TW}}$) both were $R_{\mathrm{mean}} = 2.3 \pm 0.1\,\mathrm{nm}$ and displayed a size distribution width of $\sigma = 0.3 \pm 0.1\,\mathrm{nm}$ (relative width of $\sigma_{\mathrm{rel}} = 13 \pm 1\%$). The particles exhibited a mean volume of $\langle V \rangle = 54 \pm 1\ \mathrm{nm}^3$ and contained a number of zinc oxide moieties of $n_{\mathrm{ZnO}} = 2250 \pm 40$ when assuming a density of $5.61\ \mathrm{g\ cm}^{-3}$. Upon stabilizer addition, no change in the size distribution parameters and thus no influence of the stabilizer on the ZnO cores was detected.

After complete phase transition, in sample H_{240}, values of $R_{\mathrm{mean}} = 5.7 \pm 0.1$ nm and $\sigma = 1.2 \pm 0.1$ nm

($\sigma_{\text{rel}} = 20\%$) were determined. This corresponds to $\langle V \rangle = 870 \pm 9\ \text{nm}^3$ and $n_{\text{ZnO}} = 36100 \pm 400$. While the mean volume of H_{240} is larger than that of P_0 by a factor of $n_{\text{p}} = 16$, the relative size distribution width increased only slightly. The value n_{p} could be interpreted as meaning that one H_{240} particle was formed from the material of 16 P_0 particles. To gain further insight into the growth mechanism, the particle properties of the intermediate steps of the phase transfer, as shown in Table 1, were examined in more detail. The two particle populations of H_0 displayed mean radii of $R_{\text{mean,1}} = 2.3 \pm 0.1\,\text{nm}$ and $R_{\text{mean,2}} = 7.2 \pm 0.1\,\text{nm}$. At later stages of the phase transfer the particle population was monomodal and R_{mean} increased with increasing incubation time in the line of $3.7\,\text{nm}$ (H_{15}), $4.3\,\text{nm}$ (H_{30}), $4.4\,\text{nm}$ (H_{60}), and $5.6\,\text{nm}$ (H_{90}) to the final value of $5.7\,\text{nm}$ (H_{240}). σ_{rel} was kept constant at 20% and therefore the σ values increased accordingly.

The observed ZnO particle growth could be explained along the interpretation scheme suggested by Caetano et al. for the formation of ZnO quantum dots.[10] Therein the initial steps of particle growth result from oriented attachment between several particles, with subsequent coalescence to larger particles. While the low solubility of ZnO in water could in principle enable Ostwald ripening, the aforementioned study showed that the particle growth occured mainly via aggregation and coalescence.[10] This model could explain the bimodality of the particle radii distribution found for H_0 in which single particles with $R_{\text{mean,1}}$ and agglomerated particles with $R_{\text{mean,2}}$ were present in parallel. Then, further coalescence would yield larger particles in samples H_{15}, H_{30} and H_{60}, with n_{P} values of 4 to 7, and then proceed to samples H_{90} and H_{240} with $n_{\text{P}} = 16$, respectively.

Dynamic light scattering (DLS) was employed to determine the hydrodynamic radii of the particles, which were in the range of about $4\,\text{nm}$ to $8\,\text{nm}$ but without apparent differences between the different particles. Very likely, the presence of the polymeric surfactant, which itself forms micelles with radii of around $R_{\text{h}} = 4\,\text{nm}$,[11] prevents a more precise determination of the hydrodynamic radii. Nevertheless, the hydrodynamic radii represent the total particle, including its stabilizing shell, and when comparing the hydrodynamic radii with the ZnO core radii from SAXS, all samples exhibited an approximately $2\,\text{nm}$ to $4\,\text{nm}$ thick stabilizer shell around the ZnO cores.

Table 1: Particle size evolution during phase transfer for primary particles P_0 and phase-transferred particles H_i, obtained after heating to $90\,^\circ\text{C}$ for i minutes: listed are mean particle radius R_{mean}, absolute (σ) and relative (σ_{rel}) size distribution widths from SAXS, average particle volume $\langle V \rangle$, the calculative number of primary particles contained therein, n_{P}, and the calculative number of formula units of ZnO within a particle, n_{ZnO}

Sample	R_{mean}	σ	σ_{rel}	$\langle V \rangle$	n_{P}	n_{ZnO}
	nm	nm	%	nm^3		
ZnO Nanoparticles before Phase Transfer in Cyclohexane						
P_0	2.3 ± 0.1	0.3 ± 0.1	13 ± 1	54 ± 1	1	2250 ± 40
P_{0+TW}	2.3 ± 0.1	0.3 ± 0.1	13 ± 1	54 ± 1	1	2250 ± 40
ZnO Nanoparticles after Phase Transfer in Water						
H_0	2.3^a	0.3^a	13	54	1	2250
	7.2 ± 0.1^a	1.5 ± 0.1^a	20	1770 ± 60	33 ± 2	74000 ± 3000
H_{15}	3.7 ± 0.1	0.8 ± 0.1	20	236 ± 5	4 ± 1	9800 ± 200
H_{30}	4.3 ± 0.1	0.9 ± 0.1	20	373 ± 10	7 ± 1	15500 ± 400
H_{60}	4.4 ± 0.1	0.9 ± 0.1	20	396 ± 9	7 ± 1	16400 ± 400
H_{90}	5.6 ± 0.1	1.2 ± 0.1	20	848 ± 20	16 ± 1	35200 ± 900
H_{240}	5.7 ± 0.1	1.2 ± 0.1	20	870 ± 9	16 ± 1	36100 ± 400

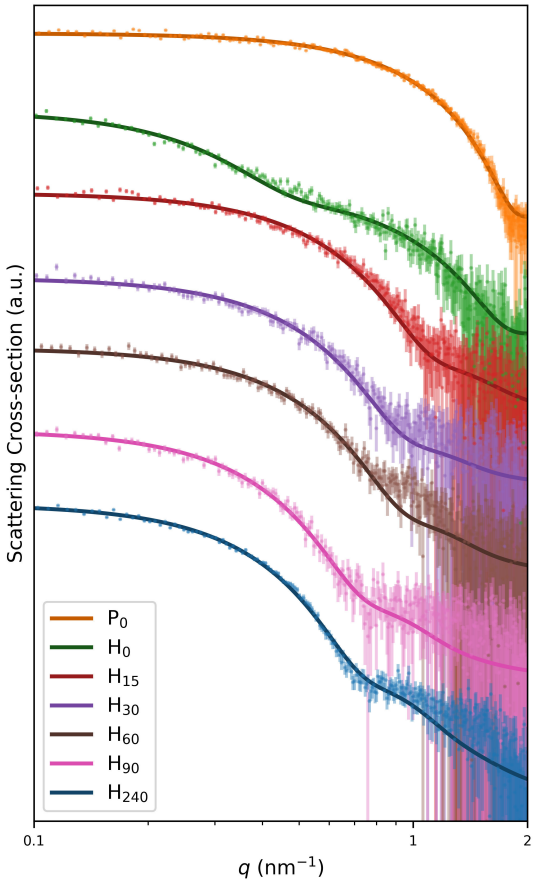

Figure 1: SAXS data (points with error bars) and curve fits (solid lines) of particles in cyclohexane (top curve, before transfer) and of aqueous particle dispersions obtained at the denoted heating times (lower curves, heating time increasing towards the bottom). Curves were shifted vertically for better visibility.

To clarify whether the phase transfer is driven solely by the evaporation of cyclohexane, whilst the particles would otherwise remain dispersed in the organic solvent, the synthesis was carried out as a microwave-assisted, autoclave-like process. Thus, all solvents remained in the system, and both dispersion media were available to the particles. After performing the incubation in the microwave for four hours, a two-phase system consisting of a turbid phase over an opalescent phase was obtained (see Figure S2 for a photograph). The volumes corresponded to those of the solvents used, although traces of the other respective solvent are likely present in both phases and cause the observed turbidity or opalescence. The mainly aqueous opalescent phase – with an odor characteristic of cyclohexane – was removed from the vessel for SAXS analysis (see Figure S2 for the data). Both before and after evaporation of the remaining cyclohexane, the scattering curve showed particles with the same radii as in the H_{240} particle system, but with a scattering intensity reduced by about 90%. During phase transfer in an open flask, about 50% of the water evaporates, though it remains in the system during microwave-assisted synthesis. The opalescence of the mainly aqueous phase could indicate the formation of a microemulsion in which the ZnO nanoparticles are locally dispersed in cyclohexane. An exclusively aqueous dispersion could then only be obtained by evaporation of the cyclohexane, whereby carrying out the phase transfer in an open vessel increases its efficiency by at least fivefold.

These results demonstrate that the described synthesis is suitable to obtain hydrophilic ZnO nanopar-

ticles in an aqueous dispersion with tuneable particle size on the lower nanoscale. The observed growth process may be explained by coalescence, whereby up to $n_P = 16 \pm 1$ primary particles fuse during the heating phase to form the obtained larger particles.

2.2 Optical Properties

With increasing size of semiconductor nanoparticles such as ZnO at the lower nanoscale, a complementary change in the optical properties is expected, as described earlier for the apolar ZnO particles used here.[5] Figure 2 shows UV-Vis and fluorescence spectra of the particles P_0 and H_{240}, i.e., before and after phase transfer, illustrating the redshift in both absorption edges and mean fluorescence energies. The former were determined employing Tauc plots, yielding band gap energies of 3.44 ± 0.01 eV and 3.31 ± 0.01 eV for particles before and after phase transfer, respectively. The fluorescence spectra were approximated with Gaussian distributions, resulting in mean fluorescence energies of 2.20 ± 0.01 eV and 2.08 ± 0.01 eV with comparable full widths at half maximum of 0.63 ± 0.01 eV and 0.62 ± 0.01 eV, respectively. The exact cause of the optical properties of nanoscale zinc oxide, and thus its dependence on, e.g., stabilising agents and the solvent, is still disputed, hence the analysis here is restricted to the determination of the respective energies.[12] The UV-vis and fluorescence data support our interpretation from SAXS that the particles were grown in a defined way during the phase transfer.

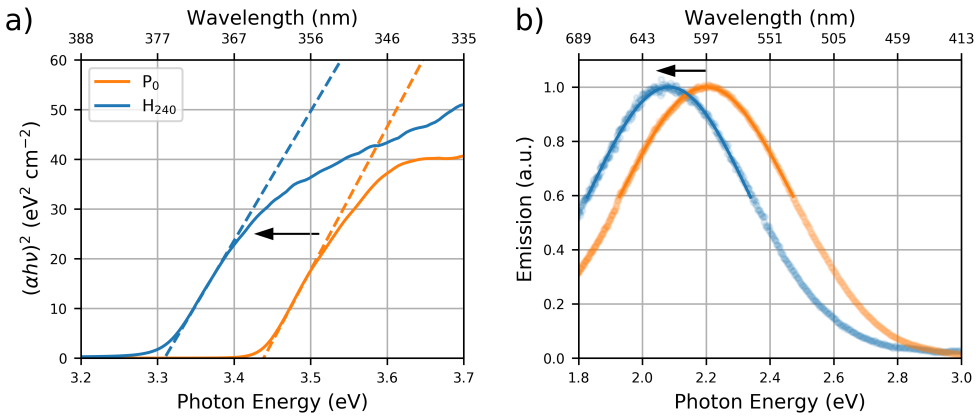

Figure 2: Normalised UV-Vis and Fluorescence spectra of ZnO nanoparticles before (P_0) and after phase transfer (H_{240}). a) Tauc plot depicting the absorption edges (solid lines) and linear fits (dashed lines) for determination of the band gap energies. b) Fluorescence data (symbols) and Gaussian fits (solid lines) for determination of the mean fluorescence energy.

2.3 Catalysis

A potential field of application for aqueous ZnO nanoparticle dispersions arises in photocatalysis. We have chosen methylene blue as a model substance to test whether the particles H_{240} can photocatalytically decompose organic pollutants. Methylene blue has been frequently used to evaluate the photocatalytic activity of nanoparticles,[6, 13, 14] where the decomposition of the dye can be easily monitored with UV-Vis spectroscopy. We added H_{240} particles to a solution of methylene blue and irradiated the solution with UV light with a wavelength of 365 nm. Over time, the solution discolored in the presence of H_{240}, while the color did not change substantially when no particles were added. This indicates that the H_{240} particles are photocatalytically active. Therefore, time-dependent UV-Vis spectra were measured to quantify the

catalytic activity. A typical time series of the spectra is shown in panel a) of Figure 3. Two distinct absorbance bands are visible in the spectra with maxima at photon energies of $E = 1.8\,\mathrm{eV}$ and $2.1\,\mathrm{eV}$, respectively, corresponding to wavelengths of $\lambda = 689\,\mathrm{nm}$ and $590\,\mathrm{nm}$. For interpretation we fitted each spectrum with the sum of two Gaussian functions f_1 and f_2 and a background contribution f_3. An example is depicted in panel b) of Figure 3, which corresponds to a reaction time of $t = 0$, i.e., directly after adding H_{240} to the solution of methylene blue. It can be seen there that the measured spectrum (silver circles) is sufficiently well reproduced by the sum $f = f_1 + f_2 + f_3$ (blue, solid line). The individual contributions to the spectrum f_1, f_2 and f_3 are given for comparison (orange dashed line, green dash-dotted line, and red dotted line, respectively). The f_3 was modelled analogously to a scattering intensity I as a function of two constants a and b and the photon energy E as $I = a + b \cdot E^4$. Examples of the curves and curve fits are given in Figure S4 for times of 0 s and 1780 s after the start of the irradiation of the sample. Furthermore, the amplitudes A_1 and A_2 of f_1 and f_2 (left figure, second row), and the sum of both amplitudes ΣA (right figure, second row) are depicted. In the third row, plots of the time-dependent evolution of mean μ_1 and μ_2, and widths σ_1 and σ_2 of f_1 and f_2, are given, respectively. The last rows shows the concentration of methylene blue c_{MB} as a function of the irradiation time, and the decrease in $\ln c/c_0$ with a linear fit, alongside its slope and intercept. The liner fit is interpreted in terms of a pseudo first order reaction kinetics expressed by

$$\ln \frac{c}{c_0} = -k_{\mathrm{app}} \cdot t. \tag{1}$$

Values for the apparent rate constants are $k_{\mathrm{app}} = (0.222 \pm 0.010) \times 10^{-3}\,\mathrm{s}^{-1}$ for H_{240} and $k_{\mathrm{app}}(0.026 \pm 0.001) \times 10^{-3}\,\mathrm{s}^{-1}$ for pure water (Figure S5). This means that the decomposition of the methylene blue dye is increased by a factor of 8.5 in the presence of H_{240} in comparison to water as a control medium. Balcha et al. synthesised zinc oxide nanoparticles for photocatalysis.[15] They reported a maximum of $k_{\mathrm{app}} = 12.4 \times 10^{-3}\,\mathrm{min}^{-1}$, which is equivalent to $0.207 \times 10^{-3}\,\mathrm{s}^{-1}$, for a sol-gel prepared catalyst at a concentration of $250\,\mathrm{mg\,L}^{-1}$. This value is close to that of H_{240}, where the catalyst concentration is much lower at $20\,\mathrm{mg\,L}^{-1}$. After normalization of these values to the mass concentration of the particles, one could therefore assume that H_{240} has a much higher photocatalytic activity than the particles studied by Balcha et al.[15] Such a finding might be plausible due to the smaller size of H_{240} compared to the sol-gel synthesized particles, which have crystallite sizes of about 30 nm. However, caution is required in this interpretation.

Kisch and Bahnemann have laid out that the comparison of photocatalysts from different studies is intrinsically difficult.[16] One reason for this unsatisfactory situation is the difficulty to quantify the quantum yield correctly. Especially with semiconductor dispersions, a substantial part of the absorbance may be due to reflection and scattering and not absorption. Another issue arises from the use of polychromatic light sources, which complicates the determination of an apparent quantum yield. Further, the optical properties can differ substantially between different photoreactors, catalyst concentrations, and the reactions studied. To circumvent all these problems, to estimate the catalytic activity of H_{240}, we investigate commercially available ZnO and TiO_2 catalysts in the same conditions as H_{240}. In addition, a solution of a mixture of sodium oleate and polysorbate 80 was investigated to evaluate the influence of the stabilizer. All three samples were found catalytically active, and the data was evaluated in the same way as H_{240}, as shown in Figures S6, S7, and S8. An overview of the decrease in the concentration of methylene blue is given in Figure 4. Curve fits according to eq. (1) are given as straight lines and the k_{app}-values are shown in panels a) and b) of Figure 4, respectively. It can be seen that the commercially ZnO particles display the highest value of $k_{\mathrm{app}} = (0.436 \pm 0.019) \times 10^{-3}\mathrm{s}^{-1}$, closely followed by TiO_2 with $k_{\mathrm{app}} = (0.412 \pm 0.020) \times 10^{-3}\mathrm{s}^{-1}$. Noteworthy is that the stabiliser has a significant catalytic activity

even without the presence of nanoparticles with $k_{app} = (0.104 \pm 0.004) \times 10^{-3} s^{-1}$.

Since the zinc oxide nanoparticles of H_{240} are significantly smaller than those of the commercial zinc oxide particles, we expected that H_{240} also has a higher catalytic activity than the commercial ones. Nonetheless, this is not the case, and the observed, comparatively lower catalytic activity could be due to the stabilizer molecules on the particle surface. It is likely that polysorbate 80 renders the surface less accessible for methylene blue as compared to the commercial samples without stabilizer. The particle concentration of H_{240} of $c_{NP} = 0.44 \pm 0.03\,g\,L^{-1}$ and the volume-weighted surface area $VSSA_{NP} = (39 \pm 2) \times 10^3\ m^2/m^3$ were determined from the SAXS data. After dilution in the methylene blue dye solution for investigation of the catalytic properties, the sample contained nanoparticles at a concentration of $21 \pm 1\,mg\,L^{-1}$ and a surface area of $VSSA_{NP} = (3.9 \pm 0.2) \times 10^{-3}\ m^2$. The commercial comparison particles were then used at the same mass concentration, and the particle surface area available in each case was calculated based on the particle size specified by the manufacturer. The determined values for k_{app} with nanoparticle concentration- and surface area-normalised values k_{app}/c_{NP} and $k_{app}/VSSA_{NP}$ are listed in Table 2. The surface normalised rate constants of $(58 \pm 1) \times 10^{-3} s^{-1} m^{-2}$ (H_{240}), $(232 \pm 16) \times 10^{-3} s^{-1} m^{-2}$ (commercial ZnO) and $(165 \pm 11) \times 10^{-3} s^{-1} m^{-2}$ quantify the differences of the catalytic activity.

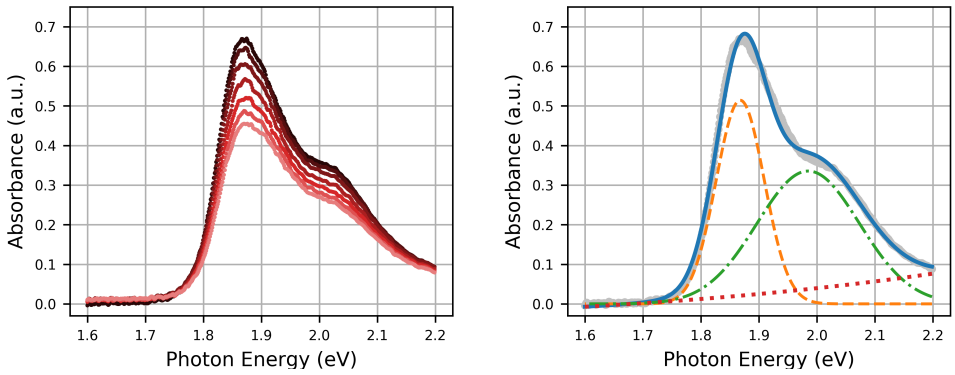

Figure 3: UV-Vis analysis of the photocatalytic degradation of methylene blue employing H_{240} particles as catalyst. a) UV-Vis spectra taken in 300 s intervals, depicting the decrease of absorbance of the dye over time, and b) UV-Vis spectrum at a reaction time of 0 s (silver circles) and curve fit (blue, solid line) with the sum of of two Gaussian functions f_1 and f_2 and a Rayleigh scattering contribution f_3 (orange dashed line, green dash-dotted line and red dotted line, respectively).

3 Conclusions

Hydrophobic oleate-coated ZnO nanoparticles with a mean radius of $R_{mean} = 2.3 \pm 0.1\,nm$ were prepared by an established microwave-assisted synthesis and obtained in cyclohexane.[5] To transfer these ultra-small nanoparticles to an aqueous medium, they were coated with polysorbate 80, and the organic solvent was removed after the addition of water under low pressure. To obtain aggregate-free particle systems, an intermediate heating process to 90 °C was needed, the duration of which determined the final particle size. Thus, hydrophilic ZnO nanoparticles with sizes between $R_{mean} = 3.7 \pm 0.1\,nm$ and $R_{mean} = 5.7 \pm 0.1\,nm$ in aqueous dispersion were obtained. These particles could be utilized in photocatalysis, which was demonstrated by the degradation of methylene blue.

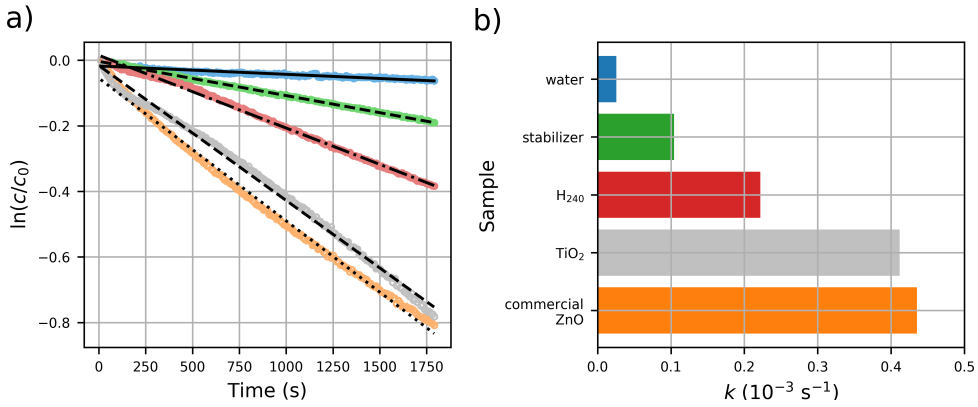

Figure 4: a) Plot of $\ln c/c_0$ of methylene blue dye as a function of irradiation time with UV-light for pure water (blue), stabilizer (green), H_{240} (red), commercial ZnO (orange) and TiO_2 (silver), given in the order of increasing steepness of the decrease. Straight lines are linear fits for evaluation of the rate constants. b) Rate constants derived from the slopes of the curve fits in a).

Table 2: Parameters obtained from catalysis experiments on different samples: applied concentration of nanoparticles c_{NP}, resultant volume-weighted specific surface area $VSSA_{NP}$, determined apparent rate constant k_{app}, and normalised rate constants k_{app}/c_{NP} and $k_{app}/VSSA_{NP}$

Sample	c_{NP}	$VSSA_{NP}$	k_{app}	k_{app}/c_{NP}	$k_{app}/VSSA_{NP}$
	$mg\,L^{-1}$	$10^{-3}\,m^2$	$10^{-3}\,s^{-1}$	$10^{-3}\,L\,g^{-1}s^{-1}$	$10^{-3}\,s^{-1}m^{-2}$
This Synthesis					
ZnO particles (H_{240})	21 ± 1	3.9 ± 0.2	0.222 ± 0.010	11 ± 1	58 ± 4
Sodium oleate and polysorbate 80	–	–	0.104 ± 0.004	–	–
Blank (H_2O)	–	–	0.026 ± 0.001	–	–
Commercial Particles					
25 nm ZnO	21 ± 1	1.9	0.436 ± 0.019	21 ± 2	232 ± 16
25 nm TiO_2	21 ± 1	2.5	0.412 ± 0.020	20 ± 2	165 ± 11

4 Experimental

4.1 Materials

All chemicals were used as received without further purification. Sodium oleate (95%) was purchased from abcr, zinc(II) chloride and Polysorbate 80 from Merck, and tetrabutylammonium hydroxide (1 M in methanol) from Sigma-Aldrich. Cyclohexane, ethanol, and tetrahydrofuran were purchased from Th. Geyer. Ultrapure water (*Milli-Q*, $18.2\,M\Omega \cdot cm$ at 25 °C) was used.

4.2 Nanoparticle Synthesis

Hydrophobic, oleate-coated zinc oxide nanoparticles were obtained as described previously.[5] Briefly, 166 mg (264 µmol) zinc oleate was dissolved in 4.736 mL tetrahydrofuran, and after addition of 264 µL of 1 M tetrabutylammonium hydroxide in methanol, the microwave-assisted synthesis of particles was carried out at 125 °C for 5 min. Particle purification was carried out by two times precipitation in a fourfold excess of ethanol and subsequent dispersion in cyclohexane.

4.3 Phase Transfer

A volume of $3.5\,\mathrm{mL}$ particle dispersion ($1.8 \pm 0.1\,\mathrm{gL^{-1}}$ ZnO in cyclohexane) was used for the phase transfer of the particles from cyclohexane to water. An amount of $50\,\mu\mathrm{L}$ Polysorbate 80 ($53\,\mathrm{mg}$, $40\,\mu\mathrm{mol}$) was added to the dispersion and stirred for ten minutes. Then, $10\,\mathrm{mL}$ of water was added and stirred for another ten minutes at a temperature of $21\,^{\circ}\mathrm{C}$. Afterwards, the temperature was set to $90\,^{\circ}\mathrm{C}$ for time intervals of 0, 15, 30 60 90 and $240\,\mathrm{min}$. The cyclohexane was completely removed after a heating time of $240\,\mathrm{min}$ as indicated by the absence of its characteristic smell. A rotary evaporator was employed to remove remaining cyclohexane from the samples obtained at shorter heating times at a pressure of $100\,\mathrm{mbar}$ and a temperature of $40\,^{\circ}\mathrm{C}$. The obtained aqueous particle dispersions were centrifuged for $20\,\mathrm{min}$ ($\mathrm{H_{15}}$: $90\,\mathrm{min}$) at $12\,000\,g$ to remove any aggregates.

4.4 Catalysis Experiment

The catalytic performance of the phase-transferred particles was analysed by the photocatalytic degradation of methylene blue (MB) as a 10^{-5} M solution in water. An aqueous solution containing 1 vol% Polysorbate 80 and $22.4\,\mathrm{gL^{-1}}$ sodium oleate was prepared as a reference sample. Samples used were an aqueous solutions containing $21\,\mathrm{gL^{-1}}$ particles, the reference sample, or water. $100\,\mu\mathrm{L}$ of the sample solutions were added to $2\,\mathrm{mL}$ of the MB solution contained in a $10\,\mathrm{mm} \times 10\,\mathrm{mm}$ High Precision Quartz Cell from Hellma Analytics under stirring. The samples were irradiated using a Herolab UV-4 S/L hand lamp at an indicated wavelength of $365\,\mathrm{nm}$ and UV-Vis spectra were recorded using a StellarNet Inc. BLACK-Comet C-50 Spectrometer with an SL5 Deuterium+Halogen Light Source and a DP400 dip probe ($10\,\mathrm{mm}$ optical path length) attached. A sketch of the experimental set-up can be found in the supporting information (Figure S3). For the photocatalysis experiment, particles were added to a solution of methylene blue dye, so that the final catalyst concentration was $21 \pm 1\,\mathrm{mg \cdot L^{-1}}$. This sample was placed in a quartz cuvette and, under UV irradiation with a wavelength of $365\,\mathrm{nm}$, the change in MB absorbance was monitored in $10\,\mathrm{s}$ intervals for a duration of $30\,\mathrm{min}$. A sketch of the experimental set-up can be found in Figure S3 in the supporting information, and based on the geometries of the UV lamp and the cuvette, the photon flux hitting the sample was estimated at around $1.9 \times 10^{15}\ \mathrm{s^{-1}}$.

4.5 SAXS Measurements

Small-angle X-ray scattering (SAXS) measurements were performed in a polycarbonate flow-through capillary at $21 \pm 1\,^{\circ}\mathrm{C}$ with a SAXSess instrument (Anton Paar, Austria), attached to a laboratory X-ray generator (PW3830, PANalytical) and operated with a fine focus glass X-ray tube at a voltage of $40\,\mathrm{kV}$ and a current of $40\,\mathrm{mA}$ (Cu-K_α, λ = $0.1542\,\mathrm{nm}$). Focusing multilayer optics and a block collimator provide a monochromatic primary beam with low background noise. SASfit version 0.94.11 was used for curve fitting, and the determination of the particle size distribution[9].

4.6 DLS Measurements

Dynamic light scattering (DLS) measurements were performed using a multiangle ALV 7004 device with a He-Ne-Laser ($\lambda = 632.8\,\mathrm{nm}$) from ALV Langen. The samples were used as obtained from the phase transfer procedure without dilution or filtration. Data evaluation was performed according to the ISO standard 13321:1996 and with the CONTIN program by Provencher to obtain the hydrodynamic radii R_h.[17]

4.7 UV-Vis measurements

UV-Vis measurements were performed using a StellarNet Inc. BLACK-Comet C-50 Spectrometer with an SL5 Deuterium+Halogen Light Source. Aqueous dispersions were used as prepared, whilst dispersions in cyclohexane were diluted in a ratio of 1:20, and then filled into a $10\,\mathrm{mm} \times 10\,\mathrm{mm}$ High Precision Quartz Cell from Hellma Analytics. A tauc plot was used to determine the optical absorption edges.

4.8 Fluorescence measurements

Fluorescence measurements were carried out on a HORIBA Fluorolog-3 spectrofluorimeter. The particle systems were prepared in the same way as for the UV-Vis measurements. Excitation wavelengths $10\,\mathrm{nm}$ smaller than the absorption edges, as determined by UV-Vis measurements, were chosen, and Gaussian approximations were employed to determine the mean fluorescence energy.

Acknowledgement

The authors thank Frederik Firschke for experimental assistance, V.-D. Hodoroaba and S. Benemann for the electron microscopy image, Thomas Risse for valuable discussions, and Glen J. Smales for proofreading the manuscript.

References

[1] A. Kolodziejczak-Radzimska, T. Jesionowski, *Materials* **2014**, *7*, 2833–2881.

[2] S. G. Kumar, K. Rao, *RSC Adv.* **2015**, *5*, 3306–3351.

[3] Y. Kumar, S. Tayyab, S. Muzammil, *Arch. Biochem. Biophys.* **2004**, *426*, 3–10.

[4] B. O. Bica, J. V. S. de Melo, *Constr Build Mater.* **2020**, *252*, 12.

[5] P. E. J. Saloga, A. F. Thünemann, *Langmuir* **2019**, *35*, 12469–12482.

[6] A. Houas, *Appl. Catal. B Environ.* **2001**, *31*, 145–157.

[7] W. Ren, G. Tian, S. Jian, Z. Gu, L. Zhou, L. Yan, S. Jin, W. Yin, Y. Zhao, *RSC Adv.* **2012**, *2*, 7037.

[8] B. R. Pauw, C. Kästner, A. F. Thünemann, *J. Appl. Crystallogr.* **2017**, *50*, 1280–1288.

[9] I. Breßler, J. Kohlbrecher, A. F. Thünemann, *J. Appl. Crystallogr.* **2015**, *48*, 1587–1598.

[10] B. L. Caetano, V. Briois, S. H. Pulcinelli, F. Meneau, C. V. Santilli, *J. Phys. Chem. C* **2017**, *121*, 886–895.

[11] A. Amani, P. York, H. de Waard, J. Anwar, *Soft Matter* **2011**, *7*, 2900.

[12] A. Janotti, C. G. Van de Walle, *Rep. Prog. Phys.* **2009**, *72*, 126501.

[13] R. Asahi, *Science* **2001**, *293*, 269–271.

[14] A. Mishra, A. Panigrahi, P. Mal, S. Penta, G. Padmaja, G. Bera, P. Das, P. Rambabu, G. R. Turpu, *J. Alloys Compd.* **2020**, *842*, 155746.

[15] A. Balcha, O. P. Yadav, T. Dey, *Environ. Sci. Pollut. Res.* **2016**, *23*, 25485–25493.

[16] H. Kisch, D. Bahnemann, *J. Phys. Chem. Lett.* **2015**, *6*, 1907–1910.

[17] S. W. Provencher, *Comput. Phys. Commun.* **1982**, *27*, 229–242.

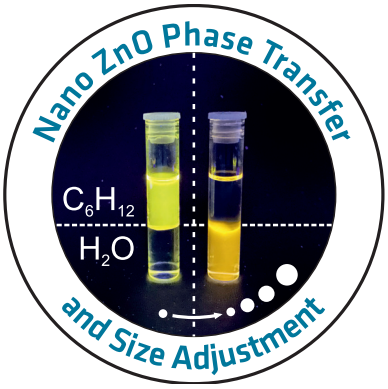

Figure 5: Table of contents graphic

Supporting Information for Phase Transfer of Ultra-small ZnO Nanoparticles to Aqueous Medium

Patrick E. J. Saloga[1,2], Tina Rybak[1], and Andreas F. Thünemann[1,*]

[1]Bundesanstalt für Materialforschung und -prüfung (BAM), Unter den Eichen 87, 12205 Berlin, Germany

[2]Freie Universität Berlin, Fachbereich Biologie, Chemie, Pharmazie, Takustraße 3, 14195 Berlin, Germany

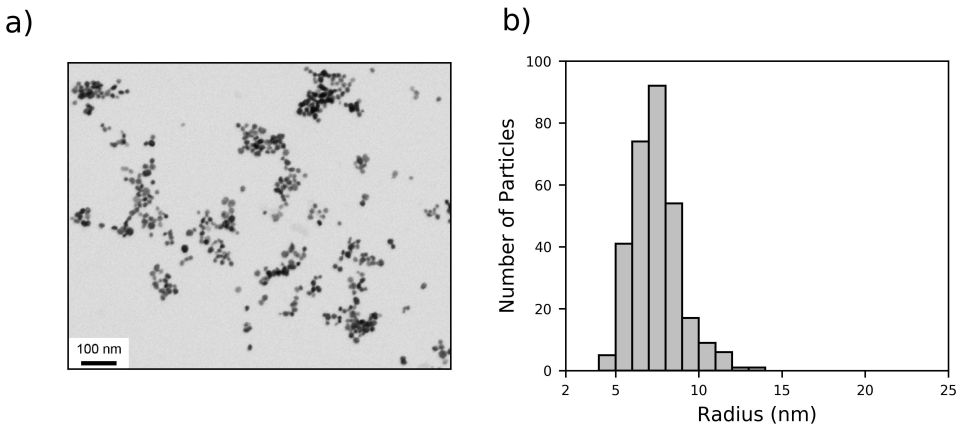

Figure S1: a) Scanning Transmission Electron Microscopy (STEM) image of the H_{240} ZnO nanoparticles. b) Estimate of the corresponding particle radii distribution.

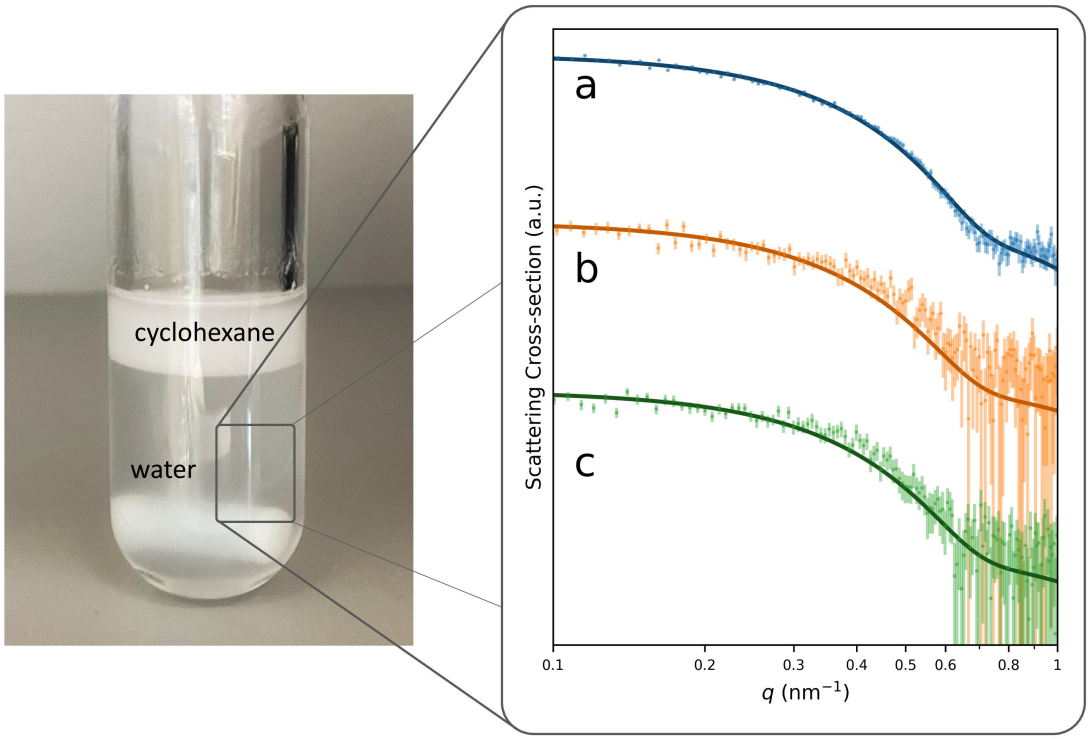

Figure S2: Photograph of a microwave vessel containing a water-rich and cyclohexane-rich phase after incubation of $P_{0,\mathrm{TW}}$ in a microwave at a temperature of $90\,^{\circ}\mathrm{C}$ for 240 min. The right-hand figure displays SAXS data and corresponding curve fits of particles after different phase transfer processes. Data in **a** are from H_{240}. Data in **b** are from the aqueous phase in the microwave vessel shown in the left-hand picture and data in **c** are from the particles in the same phase after evaporation of the cyclohexane. Data were shifted vertically for better visibility. The curve fits (solid lines in **a**, **b** and **c**) correspond to the same radii of $R_{\mathrm{mean}} = 5.7 \pm 0.1$ nm and size distribution width $\sigma_{\mathrm{rel}} = 20\%$, within the experimental uncertainties.

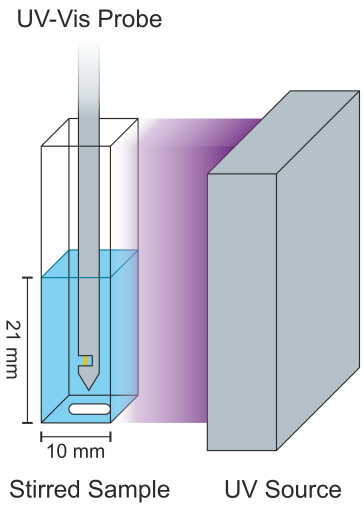

Figure S3: Scheme depicting the experimental set-up for analysis of the photocatalytic decomposition of methylene blue. Therein the sample consisting of an aqueous solution of methylene blue and H_{240} particles is located in a standard quartz cuvette. While stirring, the sample is irradiated with UV-light from the right, with a wavelength of $\lambda = 365$nm. UV-Vis spectra are recorded with a probe immersed directly into the sample.

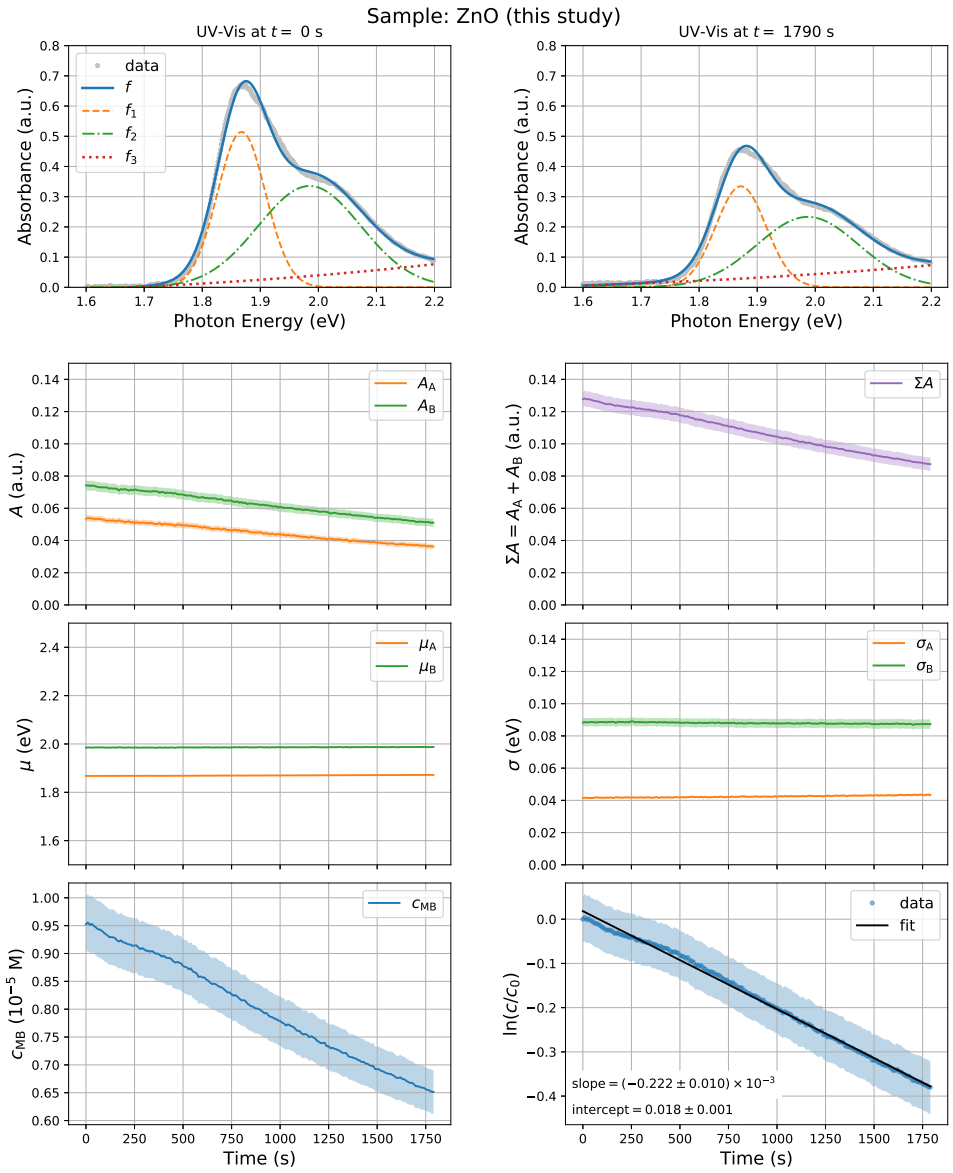

Figure S4: Evaluation of the UV-Vis data from the catalysis experiment with H_{240} nanoparticles (ZnO particles synthesized in this study). The upper row displays UV-Vis spectra measured at times of 0 s and 1780 s after the start of irradiation of the sample (silver circles). Curve fits utilising f (blue solid line) consist of the sum of two Gaussian functions f_1 and f_2 (orange, dashed line, and green, dash-dotted line, respectively), as well as a background contribution f_3 (red, dotted line). Second row: Amplitudes A_1 and A_2 of Gaussian functions f_1 and f_2 (left). Sum of both amplitudes ΣA (right). Third row: Time-dependent evolution of mean μ_1 and μ_2, and widths σ_1 and σ_2 of f_1 and f_2, respectively. Last row: Concentration of methylene blue c_{MB}, and the decrease in $\ln c/c_0$ with linear fit and determined slope and intercept.

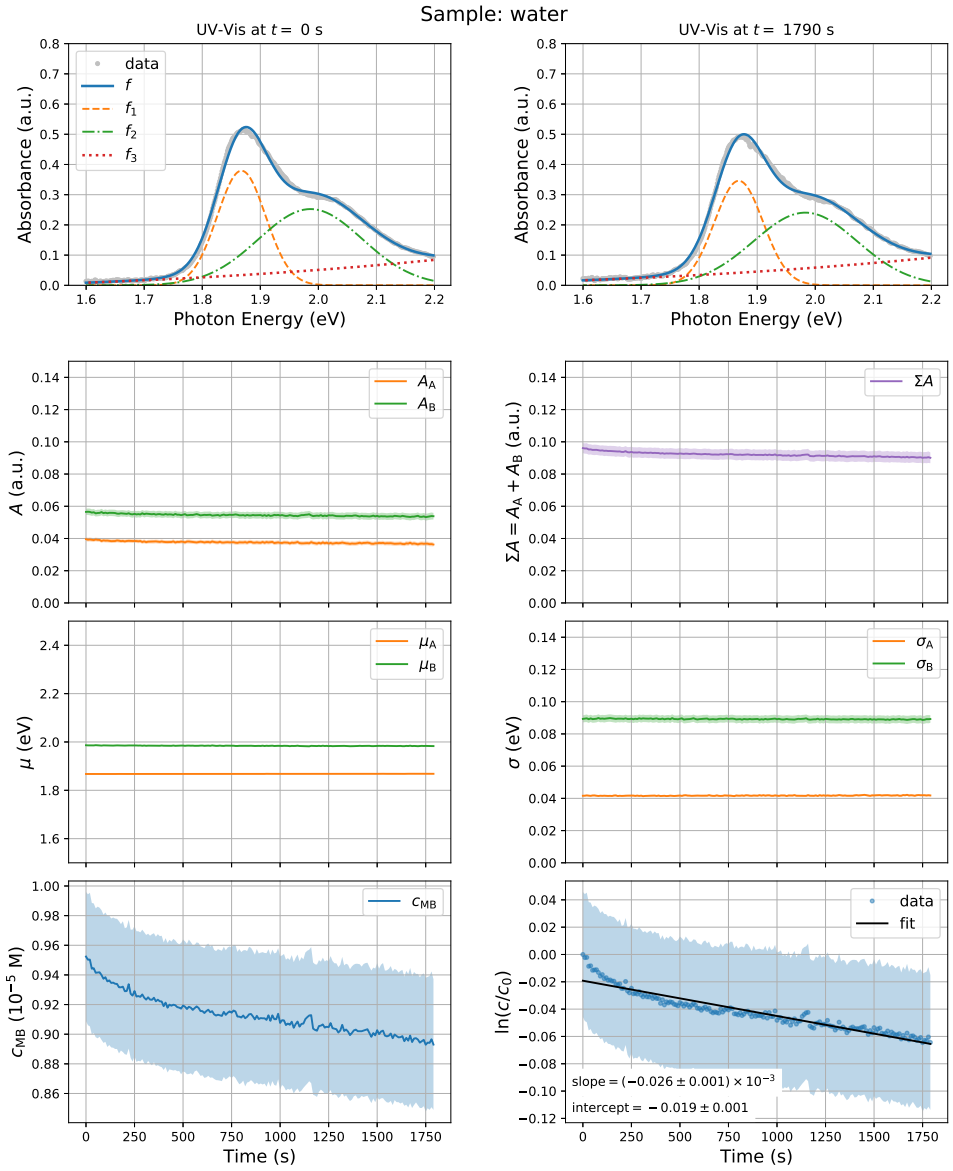

Figure S5: Evaluation of the UV-Vis data from the blank catalysis experiment with only methylene blue in water. The upper row displays UV-Vis spectra measured at times of 0 s and 1780 s after the start of irradiation of the sample (silver circles). Curve fits utilising f (blue solid line) consist of the sum of two Gaussian functions f_1 and f_2 (orange, dashed line, and green, dash-dotted line, respectively), as well as a background contribution f_3 (red, dotted line). Second row: Amplitudes A_1 and A_2 of Gaussian functions f_1 and f_2 (left). Sum of both amplitudes ΣA (right). Third row: Time-dependent evolution of mean μ_1 and μ_2, and widths σ_1 and σ_2 of f_1 and f_2, respectively. Last row: Concentration of methylene blue c_{MB}, and the decrease in $\ln c/c_0$ with linear fit and determined slope and intercept.

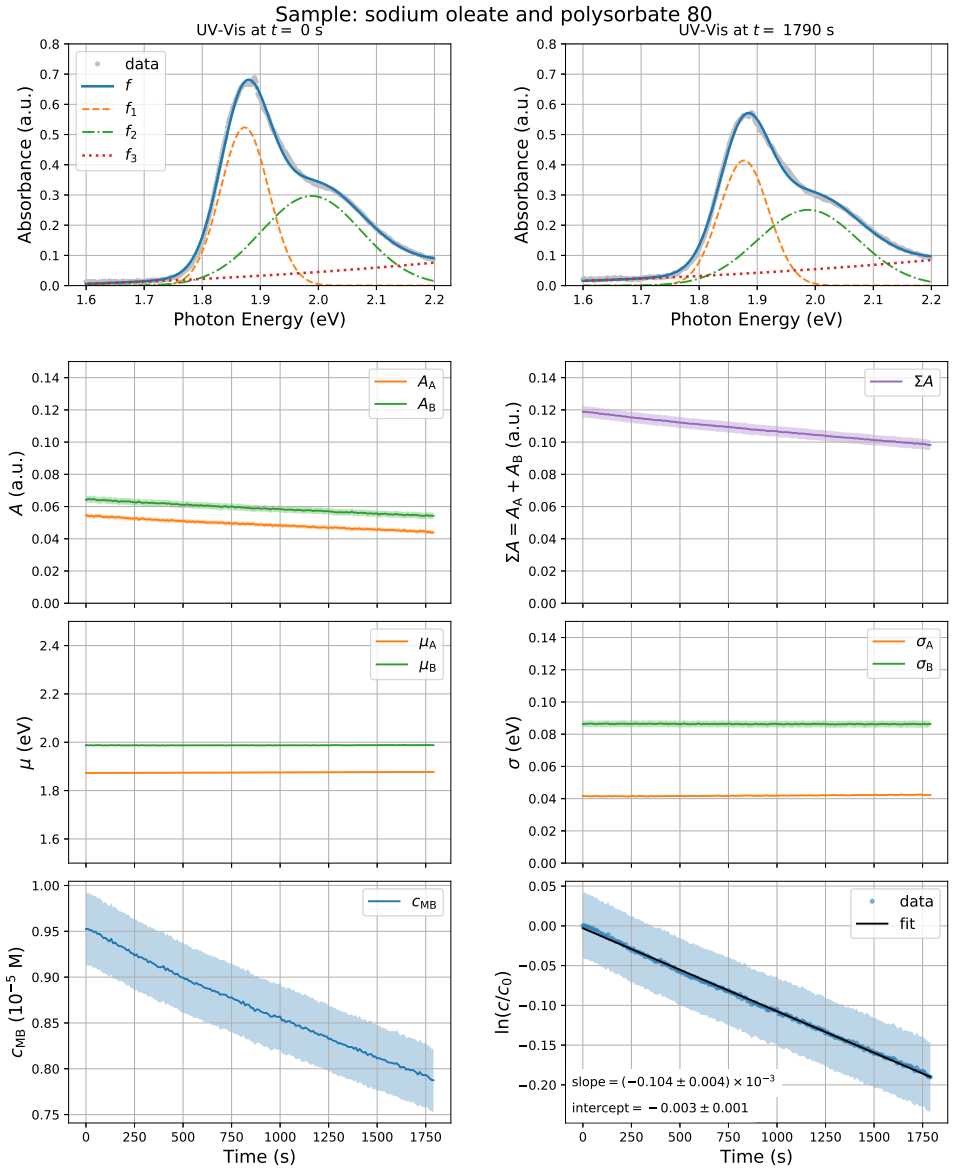

Figure S6: Evaluation of the UV-Vis data from the catalysis experiment containing the colloidal stabilizer (mixture of sodium oleate and polysorbate 80 in water). The upper row displays UV-Vis spectra measured at times of 0 s and 1780 s after the start of irradiation of the sample (silver circles). Curve fits utilising f (blue solid line) consist of the sum of two Gaussian functions f_1 and f_2 (orange, dashed line, and green, dash-dotted line, respectively), as well as a background contribution f_3 (red, dotted line). Second row: Amplitudes A_1 and A_2 of Gaussian functions f_1 and f_2 (left). Sum of both amplitudes ΣA (right). Third row: Time-dependent evolution of mean μ_1 and μ_2, and widths σ_1 and σ_2 of f_1 and f_2, respectively. Last row: Concentration of methylene blue c_{MB}, and the decrease in $\ln c/c_0$ with linear fit and determined slope and intercept.

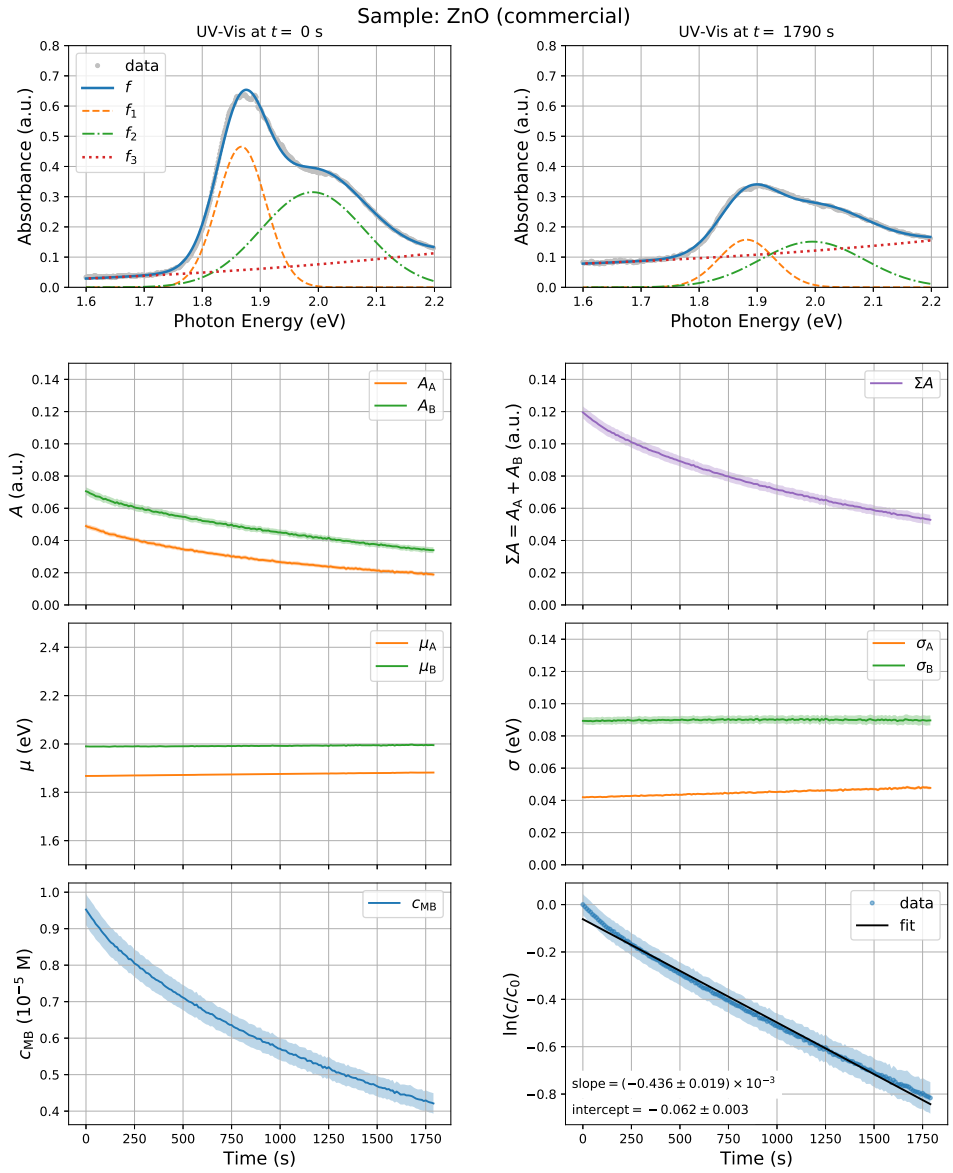

Figure S7: Evaluation of the UV-Vis data from the catalysis experiment with commercial ZnO nanoparticles. The upper row displays UV-Vis spectra measured at times of 0 s and 1780 s after the start of irradiation of the sample (silver circles). Curve fits utilising f (blue solid line) consist of the sum of two Gaussian functions f_1 and f_2 (orange, dashed line, and green, dash-dotted line, respectively), as well as a background contribution f_3 (red, dotted line). Second row: Amplitudes A_1 and A_2 of Gaussian functions f_1 and f_2 (left). Sum of both amplitudes ΣA (right). Third row: Time-dependent evolution of mean μ_1 and μ_2, and widths σ_1 and σ_2 of f_1 and f_2, respectively. Last row: Concentration of methylene blue c_{MB}, and the decrease in $\ln c/c_0$ with linear fit and determined slope and intercept.

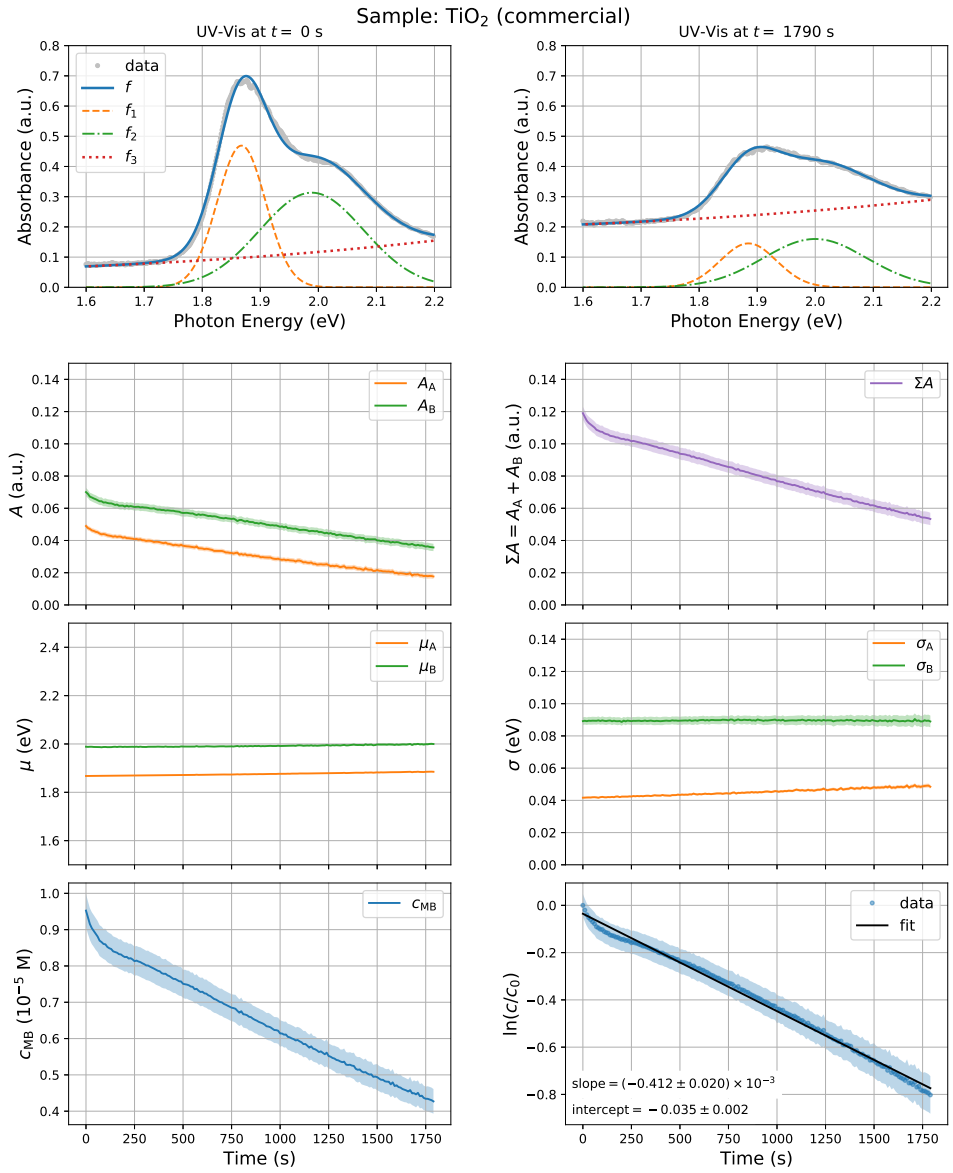

Figure S8: Evaluation of the UV-Vis data from the catalysis experiment with commercial TiO_2 nanoparticles. The upper row displays UV-Vis spectra measured at times of 0 s and 1780 s after the start of irradiation of the sample (silver circles). Curve fits utilising f (blue solid line) consist of the sum of two Gaussian functions f_1 and f_2 (orange, dashed line, and green, dash-dotted line, respectively), as well as a background contribution f_3 (red, dotted line). Second row: Amplitudes A_1 and A_2 of Gaussian functions f_1 and f_2 (left). Sum of both amplitudes ΣA (right). Third row: Time-dependent evolution of mean μ_1 and μ_2, and widths σ_1 and σ_2 of f_1 and f_2, respectively. Last row: Concentration of methylene blue c_{MB}, and the decrease in $\ln c/c_0$ with linear fit and determined slope and intercept.

4.3 ENVIRONMENTAL IMPACT OF ZNO NANOPARTICLES EVALUATED BY IN VITRO SIMULATED DIGESTION

Linn Voss, Patrick E. J. Saloga, Valerie Stock, Linda Böhmert, Albert Braeuning, Andreas F. Thünemann, Alfonso Lampen, and Holger Sieg
ACS Appl. Nano Mater. **2020**, 3, 1, 724-733.

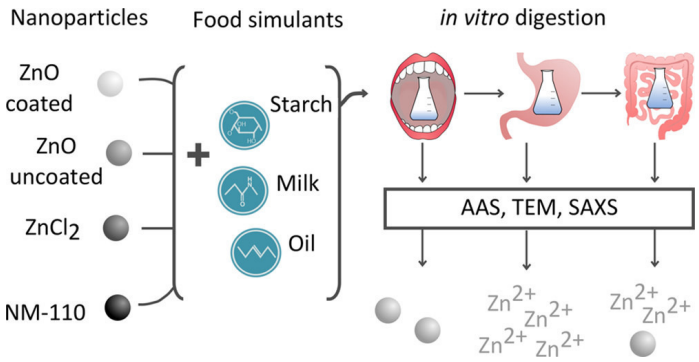

Figure 4.3: Graphical abstract.

Submitted on 13 November 2019, first published on 20 December 2019 in ACS Applied Nano Materials.
An electronic version of the article is available.
DOI: 10.1021/acsanm.9b02236

Reprinted with permission from *ACS Appl. Nano Mater.* **2020**, 3, 1, 724-733. Copyright 2020 American Chemical Society.

Author Contributions:
The general concept of this study was set up by Linn Voss, Holger Sieg, Albert Braeuning, Linda Böhmert, Valerie Stock, and Alfonso Lampen. I have contributed to the preparation and conduct of six self-contained artificial digestive processes. I conducted the SAXS data collection, procession, and evaluation and discussed the results with Andreas F. Thünemann, with whom the corresponding contributions to the manuscript were written. All other data shown in the publication were obtained by Linn Voss, who created the first draft of the manuscript together with Holger Sieg.

This article has been corrected in: *ACS Appl. Nano Mater.* **2020**, 3, 5, 4914. These corrections do not affect the results, discussion, or conclusions of the study. An electronic version of the correction is available.
DOI: 10.1021/acsanm.0c01054

Reprinted with permission from *ACS Appl. Nano Mater.* **2020**, 3, 5, 4914. Copyright 2020 American Chemical Society.

4.4 ZINC PHOSPHATE NANOPARTICLES PRODUCED IN SALIVA

Patrick E. J. Saloga, Glen J. Smales, Adam H. Clark, and Andreas F. Thünemann
Eur. J. Inorg. Chem. **2020**, 2020, 38, 3654-3661.

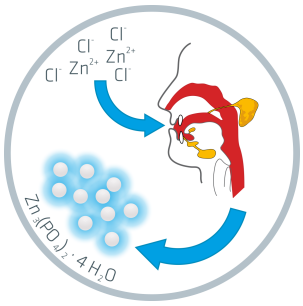

Figure 4.4: Graphical abstract.

Submitted on 28 May 2020, first published on 1 July 2020 in European Journal of Inorganic Chemistry.
An electronic version of the article is available.
DOI: 10.1002/ejic.202000521

Author Contributions: The general concept of this study was set up by me. SAXS and WAXS data were obtained by Glen J. Smales and evaluated by me. Infrared spectroscopy data were collected and evaluated by me. *In situ* XAS data was collected by me with help of Glen J. Smales and Adam H. Clark. *Ex situ* XAS data was collected by Adam H. Clark, who evaluated all XAS data. All authors discussed the results and contributed to the writing of the manuscript, with major contributions from my side.

EurJIC
European Journal of Inorganic Chemistry

Full Paper
doi.org/10.1002/ejic.202000521

Chemistry Europe
European Chemical Societies Publishing

Biomineralization

Zinc Phosphate Nanoparticles Produced in Saliva

Patrick E. J. Saloga,[a,b] Glen J. Smales,[a] Adam H. Clark,[c] and Andreas F. Thünemann*[a]

Abstract: This paper reports the formation of zinc phosphate nanoparticles from the artificial digestion of zinc chloride. Initially, the formation of amorphous primary particles with a mean radius of 1.1 nm is observed, alongside the formation of larger, protein stabilized aggregates. These aggregates, with a radius of gyration of 37 nm, are observed after 5 minutes of exposure to artificial saliva and are shown to be colloidally stable for a minimum time of two weeks. The initially formed primary particles are thought to consist of amorphous zinc phosphate, which is then transformed into crystalline $Zn_3(PO_4)_2{\cdot}4H_2O$ over the course of two weeks. Our results demonstrate that the interaction of inorganic salts with bodily fluids can induce the formation of de novo nanoparticles, which in turn, provides insights into how zinc-enriched foods may also facilitate the formation of nanoparticles upon contact with saliva. As such, this may be considered as an undesirable (bio)mineralization.

Introduction

Zinc salts are commonly added to food and cosmetic products to promote health and well-being, as zinc is an essential trace element required by the hundreds of different enzymes within the human body.[1] The recommended daily zinc intake is 8–11 mg,[2] and levels of zinc within the body are maintained predominantly through absorption and excretion within the gastrointestinal tract.[3] Zinc salts, instead of elemental zinc, are added to products intended for human use/consumption, such as cereals and mouthwash, often in the form of compounds such as zinc acetate, zinc chloride, zinc gluconate and zinc glutamate.[4] However, the use of zinc-enriched products can lead to the intake of excessive amounts of zinc (> 40 mg/day), which can induce adverse effects, such as dysfunctions of the gastrointestinal tract, or a reduced copper status.[2] The achievement of daily intake levels > 300 mg with zinc-enriched, over-the-counter products has been reported to be potential causes of anaemia and leukopenia.[5]

For these reasons, cosmetic products within the European Union, are only permitted to contain water-soluble zinc salts up to concentrations of 1 % to protect human health within the Single Market.[4] Recently, Voss et al.[31] evaluated the environmental impact of ZnO nanoparticles by in vitro simulated digestion.

In this study, zinc chloride ($ZnCl_2$) at a mass fraction of ≈ 0.13 % in saliva, is utilized to study the effects that can occur upon its addition to saliva, and more precisely, evaluate whether the formation of nano-scale structures occurs. This is particularly relevant from a toxicological point of view where the chemical transformation, or the de novo formation of nanostructures with different toxicological properties to those of the originally ingested material, can take place.[6]

Results

Formation of Nanoparticles

An aqueous solution of zinc chloride (sample A) was added to a solution of artificial saliva (sample B), which abides by the German standard DIN 19378.[7] As per the NANOGENOTOX protocol for producing suitable, manufactured nanomaterial exposure media, the artificial saliva contained the protein bovine serum albumin (BSA).[8]

The samples were examined after the addition of the zinc salt to artificial saliva at time intervals of five minutes (sample C), seven hours (sample D), and after a period of storage of two weeks (sample E).

For the investigation of the samples in a size range of approximately 0.3 - 300 nm, small-angle X-ray scattering (SAXS) was utilized as a method of choice, in combination with wide-angle X-ray scattering (WAXS) to detect changes in crystalline structures. Sample B was used as background, for which the SAXS data of samples C, D, and E was corrected (see Figure S1, Supporting Information).

We found that the intensity of the SAXS signal increases rapidly upon the addition of $ZnCl_2$ to artificial saliva, and upon investigation of sample C, the scattering curve exhibits features

[a] P. E. J. Saloga, Dr. G. J. Smales, Dr. A. F. Thünemann
Bundesanstalt für Materialforschung und -prüfung (BAM),
Unter den Eichen 87, 12205 Berlin, Germany
E-mail: andreas.thuenemann@bam.de
[b] P. E. J. Saloga
Freie Universität Berlin, Fachbereich Biologie, Chemie, Pharmazie,
Takustraße 3, 14195 Berlin, Germany
[c] Dr. A. H. Clark
Paul Scherrer Institut,
Forschungsstrasse 111, 5232 Villigen PSI, Switzerland
Supporting information and ORCID(s) from the author(s) for this article are available on the WWW under https://doi.org/10.1002/ejic.202000521.
© 2020 The Authors. Published by Wiley-VCH Verlag GmbH & Co. KGaA. • This is an open access article under the terms of the Creative Commons Attribution License, which permits use, distribution and reproduction in any medium, provided the original work is properly cited.

 © 2020 The Authors. Published by Wiley-VCH Verlag GmbH & Co. KGaA, Weinheim

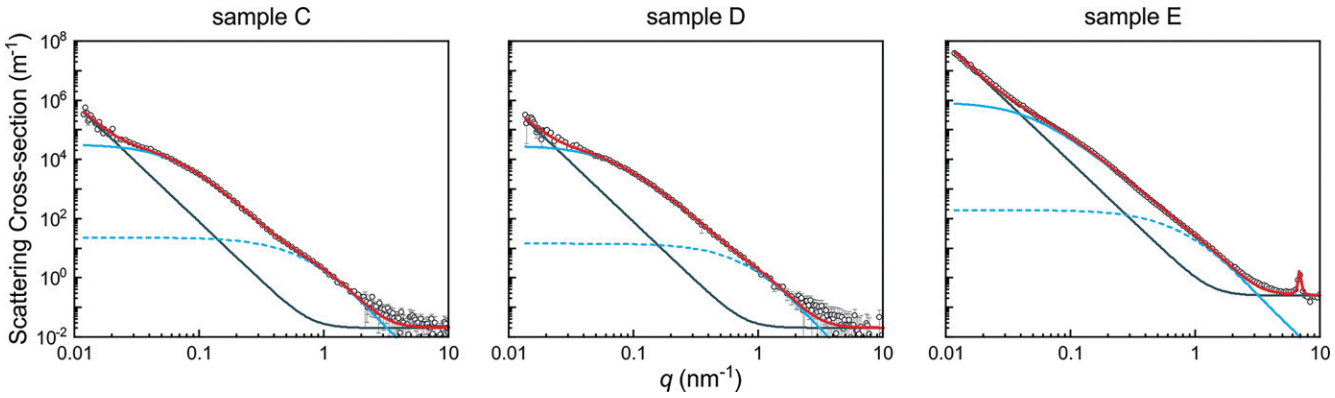

Figure 1. SAXS data of samples C, D, and E (symbols). The model curves (red, solid lines) are the sum of the scattering contribution from the particles according to Equation (1) (blue, solid lines) and a background according to Equation (2) (gray lines). The particle scattering is the product of the form factor of log-normally distributed spheres according to Equation (3) (blue dashed lines) and the mass fractal structure factor according to Equation (7). The structure factors are depicted in Figure S2 (Supporting Information).

typically expected from the presence of nano-scale structures (see Figure 1).

The SAXS pattern can be described well by the presence of two populations of nanostructures from the bumps observed in the data at q-values of ca. 0.1 and 1 nm^{-1}. Due to this, the scattering curves are modelled as the sum of a contribution from small primary particles that form aggregates (mass fractal agglomerates),[9,10] alongside a contribution from larger particles with radii of several hundred nanometers, due to the SAXS patterns' tendency towards a slope of q^{-4} at low q-values.

Briefly, the scattering intensity $I(q)$ as a function of the scattering vector q is the product of the particle form factor $P(q)$ and the structure factor $S(q)$, and it is complemented by a background function according to Equations (1) and (2).

$$I(q) = P(q)S(q) + I_{\mathrm{bkg}}(q) \tag{1}$$

$$I_{\mathrm{bkg}}(q) = a + bq^{-4} \tag{2}$$

$I_{\mathrm{bkg}}(q)$ was introduced to compensate for structures larger than ca. 300 nm in radius, whose scattering signal – as a first approximation – was expected to drop off with q^{-4} in the q-range under investigation.

The form factor of a log-normal size distribution of spherical particles is composed of said size distribution $f(N, R, R_{\mathrm{median}}, \sigma_{\log})$ and the scattering from a single sphere $I_s(\Delta\eta, q, R)$ in Equation (3) as:

$$P(q) = \int_0^\infty f\left(N, R, R_{\mathrm{median}}, \sigma_{\log}\right) I_s(\Delta\eta, q, R)\, \mathrm{d}R. \tag{3}$$

Here, N is the particle number density, R the sphere radius, R_{median} the median sphere radius, $\sigma_{\log}$ the width parameter of the size distribution, and $\Delta\eta$ the scattering length density difference between the particles and the surrounding medium. The log-normal size distribution is defined as Equation (4):

$$f(N, R, R_{\mathrm{median}}, \sigma_{\log}) = \frac{N}{R\sigma_{\log}\sqrt{2\pi}} \exp\left[-\frac{(\ln R - \ln R_{\mathrm{median}})^2}{2\sigma_{\log}^2}\right] \tag{4}$$

and the scattering of a single sphere as Equation (5):

$$I_s(\Delta\eta, q, R) = \left[\frac{4}{3}\pi R^3 \Delta\eta \frac{3(\sin qR - qR\cos qR)}{(qR)^3}\right]^2. \tag{5}$$

$P(q)$ is depicted in Figure 1 as the blue, dashed line and corresponds to the scattering of non-interacting particles, i.e. $S(q) = 1$. The corresponding number density of particles N and the size distribution parameters R_{median}, and $\sigma_{\log}$ can be found in Table S1 (Supporting Information). From these values, the mean radius R_{mean} and the width σ of the size distribution were calculated in Equation (6):

$$R_{\mathrm{mean}} = R_{\mathrm{median}} e^{\frac{\sigma_{\log}^2}{2}} \text{ and } \sigma = R_{\mathrm{mean}} \left(e^{2\sigma_{\log}^2} - e^{\sigma_{\log}^2}\right)^{\frac{1}{2}}. \tag{6}$$

To include particle–particle interactions such as the formation of agglomerates, a q-dependent structure factor needs to be introduced. Equation (7) depicts the structure factor of said mass fractal, with the fractal dimension D, the mean radius of the individual particles r_0, the distance from the fractal center r, and the fractal correlation cut-off ξ. In general, r_0 can be interpreted as the particle radius including any stabilizing shell separating the individual particles, and ξ as the fractal aggregate radius.[9,10] The structure factors as a function of the scattering vector are depicted in Figure S2 (Supporting Information).

$$S(q) = 1 + \frac{D}{r_0^D} \int_0^\infty r^{D-1} \exp\left[-\frac{r}{\xi}\right] \frac{\sin qr}{qr}\, \mathrm{d}r. \tag{7}$$

The integral in $S(q)$ can be solved analytically according to Equation (8):

$$S(q) = 1 + \frac{D\Gamma(D-1)}{(qr_0)^D} \frac{\sin[(D-1)\arctan q\xi]}{[1+(q\xi)^{-2}]^{(D-1)/2}}. \tag{8}$$

Multiplication of the structure factor with the form factor as in Equation (1) yields the scattering intensity $I(q)$ of an aggregate consisting of log-normally distributed spherical particles, and is depicted in Figure 1 as the blue, solid line. That way, the parameters of the mass fractal r_0, ξ, and D were obtained.

Furthermore, the radius of gyration R_g and the aggregation number N_{agg} were determined in Equation (9) as:

© 2020 The Authors. Published by Wiley-VCH Verlag GmbH & Co. KGaA, Weinheim

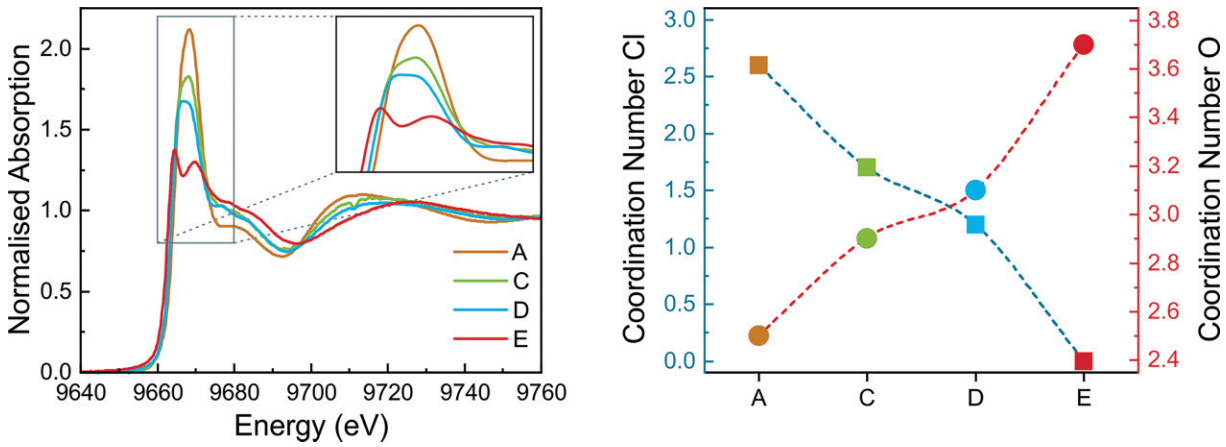

Figure 2. X-ray absorption fine structure (XAFS) spectra measured at the Zn *K*-edge of samples A, C, D, and E (left, solid lines), and coordination numbers of zinc (right) with regard to chlorine (squares, left axis of ordinate) and oxygen (circles, right axis of ordinate) as determined from fitting to the EXAFS region.

$$R_g = \xi\left[\frac{1}{2}D(D+1)\right]^{\frac{1}{2}} \text{ and } N_{agg} = \left(\frac{R_g}{r_0}\right)^D. \quad (9)$$

The particle size distribution parameters obtained from the aforementioned theory can be found in Table S1 (Supporting Information).

X-ray Absorption Spectroscopy

X-ray absorption spectroscopy (XAS) measurements were carried out to investigate the local structural environment of zinc within the reaction medium. The X-ray absorption fine structure (XAFS) of the zinc-containing samples (A, C, D, and E) at the Zn *K*-edge (9660 eV) is shown in Figure 2 (left), with the refined Zn–Cl and Zn–O coordination numbers (right) obtained from fitting of the extended X-ray absorption fine structure (EXAFS). The X-ray absorption near edge structure (XANES) is shown with an enlarged inset focusing on the top of the edge (left). EXAFS fitting was performed with k^2 weighting between 2.1 and 10.3 Å^{-1} to refine the local geometric structure. The quality of the EXAFS fitting is shown in Figure S3 (Supporting Information) for both R- and *k*-spaces, demonstrating a close agreement between the model and the data for all samples. The bond length of Zn–O and Zn–Cl refined to be approximately 1.94 Å and 2.36 Å which are in line with the structure of ZnO and $ZnCl_2$ respectively.

Compound Identification

Infrared spectroscopy (IR) and wide-angle X-ray scattering (WAXS) were employed to determine the chemical composition of the nanostructures formed in the digestive process. Since after combining aqueous solutions of $ZnCl_2$ and the respective component of saliva (see Table 1), formation of a precipitate was only evident in the cases of KH_2PO_4 and $NaHCO_3$, these samples were selected for comparison with sample C ($ZnCl_2$ in saliva). IR spectra were recorded and are depicted in Figure 3, and WAXS data is displayed in Figure 4, alongside reference data for $CaSO_4{\cdot}2H_2O$ and $Zn_3(PO_4)_2{\cdot}4H_2O$, taken from ICSD Collection Codes 161622[11] and 1945.[12]

Table 1. Composition of artificial saliva.

Compound	Supplier	Amount [mg]
α-Amylase	Sigma-Aldrich	41.9
$CaCl_2{\cdot}2H_2O$	NeoLab	25.0
KCl	NeoLab	75.0
KH_2PO_4	AppliChem	100.0
Mucin	Sigma-Aldrich	125.3
NaCl	NeoLab	83.4
$NaHCO_3$	NeoLab	25.0
NaSCN	Carl Roth	25.0
$Na_2SO_4{\cdot}10H_2O$	AppliChem	207.9
Urea	AppliChem	1.7
Uric acid	AppliChem	16.7

Discussion

To elucidate whether the addition of an aqueous solution of $ZnCl_2$ to artificial saliva could induce the formation of nanostructures, a corresponding solution was characterized by means of SAXS, XAFS, WAXS, and IR at three time points throughout the digestion procedure. In total, the following five samples were obtained and examined: 6.8 % $ZnCl_2$ in H_2O before the addition to saliva (sample A), artificial saliva without zinc (sample B), and 0.13 % $ZnCl_2$ in saliva after five minutes (sample C), seven hours (sample D), and after a storage period of two weeks (sample E). SAXS curves were obtained from samples B, C, D, and E, with sample B acting as a background correction for the other three samples. XAFS measurements were performed on the zinc-containing samples A, C, D, and E, whilst WAXS measurements were performed on all samples. The identification of the products formed was complemented by IR measurements of sample C.

It may also be desirable to additionally characterize the samples with imaging techniques, such as SEM and TEM, however, saliva does not conform well to such methods due to its high content of salts and proteins.

© 2020 The Authors. Published by Wiley-VCH Verlag GmbH & Co. KGaA, Weinheim

Full Paper
doi.org/10.1002/ejic.202000521

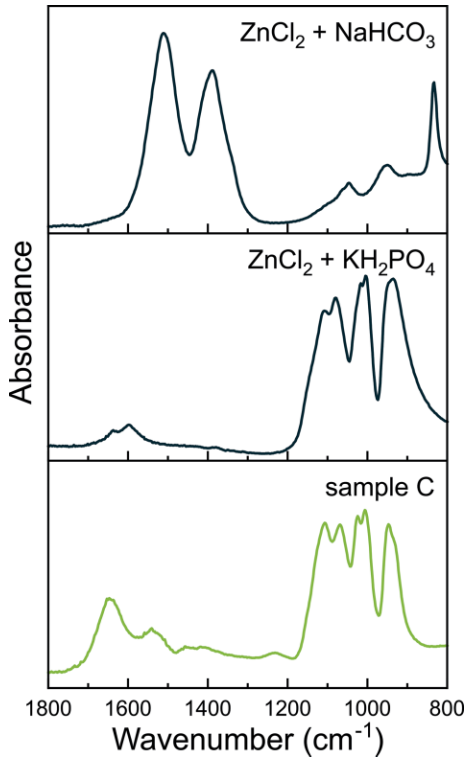

Figure 3. Infrared absorbance spectra of the precipitate formed from $ZnCl_2$ in aqueous solutions of $NaHCO_3$ (top), KH_2PO_4 (middle), and in saliva (bottom). The top spectrum shows absorption bands characteristic of the carbonate ion (antisymmetric stretching modes at $\tilde{\nu}$ = 1513 cm^{-1} and 1388 cm^{-1}, symmetric stretching mode at $\tilde{\nu}$ = 1054 cm^{-1}, and bending modes at $\tilde{\nu}$ = 953 cm^{-1} and 832 cm^{-1}). The two remaining spectra show absorption bands associated with the phosphate ion (symmetric and antisymmetric stretching modes between $\tilde{\nu}$ = 800 cm^{-1} and 1200 cm^{-1}) and water of hydration (bending modes around $\tilde{\nu}$ = 1600 cm^{-1}).

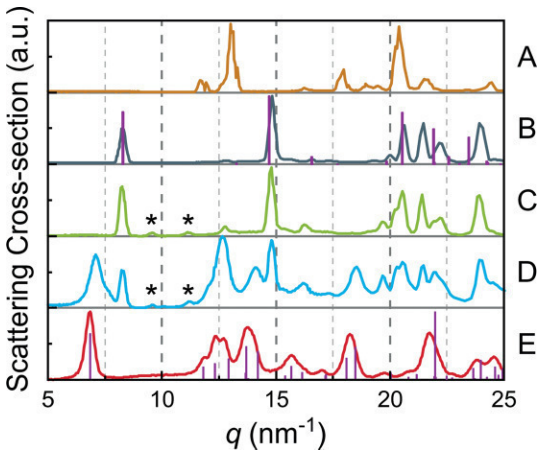

Figure 4. Wide-angle X-ray scattering data of samples A–E (solid lines) and reference data for $CaSO_4 \cdot 2H_2O$ (bars at sample B) and $Zn_3(PO_4)_2 \cdot 4H_2O$ (bars at sample E), taken from ICSD Collection Codes 161622[11] and 1945,[12] respectively.

From SAXS measurements, the formation of nanoparticles was observed within five minutes of incubation in artificial saliva. Small primary particles, exhibiting a mean radius of R_{mean} = 1.1 ± 0.2 nm and a distribution width of σ = 0.7 ± 0.2 nm, were found to aggregate, alongside structures larger than the maximum visible range of the data (ca. 300 nm in radius) in samples C, D, and E. From fits of the SAXS data, it can be seen that the resulting parameters describing the primary particles remained unchanged, within their relative uncertainties, throughout the experiments (samples C, D and E). This gives a good indication that the primary particles are present from the beginning, with their size distribution not changing significantly over the remaining period. Hence, only changes in the chemical composition and interaction with the environment are thought to be possible.

Within the scope of identifying the chemical composition of the formed particles, infrared spectroscopy measurements revealed similarities between the precipitates formed from $ZnCl_2$ with KH_2PO_4 and in saliva whilst the sample formed in the presence of $NaHCO_3$ is substantially different (Figure 3). More specifically, the latter displayed strong absorption bands at $\tilde{\nu}$ = 1513 cm^{-1} and 1388 cm^{-1}, which are associated with the antisymmetric stretching modes of the carbonate ion.[13] Bands stemming from the symmetric stretching mode (1054 cm^{-1}) and the bending modes (953 cm^{-1} and 832 cm^{-1}) are also observed. Hales and Frost performed infrared spectroscopy studies on smithsonite ($ZnCO_3$) and hydrozincite [$Zn_5(CO_3)_2(OH)_6$]. They attributed the occurrence of the otherwise IR-inactive symmetric stretching mode and of several antisymmetric stretching modes in hydrozincite to the reduced symmetry as compared to smithsonite.

The other two samples, on the other hand, show several bands in the 800 cm^{-1} – 1200 cm^{-1}-region that are typical for the phosphate ion and assigned to symmetric and antisymmetric stretching modes.[14] The broader, less pronounced bands around 1600 cm^{-1} are thought to originate from bending modes of water of hydration. Therefore, it was assumed that a hydrated zinc phosphate forms upon the addition of $ZnCl_2$ to saliva and wide-angle X-ray scattering (WAXS) measurements of the dried samples A–E were carried out (Figure 4).

As a reference, the scattering pattern of $ZnCl_2$ was collected (sample A), however this characteristic signal is not found in the subsequent samples, indicating that the compound has undergone a chemical transformation. Upon centrifugation and drying of the artificial saliva (sample B), scattering peaks of $CaSO_4 \cdot 2H_2O$ became visible at q = 8.28 nm^{-1}, 14.84 nm^{-1}, 16.55 nm^{-1}, and in the region of q > 20 nm^{-1}. These peaks remained visible in subsequent samples C and D. $CaSO_4 \cdot 2H_2O$ is thought to have formed due to the presence of $CaCl_2 \cdot 2H_2O$ and $Na_2SO_4 \cdot 10H_2O$ in saliva, and has been identified by comparison to a reference pattern (bars at sample B, ICSD collection code 161622).[11] The signal from $CaSO_4 \cdot 2H_2O$ is seen to dominate the pattern obtained from sample C, suggesting that shortly after the injection of the $ZnCl_2$ solution, no considerable amounts of other crystalline material were formed. However, small, broad diffraction peaks at q = 9.56 nm^{-1} and 11.16 nm^{-1} were observed in both sample C and D (asterisks), but not in the final product (sample E). This may indicate the formation of an intermediate, thought to be hydrozincite [$Zn_5(CO_3)_2(OH)_6$], which exhibits diffraction peaks at similar positions (ICSD collection code 16583).[15] Shifts in the X-ray absorption near edge

© 2020 The Authors. Published by Wiley-VCH Verlag GmbH & Co. KGaA, Weinheim

Full Paper
doi.org/10.1002/ejic.202000521

fine structure (XANES) region of the X-ray absorption spectra (XAS) data support this assumption, as discussed later in more detail. Seven hours after the $ZnCl_2$ injection, besides scattering peaks of $CaCl_2{\cdot}2H_2O$, those of the final product $Zn_3(PO_4)_2{\cdot}4H_2O$ became visible in the WAXS pattern of the dried sample D, although slightly shifted to higher *q*-values. For instance, the (020) scattering peak appeared at q = 7.11 nm^{-1} and was observed to be broadened in comparison to that seen in sample E at q = 6.83 nm^{-1}. In comparison to the SAXS curves of the liquid samples D and E, it can be seen that the said scattering peak is only visible in sample E, with the diffraction signal most likely being masked by the scattering of water in sample D.

Scattering of $Zn_3(PO_4)_2{\cdot}4H_2O$ was not observed in sample C, and non-crystalline intermediates during the formation of zinc phosphate have been reported in the literature. For instance, Roming et al. reported on the presence of non-crystalline zinc phosphate structures in nanoparticles obtained from a polyol-mediated synthesis.[16] Despite the application of a whole series of analytical methods, such as solid state P-NMR, they were unable to elucidate the structure exactly. However, the presence of a low-molecular organic compound (diethylene glycol) in the structure are thought to be responsible for the observed delay in crystallization. Similarly, in an elaborate study by Bach et al., the presence of non-crystalline zinc phosphate nanoparticles as intermediate species, during the formation of crystalline zinc phosphate hydrates, was confirmed.[17] This is consistent with the observed delay, of more than 24 hours, for the appearance of Bragg reflections in a BSA-templated synthesis of zinc phosphate nanocomposites, as reported by Song et al.[18] Therefore, we speculate that the particles observed in sample C initially consist of a non-crystalline zinc phosphate and, similar to that reported by Roming et al., exhibit a significant delay in crystallization due to organic components of the artificial saliva. Lastly, the WAXS pattern of sample E was only indicative of the formation of $Zn_3(PO_4)_2{\cdot}4H_2O$ and no signals of $ZnCl_2$, $CaCl_2{\cdot}2H_2O$, or the possible intermediates were found, indicating that the chemical transformation from $ZnCl_2$ to $Zn_3(PO_4)_2{\cdot}4H_2O$ was only complete after the storage period of two weeks. Based on the described results of the WAXS and XAFS investigations, it is assumed that this transformation proceeds via precursors of amorphous zinc phosphate and hydrozincite, both compounds being sparingly soluble in water.

The formation of $Zn_3(PO_4)_2{\cdot}4H_2O$ instead of $Zn_5(CO_3)_2(OH)_6$ as the final product is in accordance with the respective solubility values reported in literature: For the dissolution of $Zn_3(PO_4)_2{\cdot}4H_2O$ according to Equation (10), Nriagu[19] found a solubility product constant K_P in the order of $10^{-52.2}$ M^9 while for the dissolution of $Zn_5(CO_3)_2(OH)_6$ according to Equation (11), a K_C of $10^{-14.9}$ $M^{2.6}$ can be found.[20] K_P and K_C can be converted to molar solubilities S_P and S_C according to Equation (12) and Equation (13), respectively.

$$Zn_3(PO_4)_2 \cdot 4\,H_2O \overset{K_P}{\rightleftharpoons} 3\,Zn^{2+} + 2\,H_2PO_4^- + 4\,OH^- \tag{10}$$

$$Zn(OH)_{1.2}(CO_3)_{0.4} \overset{K_C}{\rightleftharpoons} Zn^{2+} + 1.2\,OH^- + 0.4CO_3^{2-} \tag{11}$$

From the resultant values of $S_P = 5 \times 10^{-7}$ M and $S_C = 2.5 \times 10^{-6}$ M, the lower solubility of $Zn_3(PO_4)_2{\cdot}4H_2O$ compared to $Zn_5(CO_3)_2(OH)_6$ becomes apparent, which implies a preferred formation of the phosphate.

$$K_P = (3S_P)^3(2S_P)^2(4S_P)^4 \Leftrightarrow S_P = (K_P/27648)^{1/9} \tag{12}$$

$$K_C = S_C(1.2S_C)^{1.2}(0.4S_C)^{0.4} \Leftrightarrow S_C = (K_C/0.48)^{1/2.6} \tag{13}$$

A deeper insight into the changes in chemical composition and crystal structure was obtained by XAFS. Zinc is most commonly found in the +II oxidation state, with only rare cases of Zn^I, found within compounds featuring Zn–Zn-bonds.[21] XAFS experiments confirmed the presence of Zn^{II} within the sample and provided evidence that during the artificial digestion of $ZnCl_2$ no Zn^I species are formed.

A decrease in intensity of the absorption edge over time is clearly visible (enlarged in the inset of Figure 2). The single peak observed from sample A at an energy of 9668 ± 1 eV, slowly decreases and splits into two distinct absorption peaks within the edge region at 9664 ± 1 eV and 9670 ± 1 eV. Furthermore, a less pronounced feature directly after the white line develops at 9677 ± 1 eV. Immediately after the injection of $ZnCl_2$ into artificial saliva (sample C), the Zn *K*-edge is significantly altered and shows decreasing white line intensity, a trend that progresses during the following seven hours, until sample D is obtained. After storage, the white line intensity is further reduced, whilst a doublet forms near the top of the edge in sample E, which is in accordance with the XANES investigations of mineral and synthetic zinc phosphate hydrates undertaken by Castorina et al.[22] Regarding sample A as the precursor and sample E as the end product, the inset of Figure 2 shows that upon injection of $ZnCl_2$, a quick transformation to sample C occurs, whilst the following change via sample D to the product, is much slower. It can also be noted that there are no isosbestic points in the XANES region, demonstrating the potential presence of an unidentified intermediate. Hence, linear combination fitting of the precursor and product to provide further insight into the XANES data is not possible here. Thus, the XANES data supports the assumption previously raised of the transient formation of another zinc compound such as $Zn_5(CO_3)_2(OH)_6$.

EXAFS analysis was performed to follow the change in local coordination around Zn to gain additional insight. With regard to the coordination numbers of zinc in relation to chlorine and oxygen, it can be seen that the former is constantly increasing over time, whilst the latter is decreasing. It is known, from the literature, that $ZnCl_2$ can dissociate completely at low concentrations in aqueous solution.[23] In the presence of water, Zn^{2+} can coordinate octahedrally, whilst also remaining coordinated to Cl^- at higher concentrations, explaining the higher coordination number of Zn^{2+} in relation to Cl^- observed in sample A. The results from EXAFS fitting are given in Table S2 (Supporting Information). Due to high correlation with coordination number, the Debye–Waller factors σ^2 were held constant after refinement from the $ZnCl_2$ precursor. The Zn–Cl bond length was constrained for sample E due to the lack of contribution to the EXAFS. All other parameters were freely refined.

Based on the XAS and WAXS investigations, we assume an initial formation of amorphous zinc phosphate, with the partici-

© 2020 The Authors. Published by Wiley-VCH Verlag GmbH & Co. KGaA, Weinheim

pation of hydrozincite as an intermediate, being a similarly sparingly soluble compound, but not the most thermodynamically stable. Subsequently, the conversion to crystalline $Zn_3(PO_4)_2{\cdot}4H_2O$ proceeds over a period of two weeks, however definitive statements about the kinetics of particle formation go beyond the scope of this study.

Examining further structural parameters obtained from SAXS analysis, the particle number densities N of the primary particles is seen to remain unchanged within uncertainties in samples C and D (at $5.2 \pm 0.1 \times 10^{15}$ mL^{-1}, and $4.6 \pm 0.6 \times 10^{15}$ mL^{-1}, respectively). After two weeks of storage (sample E), a near 20-fold increase in the primary particle number density to $80.6 \pm 0.2 \times 10^{15}$ mL^{-1} is observed.

Particle–particle interactions are represented in SAXS curve fitting by the structure factor, yielding information on the aggregates formed, such as aggregation number N_{agg}, radius of gyration R_g, aggregate radius ξ, and the radius of the single objects within the aggregates r_0. The latter is not to be confused with the mean particle radius R_{mean}, as in the case of particles surrounded by a shell of lower scattering contrast, R_{mean} may not include said shell in contrast to r_0.

In all cases, the mean radius of the particle cores R_{mean} was smaller than the core/shell radius r_0, indicating that within the aggregates formed, particles were separated and stabilized by an intermediate layer, which was assumed to be made up from protein found within the artificial saliva. More specifically, the samples contained α-amylase, BSA, as well as mucin (highly glycosylated proteins). BSA, for instance, is known to possess several cation binding sites, which can be formed by aromatic amino acid residues, and is used in the templated synthesis of inorganic nanostructures.[18,24,25] However, more precise statements regarding the participation of the proteins present in the saliva samples in the nanostructure formation cannot be made at this point due to the high complexity of the reaction media. The structural parameters describing the primary particles aggregating changed over time: mean core/shell radii decreased significantly, from $r_0 = 2.2 \pm 0.2$ nm to 1.7 ± 0.1 nm, during the first seven hours of incubation time between the collection of samples C and D, and remained the same within uncertainties during the following storage over two weeks yielding sample E. This indicates a likewise change of the thickness of the stabilizing shell, i.e. the particles became more tightly packed alongside their transformation into crystalline zinc phosphate.

Contrary, aggregate radius ξ, radius of gyration R_g, and aggregation number N_{agg} did only change significantly during the period of storage between collection of samples D and E. It was found that the aggregate radius increased from $\xi = 15.7 \pm 0.2$ nm in sample D to 22.4 ± 0.1 nm in sample E, which is reflected in likewise increasing radii of gyration (from $R_g = 36 \pm 1$ nm to 49 ± 1 nm) and aggregation numbers (from $N_{agg} = 4400 \pm 200$ to 9000 ± 100). These observations indicate that during the first seven hours, in which the transformation of $ZnCl_2$ into crystalline $Zn_3(PO_4)_2{\cdot}4H_2O$ occurs, only the particle concentration within the aggregates increased. In contrast, the particles remained unchanged during subsequent storage, while the aggregates grew in size and approximately 20-fold in number density.

Conclusion

Upon the addition of $ZnCl_2$ to artificial saliva, nanoparticles with a mean radius of 1.1 ± 0.2 nm and a size distribution width of 0.7 ± 0.2 nm were observed, and they formed aggregates with radii of gyration of 37 ± 1 nm, as determined from SAXS. Within these aggregates, the particles are thought to adhere via a shell of the protein found within artificial saliva. The initial composition of these nascent particles could not be determined directly, however, they were converted to $Zn_3(PO_4)_2{\cdot}4H_2O$ within seven hours of incubation, alongside an intermediate species [thought to be $Zn_5(CO_3)_2(OH)_6$]. Comparisons to literature studies suggests that the primary particles consist of amorphous zinc phosphate precursors, and throughout the incubation period, these slowly form crystalline $Zn_3(PO_4)_2{\cdot}4H_2O$.

The changes in particle size distribution parameters of primary particles and their aggregates at incubation times of five minutes, seven hours and after a period of storage of two weeks are depicted in Figure 5. During the incubation period, the particle number density remained essentially the same (within uncertainties), whilst the aggregates became more tightly packed, i.e. the thickness of the particle-surrounding shell decreased. Meanwhile, the chemical transformation of $ZnCl_2$ into $Zn_3(PO_4)_2{\cdot}4H_2O$ proceeded with the involvement of an intermediate. In the subsequent storage period of two weeks, the particle number concentration increased about 20-fold as the aggregates grew. While they initially consisted of 3200 ± 900 primary particles, the aggregation number after storage was 9000 ± 100. Thus, it was demonstrated that upon contact of solubilized, ionic zinc to artificial saliva, small $Zn_3(PO_4)_2{\cdot}4H_2O$ nanoparticles can be formed.

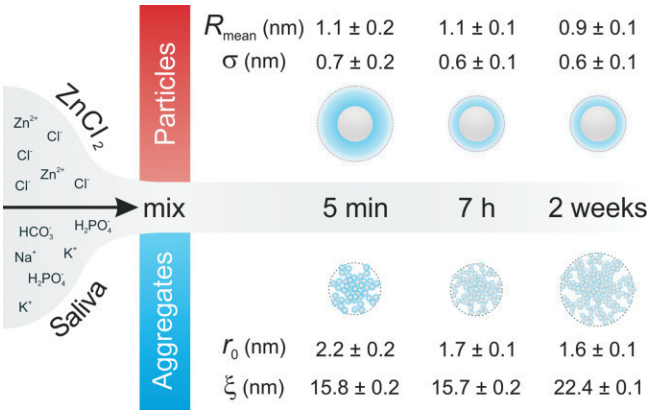

Figure 5. Scheme depicting the changes in particle size distribution parameters of primary particles and their aggregates over time, regarding mean particle core radius, R_{mean}, size distribution width, σ, mean particle core/shell radius, r_0, and aggregate radius, ξ.

The assumption that the proteins, within the saliva, temporarily stabilize zinc phosphate nanoparticles seems rational as it is well-known that proteins have previously been utilized as colloidal stabilizers in the preparation of inorganic nanoparticles.[18,24,25] Therein, proteins are frequently used in biotemplated nanoparticle synthesis. Most frequently used is BSA, which in our study is present in saliva at a concentration of 0.48 g L^{-1}. As an example, the production of a BSA templated

© 2020 The Authors. Published by Wiley-VCH Verlag GmbH & Co. KGaA, Weinheim

zinc phosphate $Zn_3(PO_4)_2$@BSA was reported by Song et al.[18] Their study reviews the biotemplated synthesis of metal phosphates, most of which were synthesized for application in catalysis.

In contrast, the particles of our study are not foreseen for technical applications. On the other hand, regularization of crystal formation is hotly debated in biomineralization. Therein, it is evident that proteins play a substantial role in healthy mineralization such as amorphous calcium phosphate in bone growth but also in pathological mineralization.[26] Examples for undesired biominerals are kidney stones, atheromatous plaque and dental calculus. The zinc phosphate formation of our present study also has an amorphous initial state as it seems to be a typical phenomenon in biomineralization. For example, Gebauer et al. were the first to discover that stable prenucleation clusters play an important role as intermediate species in the crystallization of calcium carbonate.[27]

In conclusion, the zinc phosphate nanoparticles may also form in vivo if food and cosmetics products, containing the permitted zinc salt concentrations, are ingested, which could be a source of unintentional mineral formation. Similarly, these results may be of relevance for the design of biological studies involving the use of, for example, ionic zinc and phosphate-containing buffers.

Experimental Section

Materials

Zinc(II) chloride ($ZnCl_2$) was purchased from Merck, bovine serum albumin (BSA) from Sigma-Aldrich and all chemicals for artificial saliva from AppliChem, Carl Roth, NeoLab or Sigma-Aldrich according to Table 1. Ultrapure water (*Milli-Q*, 18.2 MΩ•cm at 25 °C) was used.

Artificial Saliva

We adapted an in vitro artificial digestion procedure based on the German standard DIN 19378.[7] Solutions of $ZnCl_2$ (68.1 mg, sample A) and BSA (25 mg), in 1 mL of ultrapure water, respectively, were added to 50 mL of artificial saliva (composed according to Table 1, pH = 6.4 ± 0.05, artificial saliva with BSA is referred to as sample B) and incubated at 37 °C for 5 min (sample C). Further samples were taken after 7 h incubation time (sample D) and after a period of storage at ca. 4 °C of two weeks (sample E).

SAXS/WAXS Measurements

Small- and wide-angle X-ray scattering (SAXS/WAXS) measurements were performed on a customized Xeuss 2.0 (Xenocs, France). X-rays were generated from a microfocus X-ray tube with a copper target, and a multilayer optic was employed to parallelize and monochromatize the beam to the Cu-K_α wavelength of 0.1542 nm. The liquid samples were examined in flow by continuous pumping through a cell bearing silicon nitride windows. Data collection was performed using an in-vacuum Eiger 1M detector (Dectris, Switzerland) which was placed at multiple distances between 51–2507 mm from the sample. The resulting data has been processed and scaled to absolute units using the DAWN software package according to standardized procedures.[28,29]

XAS Measurements

XAS measurements were carried out at the SuperXAS beamline of the Swiss Light Source. The storage ring operated at 2.4 GeV in top-up mode with a ring current of 400 mA. The polychromatic X-ray beam resulting from a 2.9 Tesla bending magnet was collimated by a silicon-coated mirror at 2.5 mrad (which also served to reduce higher-order harmonics) and subsequently monochromatized by a Si(111) channel-cut monochromator, which allowed data collection in quick-scanning extended X-ray absorption fine-structure spectroscopy (QEXAFS) at 1 Hz. The beam was focused using a Rh coated toroidal mirror with a focal spot size of 1000 × 200 μm. Spectra were collected in transmission mode using 15 cm long, 2 bar N_2-filled ionization chambers. A Zn reference foil mounted between the second and third ionization chamber was measured simultaneously for absolute energy calibration. The QEXAFS spectra were processed using ProQEXAFS to extract individual XAS spectra,[32] calibrate and normalize. Due to the inherent oversampling of the XAS spectra, radial basis function interpolation was employed to reduce the data point density. In the XANES region an energy step of 0.25 eV was used. In the EXAFS region a constant *k*-step of 0.025 $Å^{-1}$ was chosen. Fitting of the EXAFS was performed using the Demeter software package.[30]

Acknowledgments

Open access funding enabled and organized by Projekt DEAL.

Keywords: Biomineralization · Nanoparticles · Structure elucidation · Zinc · Artificial digestion

[1] C. J. Boreiko, *J. Toxicol. Environ. Health Part A* **2010**, *73*, 166–174.
[2] *Institute of Medicine, Dietary Reference Intakes for Vitamin A, Vitamin K, Arsenic, Boron, Chromium, Copper, Iodine, Iron, Manganese, Molybdenum, Nickel, Silicon, Vanadium, and Zinc*, National Academies Press, Washington, D **2001**.
[3] N. F. Krebs, *J. Nutr.* **2000**, *130*, 1374S–1377S.
[4] The European Commission, *Off. J. Eur. Union: Legis.* **2009**, *52*, L 342, 137.
[5] T. J. Porea, J. W. Belmont, D. H. Mahoney Jr., *J. Pediatr.* **2000**, *136*, 688–690.
[6] A. Nel, *Science* **2006**, *311*, 622–627.
[7] Norm DIN 19738:2004-07, Soil quality - Absorption availability of organic and inorganic pollutants from contaminated soil material, **2004**.
[8] The National Research Centre for the Working Environment (NRCWE), NANOGENOTOX: Final protocol for producing suitable manufactured nanomaterial exposure media, tech. rep. **2011**.
[9] J. Teixeira, *J. Appl. Crystallogr.* **1988**, *21*, 781–785.
[10] R. Ferretti, J. Zhang, J. Buffle, *J. Colloid Interface Sci.* **1998**, *208*, 509–517.
[11] P. Comodi, S. Nazzareni, P. F. Zanazzi, S. Speziale, *Am. Mineral.* **2008**, *93*, 1530–1537.
[12] A. Whitaker, *Acta Crystallogr., Sect. AActa Crystallogr., Sect. B Struct. Crystallogr. Cryst. Chem.* **1975**, *31*, 2026–2035.
[13] M. C. Hales, R. L. Frost, *Polyhedron* **2007**, *26*, 4955–4962.
[14] O. Pawlig, R. Trettin, *Mater. Res. Bull.* **1999**, *34*, 1959–1966.
[15] S. Ghose, *Acta Crystallogr.* **1964**, *17*, 1051–1057.
[16] M. Roming, C. Feldmann, Y. S. Avadhut, J. Schmedt auf der Günne, *Chem. Mater.* **2008**, *20*, 5787–5795.
[17] S. Bach, V. R. Celinski, M. Dietzsch, M. Panthöfer, R. Bienert, F. Emmerling, J. Schmedt auf der Günne, W. Tremel, *J. Am. Chem. Soc.* **2015**, *137*, 2285–2294.
[18] Y. Song, H. Ji, M. Wang, L. He, R. Song, Z. Zhang, *Appl. Surf. Sci.* **2017**, *422*, 228–238.
[19] J. O. Nriagu, *Geochim. Cosmochim. Acta* **1973**, *37*, 2357–2361.
[20] A. K. Alwan, P. A. Williams, *Transit. Met. Chem.* **1979**, *4*, 128–132.

© 2020 The Authors. Published by Wiley-VCH Verlag GmbH & Co. KGaA, Weinheim

[21] S. Riedel, M. Kaupp, *Coord. Chem. Rev.* **2009**, *253*, 606–624.
[22] E. Castorina, E. D. Ingall, P. L. Morton, D. A. Tavakoli, B. Lai, *J. Synchrotron Radiat.* **2019**, *26*, 1302–1309.
[23] P. D'Angelo, A. Zitolo, F. Ceccacci, R. Caminiti, G. Aquilanti, *J. Chem. Phys.* **2011**, *135*, 154509.
[24] J. Xie, J. Y. Lee, D. I. C. Wang, *J. Phys. Chem. C* **2007**, *111*, 10226–10232.
[25] S. Zhao, Y. Gao, J. Tan, Y. Zhu, X. Ying, M. Zhang, X. Yu, B. You, *SN Appl. Sci.* **2019**, *1*, 917.
[26] H. Cölfen, *Nat. Mater.* **2010**, *9*, 960–961.
[27] D. Gebauer, A. Völkel, H. Cölfen, *Science* **2008**, *322*, 1819–1822.
[28] B. R. Pauw, A. J. Smith, T. Snow, N. J. Terrill, A. F. Thünemann, *J. Appl. Crystallogr.* **2017**, *50*, 1800–1811.
[29] J. Filik, A. W. Ashton, P. C. Y. Chang, P. A. Chater, S. J. Day, M. Drakopoulos, M. W. Gerring, M. L. Hart, O. V. Magdysyuk, S. Michalik, A. Smith, C. C. Tang, N. J. Terrill, M. T. Wharmby, H. Wilhelm, *J. Appl. Crystallogr.* **2017**, *50*, 959–966.
[30] B. Ravel, M. Newville, *J. Synchrotron Radiat.* **2005**, *12*, 537–541.
[31] L. Voss, P. E. J. Saloga, V. Stock, L. Böhmert, A. Braeuning, A. F. Thünemann, A. Lampen, H. Sieg, *ACS Appl. Nano Mater.* **2020**, *3*, 724–733.
[32] A. H. Clark, J. Imbao, R. Frahm, M. Nachtegaal, *J. Synchrotron Rad.* **2020**, *27*, 551–557.

Received: May 28, 2020

© 2020 The Authors. Published by Wiley-VCH Verlag GmbH & Co. KGaA, Weinheim

Supporting Information

Zinc Phosphate Nanoparticles Produced in Saliva

Patrick E. J. Saloga, Glen J. Smales, Adam H. Clark,
Andreas F. Thünemann*

Contents

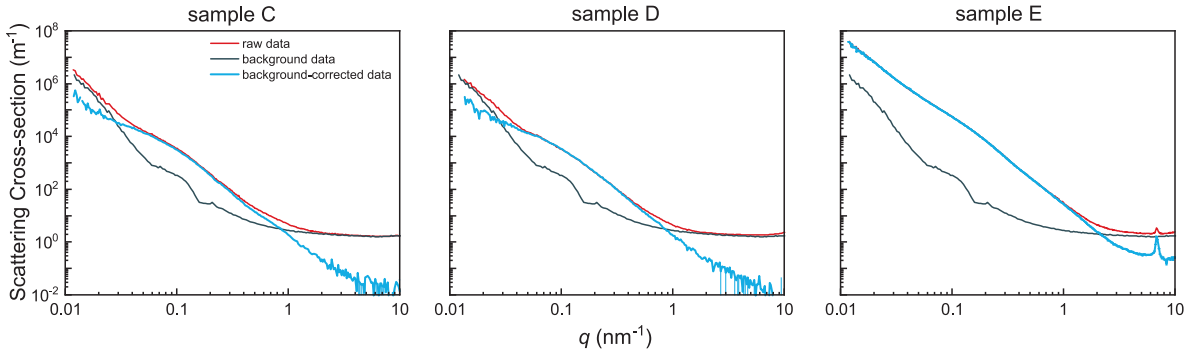

Figure S1: SAXS raw data with background (artificial saliva with BSA in the measurement cell) and background-corrected data of samples C, D, and E.

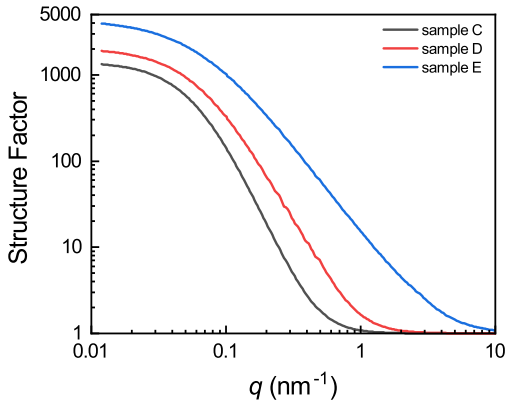

Figure S2: Structure factors used in SAXS curve fits of samples C, D, and E.

Table S1: Particle size distribution parameters for samples C, D, and E, derived from SAXS analysis.

Contribution	Parameter	Symbol	Unit	Sample C	Sample D	Sample E
Primary particles	Particle number density	N	10^{15} mL^{-1}	5.2 ± 0.1	4.6 ± 0.6	80.6 ± 0.2
	Median radius	R_{median}	nm	0.9 ± 0.2	1.0 ± 0.1	0.8 ± 0.1
	Width parameter	$\sigma_{\log}$		0.52 ± 0.04	0.49 ± 0.01	0.53 ± 0.01
	Mean radius (core)	R_{mean}	nm	1.1 ± 0.2	1.1 ± 0.1	0.9 ± 0.1
	Distribution width	σ	nm	0.7 ± 0.2	0.6 ± 0.1	0.6 ± 0.1
Aggregates	Mean radius (core/shell)	r_0	nm	2.2 ± 0.2	1.7 ± 0.1	1.6 ± 0.1
	Aggregate radius	ξ	nm	15.8 ± 0.2	15.7 ± 0.2	22.4 ± 0.1
	Fractal dimension	D		2.87 ± 0.07	2.75 ± 0.01	2.64 ± 0.01
	Radius of gyration	R_g	nm	37 ± 1	36 ± 1	49 ± 1
	Aggregation number	N_{agg}		3200 ± 900	4400 ± 200	9000 ± 100
Background		a		0.02	0.02	0.25
		b		0.0078	0.0078	0.82

Table S2: EXAFS fitting results obtained from fits shown in Figure 3, with coordination numbers CN, Debye-Waller factors σ^2, and bond lengths R, with regard to chlorine (Cl) and oxygen atoms (O).

Sample	CN Cl	σ^2 Cl ($\mathring{A}^2$)	R Cl ($\mathring{A}$)	CN O	σ^2 O ($\mathring{A}^2$)	R O ($\mathring{A}$)
A	2.6	0.0045	2.36 ± 0.01	2.5	0.0045	1.95 ± 0.01
C	1.7	0.0045	2.36 ± 0.01	2.9	0.0045	1.93 ± 0.01
D	1.2	0.0045	2.36 ± 0.01	3.1	0.0045	1.93 ± 0.01
E	0	0.0045	2.36	3.7	0.0045	1.93 ± 0.01

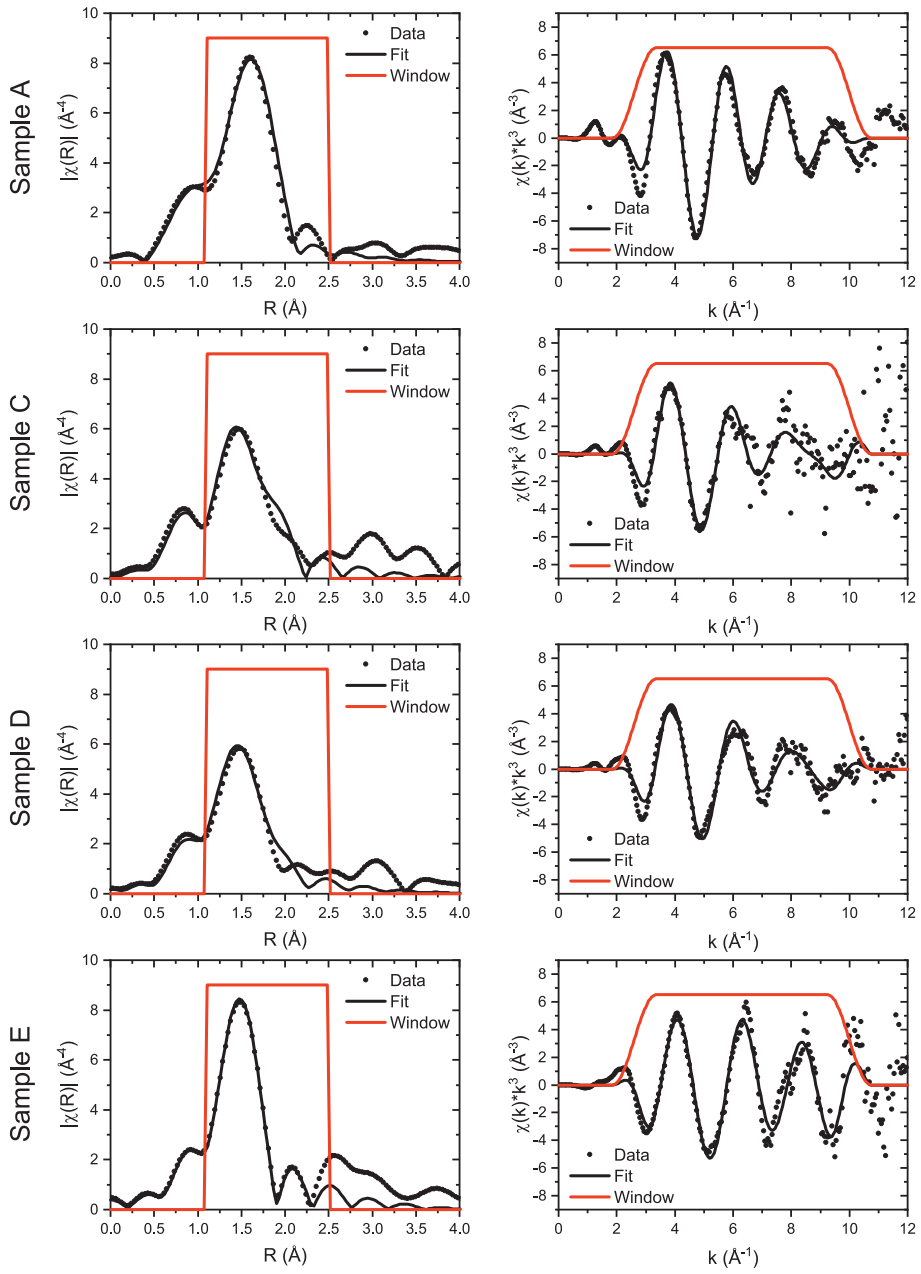

Figure S3: EXAFS data (dots) with fits (black, solid lines) and window functions used (red, solid lines) for samples A, C, D, and E in both R- (left) and k-space (right).

5 CONCLUSIONS AND PERSPECTIVES

The work presented in this thesis initially depicts the synthesis of spherical zinc oxide nanoparticles in organic dispersion in project **1**. The use of microwave-assisted synthesis enabled the production of aggregate-free ZnO nanoparticles within a reaction time shortened by more than 99% in comparison to conventional synthesis methods.[30] By selecting a synthesis temperature between 125 °C and 200 °C, the particle size, as well as the related lattice and optical properties, could be adjusted. In the investigated size range, lattice strain, ϵ, stress, σ, and deformation energy, u, which are dependent upon the crystallite size according to a set of power law equations that are speculated to apply universally to crystallites smaller than 20 nm.

Certain potential applications for these ZnO nanoparticles, for instance in biological environments, require aqueous particle dispersions. A phase transfer can be facilitated, for these initially hydrophobic particles, through functionalisation with the surfactant polysorbate 80. During this phase transfer, in project **2**, the particles are heated, which in turn induces particle growth, thus providing more possibilities to tune their particle size. The obtained, water-stable particles are also photocatalytically active, a property that was investigated *via* the degradation of methylene blue.

Size characterisation was predominantly carried out by small-angle X-ray scattering, which is particularly suitable for the determination of particle size distributions in complex media. This was demonstrated in the second part of this work in projects **3** and **4** when studying nanoparticles in digestive fluids. Zinc oxide, as well as ionic zinc compounds, are commonly added to food and cosmetic products. Hence, the potential chemical or structural transformations of these substances were studied in an artificial digestion process. It was found that contact of ZnO and $ZnCl_2$ to saliva can induce the *de novo* formation of nanoparticles irrespective of size, concentration or functionalisation of the ingested material or the presence of food simulants. After the intermittent dissolution of all zinc-containing structures in gastric juice, new particles were formed in the intestinal juice. In all cases, the *de novo* formation of particles was thought to yield zinc phosphate compounds.

The addition of $ZnCl_2$ to artificial saliva was examined more closely, and the formation of small nanoparticles was observed, which formed nano-sized aggregates, presumably through adhesion facilitated *via* a protein-containing shell. After seven hours of incubation, these nanoparticles were found to consist of $Zn_3(PO_4)_2 \cdot 4\,H_2O$, alongside the presence of an intermediate species, that is thought to be $Zn_5(CO_3)_2(OH)_6$ from observations of the WAXS data. During the subsequent two-weeks of storage, the aggregates densify, i.e. the thickness of the protein shell decreased, and then the aggregates grow to contain three times the number of particles.

In summary, the first part of this thesis focuses on the development of synthetic routes for obtaining organic and aqueous dispersions of zinc oxide

nanoparticles with adjustable size and correlated optical and structural properties, making these particles suitable candidates for certified reference materials. With their finely tunable radii in the range of 2.3 nm to 5.7 nm, these nanoparticles could become calibrants for sizing methods such as light or X-ray scattering at the lower nanoscale. Studies concerning size-dependent optical or structural properties of ZnO at the lower nanoscale could benefit significantly from the synthesis strategies presented in this dissertation. Particles with selectable ultraviolet absorbance or luminescence properties could be utilised as optical probes, particularly in aqueous dispersion for biological applications.

In a broader context, the results of the second part of this dissertation are of particular relevance to the application of zinc compounds in biological systems, both within and outside the scientific community. No toxicological evaluations are undertaken in this work; however, the characterisation of the chemical and structural effects of an artificial digestion process on zinc compounds provides valuable information for future biological and toxicological studies in this respect.

6 REFERENCES

[1] G. Loussouarn, I. Lozano, S. Panhard, C. Collaudin, C. El Rawadi, G. Genain, *Eur. J. Dermatology* **2016**, *26*, 144–154.

[2] I. Bars, J. Terning, *Extra Dimensions in Space and Time*, (Ed.: F. Nekoogar), Springer New York, New York, NY, **2010**.

[3] C. Taylor, *The Atomists: Leucippus and Democritus. Fragments : A Text and Translation with a Commentary*, University of Toronto Press, Toronto Buffalo London, **1999**.

[4] B. Pullman, *The Atom in the History of Human Thought*, Oxford University Press, New York, **2001**.

[5] W. L. Bragg, *London Edinburgh Dublin Philos. Mag. J. Sci.* **1920**, *40*, 169–189.

[6] R. P. Feynman, *Resonance* **2011**, *16*, 890–905.

[7] N. Taniguchi, *Proc. Int. Conf. Prod. Eng. Tokyo Part II Japan Soc. Precis. Eng.* **1974**.

[8] H. Weller, *Angew. Chem. Int. Ed.* **1993**, *32*, 41–53.

[9] ISO, Nanotechnologies - Vocabulary - Part 1: Core terms (ISO/TS 80004-1:2015), tech. rep., **2015**.

[10] The European Commission, Commission recommendation of 18 October 2011 on the definition of nanomaterial (2011/696/EU). **2011**.

[11] M. Haase, H. Schäfer, *Angew. Chem. Int. Ed.* **2011**, *50*, 5808–5829.

[12] A. Ekimov, A. Efros, A. Onushchenko, *Solid State Commun.* **1985**, *56*, 921–924.

[13] Y. Wang, N. Herron, *J. Phys. Chem.* **1991**, *95*, 525–532.

[14] A. Rastelli, S. Kiravittaya, O. G. Schmidt in *Single Semiconductor Quantum Dots*, **2009**, pp. 31–69.

[15] A. Moezzi, A. M. McDonagh, M. B. Cortie, *Chem. Eng. J.* **2012**, *185-186*, 1–22.

[16] H. Sicius, *Zinkgruppe: Elemente der zweiten Nebengruppe*, Springer Fachmedien Wiesbaden, Wiesbaden, **2017**.

[17] W. J. Jones, *Historisches Lexikon deutscher Farbbezeichnungen*, Akademie Verlag, Berlin, **2013**.

[18] H. Roscoe, C. Schorlemmer, *Ausführliches Lehrbuch der Chemie. Zweiter Band. Die Metalle und Spectralanalyse.* Friedrich Vieweg und Sohn, Braunschweig, **1879**, p. 207.

[19] C. Klingshirn, *ChemPhysChem* **2007**, *8*, 782–803.

[20] A. Sirelkhatim, S. Mahmud, A. Seeni, N. H. M. Kaus, L. C. Ann, S. K. M. Bakhori, H. Hasan, D. Mohamad, *Nanomicro Lett.* **2015**, *7*, 219–242.

[21] M. Heckmann in *Fortschritte der Dermatologie*, Steinkopff, Heidelberg, **2002**, pp. 61–74.

[22] G. Heideman, R. N. Datta, J. W. M. Noordermeer, B. van Baarle, *J. Appl. Polym. Sci.* **2005**, *95*, 1388–1404.

[23] S. Tolksdorf, *Z. Phys. Chem.* **1928**, *132U*, 161–184.

[24] H. J. Yearian, *Phys. Rev.* **1935**, *48*, 631–639.

[25] A. Janotti, C. G. Van de Walle, *Rep. Prog. Phys.* **2009**, *72*, 126501.

[26] R. Breit in *Fortschritte der Dermatologie*, Steinkopff, Heidelberg, **2002**, pp. 23–32.

[27] T. J. Jacobsson, T. Edvinsson, *Inorg. Chem.* **2011**, *50*, 9578–9586.

[28] Ü. Özgür, Y. I. Alivov, C. Liu, A. Teke, M. A. Reshchikov, S. Doğan, V. Avrutin, S.-J. Cho, H. Morkoç, *J. Appl. Phys.* **2005**, *98*, 041301.

[29] Y. Chen, D. M. Bagnall, H.-J. Koh, K.-T. Park, K. Hiraga, Z. Zhu, T. Yao, *J. Appl. Phys.* **1998**, *84*, 3912–3918.

[30] S. Ehlert, T. Lunkenbein, J. Breu, S. Förster, *Colloids Surfaces A Physicochem. Eng. Asp.* **2014**, *444*, 76–80.

[31] P. Casey in *Nanostructure Control of Materials*, Elsevier, **2006**, pp. 1–31.

[32] V. K. LaMer, R. H. Dinegar, *J. Am. Chem. Soc.* **1950**, *72*, 4847–4854.

[33] M. Herbst, E. Hofmann, S. Förster, *Langmuir* **2019**, *35*, 11702–11709.

[34] P. E. J. Saloga, A. F. Thünemann, *Langmuir* **2019**, *35*, 12469–12482.

[35] P. E. J. Saloga, C. Kästner, A. F. Thünemann, *Langmuir* **2018**, *34*, 147–153.

[36] J. H. van't Hoff, *Études de dynamique chimique*, Frederik Muller & Co., Amsterdam, **1884**, pp. 114–118.

[37] S. Arrhenius, *Z. Phys. Chem.* **1889**, *4U*, 226–248.

[38] C. O. Kappe, *Acc. Chem. Res.* **2013**, *46*, 1579–1587.

[39] W. Brown, K. Schillen, M. Almgren, S. Hvidt, P. Bahadur, *J. Phys. Chem.* **1991**, *95*, 1850–1858.

[40] C. A. Dreiss, *Soft Matter* **2007**, *3*, 956.

[41] DIN Deutsches Institut für Normung e.V., Partikelgrößenanalyse – Dynamische Lichtstreuung (DLS) (ISO 22412:2017), tech. rep., **2018**.

[42] P. A. Hassan, S. Rana, G. Verma, *Langmuir* **2015**, *31*, 3–12.

[43] W. C. Röntgen, *Ann. Phys.* **1898**, *300*, 12–17.

[44] P. Debye, *Ann. Phys.* **1915**, *351*, 809–823.

[45] B. Ruta, Y. Chushkin, G. Monaco, L. Cipelletti, E. Pineda, P. Bruna, V. M. Giordano, M. Gonzalez-Silveira, *Phys. Rev. Lett.* **2012**, *109*, 165701.

[46] F. Perakis, K. Amann-Winkel, F. Lehmkühler, M. Sprung, D. Mariedahl, J. A. Sellberg, H. Pathak, A. Späh, F. Cavalca, D. Schlesinger, A. Ricci, A. Jain, B. Massani, F. Aubree, C. J. Benmore, T. Loerting, G. Grübel, L. G. M. Pettersson, A. Nilsson, *Proc. Natl. Acad. Sci. U.S.A.* **2017**, *114*, 8193–8198.

[47] Q. Zhang, D. Bahadur, E. M. Dufresne, P. Grybos, P. Kmon, R. L. Leheny, P. Maj, S. Narayanan, R. Szczygiel, S. Ramakrishnan, A. Sandy, *Phys. Rev. Lett.* **2017**, *119*, 178006.

[48] T. Li, A. J. Senesi, B. Lee, *Chem. Rev.* **2016**, *116*, 11128–11180.

[49] E. Mylonas, D. I. Svergun, *J. Appl. Crystallogr.* **2007**, *40*, s245–s249.

[50] O. Kratky, H. Stabinger, *Colloid Polym. Sci.* **1984**, *262*, 345–360.

[51] O. Glatter, *Scattering Methods and their Application in Colloid and Interface Science*, Elsevier, **2018**.

[52] O. Moscosco Londoño, P. Tancredi, P. Rivas, D. Muraca, L. M. Socolovsky, M. Knobel in *Handb. Mater. Charact.* Springer International Publishing, Cham, **2018**, pp. 37–75.

[53] W. H. Bragg, W. L. Bragg, *Proc. R. Soc. London Ser. A* **1913**, *88*, 428–438.

[54] P. Debye, A. M. Bueche, *J. Appl. Phys.* **1949**, *20*, 518–525.

[55] G. Porod, *Kolloid Z.* **1951**, *124*, 83–114.

[56] N. Stribeck, *X-Ray Scattering of Soft Matter*, Springer Berlin Heidelberg, Berlin, Heidelberg, **2007**.

[57] I. Bressler, B. R. Pauw, A. F. Thünemann, *J. Appl. Crystallogr.* **2015**, *48*, 962–969.

[58] I. Breßler, J. Kohlbrecher, A. F. Thünemann, *J. Appl. Crystallogr.* **2015**, *48*, 1587–1598.

[59] J. Babinet, *C.R. Acad. Sci.* **1837**, *4*, 638–648.

[60] Lord Rayleigh, *Proc. R. Soc. London Ser. A* **1910**, *84*, 25–46.

[61] J. S. Pedersen, *Adv. Colloid Interface Sci.* **1997**, *70*, 171–210.

[62] J. K. Percus, G. J. Yevick, *Phys. Rev.* **1958**, *110*, 1–13.

[63] A. Vrij, *J. Chem. Phys.* **1979**, *71*, 3267–3270.

[64] J. Teixeira, *J. Appl. Crystallogr.* **1988**, *21*, 781–785.

[65] R. Ferretti, J. Zhang, J. Buffle, *J. Colloid Interface Sci.* **1998**, *208*, 509–517.

[66] L. Voss, P. E. J. Saloga, V. Stock, L. Böhmert, A. Braeuning, A. F. Thünemann, A. Lampen, H. Sieg, *ACS Appl. Nano Mater.* **2020**, *3*, 724–733.

[67] C. Weidenthaler, *Nanoscale* **2011**, *3*, 792.

[68] L. Alexander, *J. Appl. Phys.* **1954**, *25*, 155–161.

[69] A. Kalita, M. P. Kalita, *Physica E Low Dimens. Syst. Nanostruct.* **2017**, *92*, 36–40.

[70] W. Ruland, *Acta Crystallogr.* **1965**, *18*, 581–581.

[71] P. Scherrer, *Nachr. Ges. Wiss. Göttingen* **1918**, *2*, 98–100.

[72] G. Williamson, W. Hall, *Acta Metall.* **1953**, *1*, 22–31.

[73] A. K. Zak, M. E. Abrishami, W. A. Majid, R. Yousefi, S. Hosseini, *Ceram. Int.* **2011**, *37*, 393–398.

[74] H. Fricke, *Phys. Rev.* **1920**, *16*, 202–215.

[75] O. Müller, M. Nachtegaal, J. Just, D. Lützenkirchen-Hecht, R. Frahm, *J. Synchrotron Radiat.* **2016**, *23*, 260–266.

[76] A. Beer, *Ann. der Phys. und Chemie* **1852**, *162*, 78–88.

[77] H. Haken, H. C. Wolf, *Atom- und Quantenphysik*, Springer Berlin Heidelberg, Berlin, Heidelberg, **2004**.

[78] G. Bunker, *Introduction to XAFS*, Cambridge University Press, Cambridge, **2010**.

[79] C. T. Chantler, *J. Phys. Chem. Ref. Data* **1995**, *24*, 71–643.

[80] C. T. Chantler, *J. Phys. Chem. Ref. Data* **2000**, *29*, 597–1056.

[81] S. Calvin, *XAFS for Everyone*, CRC Press, **2013**.

[82] P. E. J. Saloga, G. J. Smales, A. H. Clark, A. F. Thünemann, *Eur. J. Inorg. Chem.* **2020**, *2020*, 3654–3661.

[83] P. A. M. Dirac, *Proc. R. Soc. London Ser. A* **1927**, *114*, 243–265.

[84] J. J. Rehr, R. C. Albers, *Rev. Mod. Phys.* **2000**, *72*, 621–654.

[85] A. H. Clark, J. Imbao, R. Frahm, M. Nachtegaal, *J. Synchrotron Radiat.* **2020**, *27*, 551–557.

[86] B. Ravel, M. Newville, *J. Synchrotron Radiat.* **2005**, *12*, 537–541.

[87] L. Voss, P. E. J. Saloga, V. Stock, L. Böhmert, A. Braeuning, A. F. Thünemann, A. Lampen, H. Sieg, *ACS Appl. Nano Mater.* **2020**, acsanm.oco1054.

[88] E. Solati, D. Dorranian, *J. Appl. Spectrosc.* **2017**, *84*, 490–497.

[89] D. Verma, A. Kole, P. Kumbhakar, *J. Alloys Compd.* **2015**, *625*, 122–130.

[90] A. Kalita, M. P. C. Kalita, *Appl. Phys. A* **2015**, *121*, 521–524.

[91] K. Ocakoglu, S. Mansour, S. Yildirimcan, A. A. Al-Ghamdi, F. El-Tantawy, F. Yakuphanoglu, *Spectrochim. Acta Part A* **2015**, *148*, 362–368.

[92] P. Bindu, S. Thomas, *J. Theor. Appl. Phys.* **2014**, *8*, 123–134.

[93] M. Kahouli, A. Barhoumi, A. Bouzid, A. Al-Hajry, S. Guermazi, *Superlattices Microstruct.* **2015**, *85*, 7–23.

[94] A. J. Reddy, M. Kokila, H. Nagabhushana, R. Chakradhar, C. Shivakumara, J. Rao, B. Nagabhushana, *J. Alloys Compd.* **2011**, *509*, 5349–5355.

[95] B. Manikandan, T. Endo, S. Kaneko, K. R. Murali, R. John, *J. Mater. Sci. Mater. Electron.* **2018**, *29*, 9474–9485.

[96] D. Arora, K. Asokan, S. Kumar, S. Kaur, P. Kaur, G. P. Singh, A. Mahajan, S. Kalia, N. Kalia, K. Seth, P. Kaur, D. P. Singh, *J. Am. Ceram. Soc.* **2018**, *101*, 4023–4037.

[97] S. Goel, N. Sinha, B. Kumar, *Physica E Low Dimens. Syst. Nanostruct.* **2019**, *105*, 29–40.

[98] W. Ren, G. Tian, S. Jian, Z. Gu, L. Zhou, L. Yan, S. Jin, W. Yin, Y. Zhao, *RSC Adv.* **2012**, *2*, 7037.

[99] H. Kisch, D. Bahnemann, *J. Phys. Chem. Lett.* **2015**, *6*, 1907–1910.

[100] B. R. Pauw, A. J. Smith, T. Snow, N. J. Terrill, A. F. Thünemann, *J. Appl. Crystallogr.* **2017**, *50*, 1800–1811.

[101] J. Ollig, V. Kloubert, I. Weßels, H. Haase, L. Rink, *Metals* **2016**, *6*, 71.

[102] C. Cheng, R. Xin, Y. Leng, D. Yu, N. Wang, *Inorg. Chem.* **2008**, *47*, 7868–7873.

[103] The European Commission, *Off. J. Eur. Union Legis.* **2009**, *52*, L 342, 137.

[104] P. Comodi, S. Nazzareni, P. F. Zanazzi, S. Speziale, *Am. Mineral.* **2008**, *93*, 1530–1537.

[105] A. Whitaker, *Acta. Crystallogr. B. Struct. Sci. Cryst. Eng. Mater.* **1975**, *31*, 2026–2035.

[106] S. Ghose, *Acta Crystallogr.* **1964**, *17*, 1051–1057.

[107] M. Roming, C. Feldmann, Y. S. Avadhut, J. S. auf der Günne, *Chem. Mater.* **2008**, *20*, 5787–5795.

[108] S. Bach, V. R. Celinski, M. Dietzsch, M. Panthöfer, R. Bienert, F. Emmerling, J. Schmedt auf der Günne, W. Tremel, *J. Am. Chem. Soc.* **2015**, *137*, 2285–2294.

[109] A. K. Alwan, P. A. Williams, *Transit. Met. Chem.* **1979**, *4*, 128–132.

[110] J. O. Nriagu, *Geochim. Cosmochim. Acta* **1973**, *37*, 2357–2361.

A APPENDICES

A.1 PUBLICATION LIST

Publications included in this thesis:

Patrick E. J. Saloga, Andreas F. Thünemann. **Microwave-Assisted Synthesis of Ultrasmall Zinc Oxide Nanoparticles.** *Langmuir* 2019, 35, 38, 12469-12482.
DOI: 10.1021/acs.langmuir.9b01921

Linn Voss, Patrick E. J. Saloga, Valerie Stock, Linda Böhmert, Albert Braeuning, Andreas F. Thünemann, Alfonso Lampen, Holger Sieg. **Environmental Impact of ZnO Nanoparticles Evaluated by in Vitro Simulated Digestion.** *ACS Appl. Nano Mater.* 2020, 3, 1, 724-733.
DOI: 10.1021/acsanm.9b02236

Linn Voss, Patrick E. J. Saloga, Valerie Stock, Linda Böhmert, Albert Braeuning, Andreas F. Thünemann, Alfonso Lampen, Holger Sieg. **Correction to Environmental Impact of ZnO Nanoparticles Evaluated by in Vitro Simulated Digestion.** *ACS Appl. Nano Mater.* 2020, 3, 5, 4914.
DOI: 10.1021/acsanm.0c01054

Patrick E. J. Saloga, Glen J. Smales, Adam H. Clark, Andreas F. Thünemann. **Zinc Phosphate Nanoparticles Produced in Saliva.** *Eur. J. Inorg. Chem.* 2020, 2020, 38, 3654-3661.
DOI: 10.1002/ejic.202000521

Patrick E. J. Saloga, Tina Rybak, Andreas F. Thünemann. **Phase Transfer of Ultra-small ZnO Nanoparticles to Aqueous Medium.** *Submitted to ChemPhysChem on 28 October 2020.*

Publications not included in this thesis:

Claudia Kästner, Patrick E. J. Saloga, Andreas F. Thünemann. **Kinetic monitoring of gluathione-induced silver nanoparticle disintegration.** *Nanoscale* 2018, 10, 11485-11490.
DOI: 10.1039/c8nr02369g

Christian Goroncy, Patrick E. J. Saloga, Mathias Gruner, Madlen Schmudde, Jonathan Vonnemann, Edwige Otero, Rainer Haag, Christina Graf. **Influence of Organic Ligands on the Surface Oxidation State and Magnetic Properties of Iron Oxide Particles.** *Zeitschrift für Physikalische Chemie* 2018, 232, 5-6, 819-844.
DOI: 10.1515/zpch-2017-1084

Patrick E. J. Saloga, Claudia Kästner, Andreas F. Thünemann. **High-Speed but Not Magic: Microwave-Assisted Synthesis of Ultra-Small Silver Nanoparticles.** *Langmuir* 2018, 34, 147-153.
DOI: 10.1021/acs.langmuir.7b01541

A.2 CONFERENCE CONTRIBUTIONS AND AWARDS

Oral Presentations

Patrick E. J. Saloga, Andreas F. Thünemann, **SAXS in Analysis of Ultrasmall Size-adjustable Zinc Oxide Nanoparticles for Controlled Band Gap Engineering**, *SAS2018 XVII International Small Angle Scattering Conference*, Traverse City, MI, USA, 2018.

Patrick E. J. Saloga, Andreas F. Thünemann, **Messdatenauswertung mittels Origin in der Nanopartikelanalyse**, *ADDITIVE Origin Anwendertage 2018*, Berlin, Germany, 2018, *invited talk*.

Poster Presentations

Patrick E. J. Saloga, Andreas F. Thünemann, **In-situ SAXS/WAXS investigation of zinc oxide nanotube formation**, *SAXS Excites - International SAXS Symposium*, Graz, Austria, 2019.

Patrick E. J. Saloga, Andreas F. Thünemann, **Interaction of digestive biopolymers with zinc chloride as a model for zinc-enriched foods and cosmetics**, *Polydays 2019*, Berlin, Germany, 2019.

Patrick E. J. Saloga, Andreas F. Thünemann, **Size-selective microwave-assisted synthesis of pure zinc oxide nanoparticles for precise band gap engineering**, *6th Nano Today Conference*, Lisbon, Portugal, 2019.

Patrick E. J. Saloga, Andreas F. Thünemann, **What's for eats? – Zinc phosphate nanoparticle mass fractals form during the artificial digestion of zinc chloride**, *6th Nano Today Conference*, Lisbon, Portugal, 2019.

Patrick E. J. Saloga, Claudia Kästner, Andreas F. Thünemann, **Microwave-assisted high-speed silver nanoparticle synthesis**, *NanoWorkshop 2018 (Workshop on Reference Nanomaterials. Current situation and needs: development, measurement, standardization)*, Berlin, Germany, 2018.

Patrick E. J. Saloga, Claudia Kästner, Andreas F. Thünemann, **Do non-thermal effects exist? - Microwave-assisted acceleration of silver nanoparticle synthesis and particle growth**, *5th Nano Today Conference*, Waikoloa Village, HI, USA, 2017.

Awards

Nano Today Student Travel Award, *6th Nano Today Conference*, Lisbon, Portugal, 2019.

Travel Grant of the German Chemical Society, 2017.

A.3 CURRICULUM VITAE

For reasons of data protection, the curriculum vitae is not included in the electronic version of this dissertation.

A.4 DECLARATION OF AUTHORSHIP

I hereby declare that except where specific reference is made to the work of others, the contents of this dissertation are my own unaided work and have not been submitted in whole or in part for consideration for any other degree or qualification in this, or any other university.

Patrick E. J. Saloga